# Non-integer Order Modelling and Signal Based Brain Tissue Classification in Stereoelectroencephalography

Mariana Mulinari Pinheiro Machado

**THÈSE**

pour obtenir le grade de

**DOCTEUR DE L'UNIVERSITÉ GRENOBLE ALPES**

Spécialité : Automatique-Productique

Arrêté ministériel : 25 mai 2016

Présentée par
**Mariana MULINARI PINHEIRO MACHADO**

Thèse dirigée par **Alina VODA**, Université Grenoble Alpes
et co-encadrée par **Gildas BESANÇON**, **Guillaume BECQ**, **Olivier DAVID**

préparée au sein du **Laboratoire Grenoble Images Parole Signal Automatique (GIPSA-Lab)**
dans **l'École Doctorale Electronique, Electrotechnique, Automatique, Traitement du Signal (EEATS)**

# Non-integer Order Modelling and Signal Based Brain Tissue Classification in Stereoelectroencephalography.

Thèse soutenue publiquement le **9 septembre 2022**,
devant le jury composé de:

**Mme. Alina VODA**
Maître de conférences, Université Grenoble Alpes, Directrice de thèse
**M. Olivier DAVID**
Directeur de Recherche, Inserm, Co-encadrent de thèse, Co-directeure de thèse
**M. Laurent KOESSLER**
Chargé de Recherche, CNRS, Rapporteur
**M. Pierre MELCHIOR**
Professeur, Bordeaux INP, Rapporteur
**M. Dan STEFANOIU**
Professeur, Univ. Polytechnique Bucarest, Examinateur
**M. Philippe KAHANE**
Professeur des Universités - Praticien Hospitalier, Université Grenoble Alpes, Examinateur (Président du jury)
**M. Guillaume BECQ**
Ingénieur de Recherche, CNRS, Co-encadrent de thèse (invité)
**M. Gildas BESANÇON**
Professeur des Universités, Grenoble INP, (invité)

# Acknowledgements

In the great scheme of things, three years might not seem like a significant amount of time. However, looking back to where I was in the begging of this thesis, I can not help but feel as if these years will have an everlasting effect on who I am as a professional and most of all as a person.

Being my first experience out of university, I had (and still have) a lot to learn, and what a great experience it was to grow and navigate these uncharted waters with such a supportive group of people, without whom I would most definitely not be where I am today. This section is dedicated to them.

First and foremost, I would like to thank the members of the jury for taking the time to asses my thesis, and for sharing your expertise with me.

Secondly, I would like to thank my supervisors Alina Voda, Gildas Besançon, Guillaume Becq, and Olivier David. I really enjoyed our enlightening and stimulating discussions during these three years, and the amount of knowledge they have passed on to me is immeasurable.

In addition, I would like to thank my family. My parents, my siblings, and my fiance Patrick, for giving me stability and comfort during the most trying times, but also celebrating with me achievements and peaceful times.

Finally, I consider myself very lucky to have crossed paths with so many great people during my time at Gipsa-lab, whom I am very happy to call my friends. Being away from my home country, I found in you the warmth of a family, thank you for receiving me so openly, and for all the knowledge you shared with me, both scientific and personal.

# Contents

# List of Figures

# List of Tables

# Introduction

Neurological disorders are diseases that affect the brain, nerves, spinal cord, neuromuscular junction, and muscles. They can be caused by structural, biochemical or electrical abnormalities, that can either be genetic, congenital or caused by infections. One of the most common disorders of the nervous system is epilepsy, which makes people more susceptible to having recurrent seizures.

Epilepsy can cause complications such as drowning, falling, and car accidents and should therefore be treated. In most of the cases, epilepsy can be managed by medication. However, a population of 30% of epileptic patients suffer from drug-resistant focal epilepsy. For these specific cases a resective surgery might be considered as an option. The success of such a surgery is highly dependent on the correct identification of the epileptic zone (EZ) known to be the focus source of the seizures, and the correct identification of the eloquent cortex to be avoided during surgery.

One of the possible pre-surgical examinations conducted is the stereoelectroencephalography (SEEG), in which electrodes are placed directly into the brain. It is from the signals measured by these electrodes that the EZ can be identified. Given the fact that grey and white matter react differently to stimulation, and that white matter can not be epileptogenic, the correct classification of the brain tissue in which measuring contacts are inserted in could speed up the localisation of the EZ to be removed in surgery.

## Thesis objective

Most of the brain tissue classification done currently is based on imaging. This is why the main focus of this thesis is to propose classification techniques based solely on signals measured in typical SEEG settings. In order to do so, two main approaches are proposed: A signal based one, and a model based one.

The signal based approach consists in the extraction of features either directly from the temporal signals, or their frequency representation, and specially from the non-parametric frequency response of pairs of consecutive measuring contacts. Such features are then used for supervised classification with imaging classification as the ground truth.

The model based approach consists in the physical modelling of the brain-electrode interface. The idea here is to extract features directly from the identified model, that can be used for supervised classification. Such model has been studied in literature for applications in deep brain stimulation. An interesting characteristic of the proposed brain-electrode interface is that it contains a constant phase element (CPE), which introduces a fractional order to the system. The use of non-integer derivatives in engineering is becoming more and more frequent as of recently, due to the fact that they can describe systems with "infinite memory".

Thus, this approach combines the use of dynamical modelling techniques, and some underlying electrical interpretation and parameter identification, with the specificity of dealing with fractional order dynamics.

## Manuscript outline

This manuscript consists of five main chapters. The first two are dedicated to the review of literature on the theoretical concepts, and important methods:

In chapter 1, the general context of this thesis is presented, with a focus on the examinations used for the identification of the EZ, the existing methods for brain tissue classification, and the state of the art for brain-electrode modelling based on its physical properties.

The focus of chapter 2 is to introduce the basic concepts of system identification. The typical modelling structures are reviewed, as well as the non-parametric and parametric identification methods, and how to validate them. It is also in this chapter that the theoretical concept of non-integer derivatives is presented.

The last three chapters are dedicated to the contribution of this study in brain tissue classification using signals measured during SEEG investigations:

In chapter 3 the signal approach for tissue classification is presented and applied to SEEG signals of 19 epileptic patients. The main focus of the chapter is the extraction of features from the non-parametric frequency response of pairs of contacts. Other features extracted directly from the raw SEEG signals are also presented and compared with each other. The results presented in this chapter were published in (M. Machado, Voda, Besançon, Becq, and David 2021),(M. Machado, Voda, Besançon, Becq, Kahane, et al. 2022), and (Lopes et al. 2021).

Chapter 4 is dedicated to the model based approach for brain tissue classification. At first, the modelling of a *phantom EEG* measurement chain is presented with a focus on the physical properties of the system. This first study is used as a starting point for the modelling of the brain-electrode interface using SEEG signals, and was published in (M. Machado, Voda, Besançon, Becq, and David 2020), (M. M. P. Machado et al. 2023), and (Pinheiro Machado et al. 2022a). The proposed model and identification methodology of the brain-electrode interface are presented, as well as how the identified models can be used for brain tissue classification.

Finally, in chapter 5, both signal and model approaches are combined to create a general classification method of trios of consecutive contacts that is able to classify both homogeneous and heterogeneous tissue combinations. The results are compared to previous imaging classification, and possible applications and limitations of the method are discussed. The results were published in (Pinheiro Machado et al. 2022b).

## List of publications

The list of publications of this thesis is the following:

1. **Mariana M. P. Machado**, Alina Voda, Gildas Besançon, Guillaume Becq, Olivier David, “New modeling results for an EEG measurement system with exciting and reading electrodes”. In: IFAC-PapersOnLine 53.2 (2020), pp. 15922–15927 (cit. on pp. 2, 58).

2. **Mariana M. P. Machado**, Alina Voda, Gildas Besançon, Guillaume Becq, Olivier David, “Frequency-domain identification of stereoelectroencephalographic transfer functions for brain tissue classification”. In: IFAC-PapersOnLine 54.7 (2021), pp. 565–570 (cit. on pp. 2, 34).

3. Pedro Lopes, **Mariana M. P. Machado**, Alina Voda, Gildas Besançon, Philippe Kahane, Olivier David, "Machine Learning and Stereoelectroencephalographic Feature Extraction for Brain Tissue Classification." IFAC-PapersOnLine 54.15 (2021): 340-345.

4. **Mariana M. P. Machado**, Alina Voda, Gildas Besançon, Guillaume Becq, Philippe Kahane, Olivier David, “Brain tissue classification from stereoelectroencephalographic recordings”. In: Journal of Neuroscience Methods 365 (2022), p. 109375 (cit. on pp. 2, 34).

5. **Mariana M. P. Machado**, Alina Voda, Gildas Besançon, Guillaume Becq, Olivier David, Philippe Kahane, “Electrode-Brain Interface Fractional Order Modelling for Brain Tissue Classification in SEEG”. In: Biomedical Signal Processing and Control, v. 79, p. 104050, 2023.

6. **Mariana M. P. Machado**, Alina Voda, Gildas Besançon, Guillaume Becq, Olivier David, Philippe Kahane, "Dynamic Modelling of the Brain-electrode Interface for Stereoelectroencephalography," 2022 26th International Conference on System Theory, Control and Computing (ICSTCC), 2022, pp. 576-581.

7. **Mariana M. P. Machado**, Alina Voda, Gildas Besançon, Guillaume Becq, Olivier David, Philippe Kahane, "System-Identification-Based Automatic Brain Tissue Classification for Stereoelectroencephalography," 2022 26th International Conference on System Theory, Control and Computing (ICSTCC), 2022, pp. 440-445.

Chapter 1

# State of the art: Brain tissue classification for epileptogenic zone identification

Epilepsy is a chronic neurological disorder characterised by frequent seizures that interrupt normal brain function. Seizures are caused by abnormal excessive or synchronous neuronal activity in the brain (Fisher et al. 2005). This abnormal activity is likely triggered by a cortical imbalance between excitation and inhibition processes in the brain (David, Bastin, et al. 2010) and (Carvallo et al. 2018). Over 15 million people are diagnosed with epilepsy worldwide (Greene et al. 2021), 30% of which suffer from a type of focal drug-resistant epilepsy (Carvallo et al. 2018).

In the cases when the persistence of drug-resistant seizures interferes with daily activities, and in the case of children, with learning and development, resective surgery of epileptogenic regions becomes an option (Brodie et al. 1997). Focal epilepsy is when seizures originate from abnormal activity in a specific brain area. In this type of epilepsy cases (60% of patients (Acharya et al. 2019)), the surgery consists in the removal or disconnection of the epileptogenic zone (EZ), which is the source of seizures (Greene et al. 2021). The success of the resective surgery depends largely on the correct identification of the EZ. This can be done either with invasive or non-invasive methods.

In the cases where the EZ is located via invasive methods, correct tissue classification becomes an initial discriminatory task necessary to focus on regions of interest. This is because contacts in white matter are usually disregarded by doctors as they can not be epileptogenic. Therefore, if a grey matter contact is wrongly classified and ignored, a part of the EZ may be missed (Greene et al. 2021). Moreover, in functional connectivity analysis, where brain tissues are stimulated, correct classification is important to better interpret the obtained responses (Trebaul, Deman, et al. 2018).

The majority of tissue classification done is based on Magnetic resonance imaging (MRI) and Computer tomography (CT). Only recently the interest in classification using recorded brain signals (Greene et al. 2021) is being proposed. In this context, the study of the brain electrode interface can play an important role, as it can be used to highlight some differences between tissues as shown in (Carvallo et al. 2018).

In the following sections, methodologies for EZ identification are presented, followed by

the state of the art in brain tissue classification. Next, models of the brain-electrode interface based on its physical properties are presented.

## 1.1 Epileptogenic zone identification

There are many methodologies that can be used for the definition of EZ, either invasive or non-invasive. Among the most used non-invasive methods are the Magnetic Resonance Imaging (MRI), Electroencephalography (EEG), and also nuclear medicine such as positron emission tomography (PET) scan, and single-photon emission computed tomography (SPECT) scan. When the EZ can not be detected with non-invasive methods, stereoelectroencephalography (SEEG) is usually used.

Here the focus will be mainly given to MRI, EEG, and SEEG examinations as they are directly related to the study presented in this thesis, their representations can be found in Fig. 1.1. However, for the correct identification of the EZ, PET and SPECT scans are needed for multimodal exploration, as well as video-HD recordings, and human and clinical expertise.

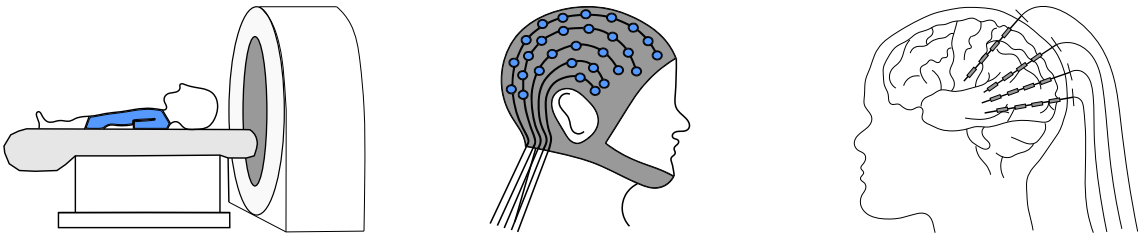

(a) MRI (b) EEG (c) SEEG

Figure 1.1: Representation of common methods for EZ identification.

### 1.1.1 Magnetic resonance imaging (MRI)

Magnetic Resonance Imaging (MRI) is a medical imaging evaluation that employs radio-frequency non-ionising radiation in the presence of controlled magnetic fields to create images of the organs of the body in any plain (Katti et al. 2011).

In epilepsy, MRI is used to identify structural abnormalities that could be the cause of seizures. This type of examination is most commonly used to identify hippocampal sclerosis, malformations of cortical development, vascular malformations, tumours and acquired cortical damage (Duncan 1997). If abnormalities are detected with MRI, the patient is classified as MRI positive, if not the patient is classified as MRI negative. However, 18% to 43% of patients candidate to surgery are MRI negative (Bien et al. 2009). In this case, either the sensitivity of the MRI should be improved or patients need to be addressed to invasive EZ detection techniques.

However, MRI alone is not sufficient for EZ identification as epilepsy is defined by seizures

which can be recorded only by EEG.

### 1.1.2 Electroencephalography (EEG)

Electroencephalography (EEG) consists in the recording of brain electrical potentials using electrodes placed on the scalp of the patient (Nunez et al. 2006). The measured signals are created from neuronal activity. This method is largely used in epilepsy diagnosis due to the fact that it is non-invasive, low cost, and gives a more generalised view of epileptic episodes as electrodes cover different areas.

The diagnosis is done via the recognition of some epileptiform patterns in recorded signals such as spikes, and sharp waves (Noachtar et al. 2009). For patients with focal epilepsy, the EZ is determined with the precise location of the epileptiform discharges. In this case, EEG information is often compared with MRI. The accuracy of the method depends on the localisation of the EZ. Good results are obtained when the EZ is superficial, as it is closer to the measuring electrodes. However, for other cases, EEG might not be sufficient as it is largely impacted by the mixing of signal sources, week signal to noise ratio due to skull conductivity, and small spatial resolution.

### 1.1.3 Stereoelectroencephalography (SEEG)

In cases where non-invasive methods are not enough to locate the EZ, or in cases where the EZ is too close to eloquent cortex, invasive methods are used (Noachtar et al. 2009). The eloquent cortex are the functional areas of the brain that should be speared during surgery, as damage to these parts induce neurological deficits. One of the most common invasive methods in epileptic patients is stereoelectroencephalography (SEEG).

This method of electrode implementation was first proposed by (Talairach et al. 1973). In it, multiple stereotactic electrodes (typically 8 to 15 (Bartolomei, Lagarde, et al. 2017)) are implanted directly in different brain areas. Each electrode is composed by several contacts measuring signals in different locations. An example of electrode implantation and its measured signals is illustrated in Fig. 1.2. The chosen areas for electrode implantation are based on hypothetical EZ location based on previous non-invasive examinations (such as MRI, and EEG).

Measured voltages are usually referenced considering a point in distant white matter. However, signals can be re-referenced to other montages. For instance, in bipolar montage the signal from pairs of adjacent electrode contacts are subtracted. In the case of global average reference, the signals from all contacts are averaged, and the resulting signal is subtracted from all contacts. The choice of the reference montage has a great impact on the analysis of SEEG signals (Mercier et al. 2017), and therefore should be made with caution. Two examples of reference montages are illustrated in Fig. 1.3.

The greatest advantages in using this type of methods is the better signal-to-noise ratio

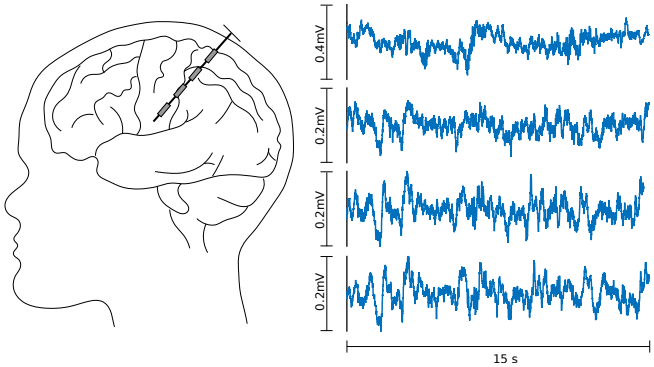


Figure 1.2: Example of the implantation of a SEEG electrode and its typical measured signals.

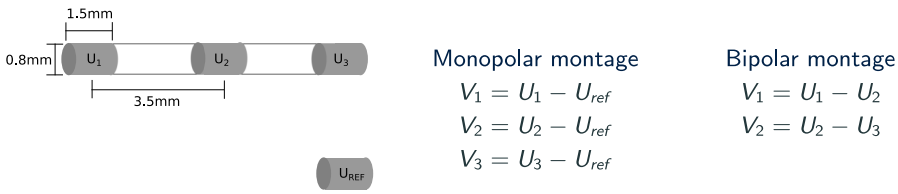


Figure 1.3: Example of monopolar and bipolar reference montages.

compared to scalp EEG, and better signal localisation. They also allow for the measurement of activity in sub-cortical regions.

The use of SEEG in epilepsy is either for direct mapping of the level of activation of individual neurons or brain areas, or for connectivity analysis where the interest is to study the functional interactions of different parts of the brain (Kahane et al. 2014) and (Bartolomei, Lagarde, et al. 2017).

In the first case, the idea is to detect the seizure-onset zone via analysis of SEEG recorded signals. This is usually done with the measurement of the epileptogenicity index (EI) (Bartolomei, Chauvel, et al. 2008). The EI is a quantification of how epileptogenic is a brain region based on the capability of a certain brain region to generate high-frequency oscillations, and the delay of involvement of the region with respect to the onset of the seizure. Based on the idea of the EI, epileptogenicity maps (EMs) were also proposed (David, Blauwblomme, et al. 2011) in which statistical parametric mapping is proposed by the comparison of mean activity of the baseline and mean activity after seizure onset.

The use of SEEG in functional connectivity analysis is mostly to identify the eloquent cortex, in other words, regions that should not be resected in surgery (David, Bastin, et al. 2010). In this types of examinations direct electrical stimulation (DES) of the brain is used to understand the connectivity of brain regions. Two adjacent contacts are stimulated by a bipolar current and the other contacts are used for voltage measurement. The connectivity can be implied via the study of the amplitudes of cortico-cortical evoked potentials (CCEPs) (David, Bastin, et al. 2010) and (David, Job, et al. 2013). DES can also be used for EZ

identification by comparing the response of electrical stimulation of different tissues (David, Woźniak, et al. 2008).

For both the EZ localisation problem and functional connectivity analysis, the correct tissue classification on which the contacts are inserted in is needed. In the functional connectivity case, the type of stimulated tissue has an impact on the connectivity probability (being higher if the stimulated contact is located in white matter) (Trebaul, Deman, et al. 2018). Furthermore, the tuning of electrical stimulation parameters is different in white matter than in grey matter. In the EZ localisation case, white matter contacts are mostly ignored as they can not be epileptogenic. If a disregarded contact in white matter is miss-labeled, the EZ might not be fully characterised (Greene et al. 2021). Thus, correct brain classification becomes an important task.

## 1.2 Brain tissue classification

Neurons and glial cells are the main components of the nervous tissues. Neurons are composed of a soma which is the central cell body, dendrites relatively proximal to the soma that sum information from distant neurons, and axon which is the stem that enables connection to distant neurons. The latest is wrapped in a protective coat of myelin which is white. The representation of a neuron can be found in Fig. 1.4.

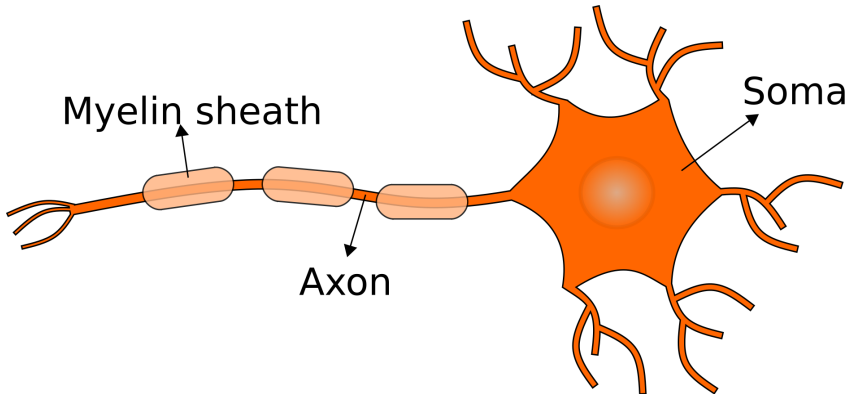


Figure 1.4: Representation of a neuron.

When talking about the brain, and the nervous system in general, two different tissues are often taken into consideration which are the grey and white matter. Grey matter is mainly composed of the neurons somas and is located in the outermost layer of the brain called the cortex. It is responsible for the processing and release of information. White matter is composed by the axons of such neurons and links different parts of the cortex. It is responsible for the propagation of information.

Given the nature of the different brain tissues, epileptic activity originates in grey matter and is spread throughout the brain via white matter. Thus, only grey matter can be epileptogenic.

### 1.2.1 Standard brain tissue classification using imaging

The state of the art of brain tissue classification nowadays is heavily based on structural MRI (Dora et al. 2017). The general idea of tissue classification based on MRI is the comparison between contrasts. The intensity in the image is different for each of the two matters. Therefore, different regions can be identified by looking at each voxel (image intensity at the spatial location).

The standard approach for labelling brain tissues is the co-registration of MRIs with computed tomography (CT) scans. CT scans as well as the MRIs produce images of internal organs. However, contrary to the MRI, they use X-rays to do so. Electrodes are manually positioned in the co-registered image. In order to assign labels to the contacts, softwares such as the one proposed in (Deman et al. 2018) are used. The software labels each contact according to its position in anatomic atlases which are overlaid to the image. The most common label of voxels in a sphere of 3 mm radius around the contact centre is assigned to the contact. This co-registration process of the electrodes with MRI might introduce artefacts in the labelling process.

The tissue classification via imaging is limited by the finite spacial resolution of the imaging device, which makes it impossible to guarantee that every voxel represents only one type of tissue. This phenomenon is called partial volume effect (PVE) (Tohka 2014). In addition, because of the fact that anatomic atlases are used, some deviations might occur due to anatomical variability between patients. Corrections on tissue classification can be done by expert neurophysiologists by visual analysis.

The exploration of tissue classification using methods different from MRI would be helpful mainly when considering contacts in positions with PVE. Furthermore, accurate co-registration procedures are time consuming and are not always available, therefore having a classification method that relies only on SEEG data could be useful.

### 1.2.2 Brain tissue classification using SEEG signals

Differences in SEEG signals depending on contact localisation were already pointed out in literature (Mercier et al. 2017), where the authors compared the power spectra and absolute amplitude of spontaneous brain activity. Nevertheless, up until this point, only one study has proposed brain tissue identification directly from SEEG signals (Greene et al. 2021). In their article, the authors propose a signal approach for tissue classification using bipolar montage and a Bayesian classifier. They do so by considering two main features, the first one is the average vertical shift in the power spectrum of a contact compared to the average power spectrum over all contacts, and the second one is the distance between a contact and the most peripheral contact of the electrode that was not outside of the brain. The results obtained by the authors are promising with an average area under the receiver operating characteristic (ROC) curve of $0.85 \pm 0.079$ across 29 patients.

However, there is a lot more to be explored with tissue classification using SEEG signals in terms of different features to be considered for classification. Even more so due to the fact that different tissues have different conductivities.

## 1.3 Brain tissue conductivity

The estimation of the conductivity of brain tissues is an important field of study in neuroscience for source localisation. When working with EEG signals either to identify the origin of epileptic seizures, or to map current pathways during electrical stimulation of the brain, it is important to correctly define the head model of a patient. Such a model depends on the geometry of the head, and the conductivity of head tissues. Many studies discuss the influence of incorrect head models in source connectivity problems. In (Cho et al. 2015), the authors show the differences in reconstructed sources when neglecting grey and white matter distinctions. In (Holdefer et al. 2006), the authors indicate the differences in current densities when considering anisotropies in resistivity of white matter.

This is why, the study of brain tissue conductivity is very pertinent and largely discussed in literature. Still, there seems to be a great discrepancy in conductivity values found in different studies depending on methodology used for impedance measurement, and demographics of patients as pointed out in (McCann et al. 2019).

### 1.3.1 Methods

One of the used methods is directly applied current (DAC), which is an invasive method that consists in applying current directly into tissue and measuring the potential difference between a pair of electrodes. In these cases, either the impedance measurement is done in post-mortem samples or excised tissues. However, if intracranial electrodes are implanted on the patient, they can be used for in vivo impedance measurement.

An example of in vivo DAC impedance measurements performed in two epileptic patients implanted with intra-cranial electrodes is given in (Carvallo et al. 2018). The obtained conductivity values were close to 0.3 S/m for grey matter and 0.16 S/m for white matter.

As for non-invasive methods, there are electrical impedance tomography (EIT), magnetic resonance EIT (MREIT), and difusion tensor imaging (DTI) for example. These methods are performed in vivo. For EIT, an electrical current is applied to surface electrodes and measured electrical potentials are used to construct a two-dimensional tomogram containning tissues impedances. In the case of MREIT, not only electrical fields are used to reconstruct the conductivity of tissues with the EIT, but also magnectic fields are measured via a magnetic resonance imaging scanner to enrich the knowledge on tissue conductivity. Finally in the DTI case, the diffusion of water molecules is used to generate contrasts in magnetic resonance images, and conductivity maps are obtained exploiting the correlation of water diffusivity and electrical conductivity (Ammari et al. 2017).

The DTI has also been an important tool in white matter mapping, as it highlights the anisotropy of the diffusion coefficient and also of the conductivity in white matter (Basser et al. 1994). This difference in white matter conductivity was also measured by (Logothetis et al. 2007) with the DAC method performed in vivo in monkey primary visual cortex. In their study, different white matter resistances were found depending on the direction of measurement. Measurements in the mediolateral direction revealed a decrease of impedance at the transition between grey and white matter, and measurements in the anterior-posterior direction revealed an increase of impedance. This difference in conductivity depending on the direction of the measurement is justified by the difference in the direction of fibers in white matter. In (Güllmar et al. 2010) the differences in conductivity of white matter depending on fiber orientation were of 0.439 S/m for transverse orientation, and 0.915 S/m for longitudinal orientation using the direct transformation approach on DTI.

According to (McCann et al. 2019) the conductivity of grey matter can vary from 0.27 S/m to 0.75 S/m, and the conductivity of white matter can vary from 0.2 S/m to 0.4 S/m comparing the EIT and MREIT methods.

### 1.3.2 Demographics

Other than the variation of methods used for the measurement of tissue impedance, the subjects in which the impedance is measured also differ. The first difference was already mentioned in the previous section, where measurements are either done in vivo, or post-mortem or in excised tissues. In (Opitz et al. 2017), the authors discuss the biological properties differences in brain tissue that occur after death.

The conductivity of brain tissues has been measured in both animals and humans. Its values are shown to vary depending on which of the animals the measurements have been conducted in. This is discussed in (Geddes et al. 1967), with the conductivity of the cortex varying from 0.45 S/m to 0.48 S/m, and the conductivity of white matter varying from 0.1 S/m to 0.29 S/m, considering an anaesthetised cat and rabbit.

Differences in brain conductivity are also observed considering different diseases. In (McCann et al. 2019), the conductivity of healthy grey matter is compared to the conductivity of grey matter affected by epilepsy, Alzheimer's disease (AD), Parkinson's disease (PD), and stroke. While the conductivity of grey matter affected by AD, PD, and stroke are close to healthy grey matter with values close to 0.52 S/m, the conductivity of grey matter affected by epilepsy has values close 0.27 S/m.

### 1.3.3 Conductivity and brain tissue classification

The exact values of conductivities of grey and white tissues vary depending on the measuring method, and demographics. In addition, in some studies such as (Carvallo et al. 2018) the obtained conductivity values of grey matter are higher than the conductivity of white mat-

ter, whereas the opposite is obtained in (Satzer et al. 2015) for impedance measurements of chronically implanted electrodes in patients suffering from Parkinson's disease.

Nonetheless, in all previous studies mentioned in this section, the difference in conductivity of grey and white matter is always perceptible. Thus, if one can get information on tissue conductivity using SEEG signals, it could be a potential feature for tissue classification. In this scenario, the study of the brain-electrode interface can be used, as it is directly impacted by tissue conductivity.

## 1.4 Brain-electrode interface

The topic of the modelling of the brain-electrode interface has been widely discussed in literature due to its great number of applications. Nevertheless, there is still work to be done in perfecting the models, as they are difficult to study on living systems.

In the cases of patients suffering from movement disorders, the chronic implantation of electrodes in the brain can be used for therapy via deep brain stimulation (DBS) and single-unit neuronal recording. Over time the measured signals are degraded due to corrosion, insulation delamination, and tissue encapsulation due to the foreign-body immune response. These factors also affect the voltage distributions in DBS treatment making them less efficient. In order for improvements to be made to solve or at the very least decrease the effects of tissue encapsulation, the study of the brain-electrode interface is done to quantify impedance changes over time. In (Lempka, Miocinovic, et al. 2009), (Lempka, M. Johnson, et al. 2011), (Sankar et al. 2014), (Otto et al. 2006), and (M. Johnson et al. 2005) the model of the interface is identified via electrode impedance spectroscopy (EIS) or impedance tester, using signals recorded in animals chronically implanted with electrodes.

Contrary to DBS, in the cases of epileptic patients that undergo SEEG investigation, the implanted electrodes are only kept for two weeks. Still, the study of the brain-electrode interface can be used for diagnosis of brain tissue epileptogenicity (Koessler et al. 2017) and (Carvallo et al. 2018). These studies are based on the fact that epileptogenic tissues have different conductivities when compared to healthy tissues. In such studies, the difference in conductivity of grey and white matter are also highlighted which is the motivator of the use of the brain-electrode interface for brain tissue classification.

The brain-electrode model can also be used for artefact correction of electrical stimulation in the cases where SEEG is used in functional connectivity analysis for the correct estimation of CCEPs (Trebaul, Rudrauf, et al. 2016).

The interface is often characterised by an electronic circuit. The proposed circuits might differ from each other in some aspects, but in general they are formed by three main blocks: An electrode-electrolyte interface, a peri-electrode layer (tissue encapsulation of the electrode formed by the brain reaction to foreign bodies), and finally the medium resistance. The physical representation of the mentioned blocks is shown in Fig.1.5.

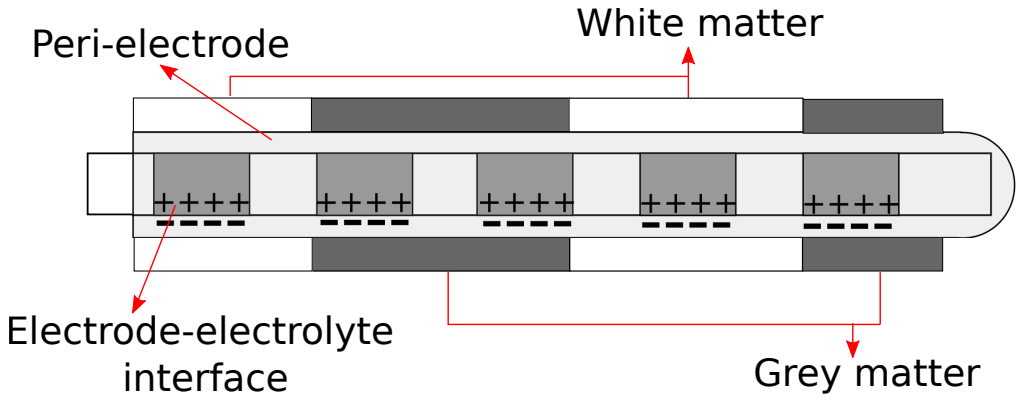


Figure 1.5: Physical representation of the brain-electrode interface.

### 1.4.1 Electrode-electrolyte interface

The study of the electrode-electrolyte interface is of interest in many medical fields, whenever physiological signals are recorded using electrodes, either invasively or not. The choice of the electrode type has a direct impact on the amplitude and dynamics of the measured signals. Thus, the study of the electrode-electrolyte interface allows for the correction of artefacts, which helps with signal interpretation (Besançon et al. 2019), and also helps with the choice of electrode material (Robinson 1968).

One of the first authors to propose an electronic circuit representation of the EEG measurement chain was (Robinson 1968). The author represented the electrode-electrolyte interface as the parallel between a double layer capacitance $C_{dl}$ and a charge transfer, or leakage resistance $R_{ct}$. The double layer capacitance receives such name because it represents the layers of charge, one in the metal surface and the other in the electrolyte of opposite polarity. The charge transfer resistance represents the charges leaked through the double layer from electrochemical reactions. The circuit is show in Fig. 1.6a.

However, it has been shown that the double layer capacitance $C_{dl}$ does not behave as a normal capacitor due to adsoprtion, surface roughness, and molecular forces (De Levie 1965). Instead, it should be represented by a constant phase element (CPE) $Z_{CPE_{dl}}$. This version of the circuit is shown in Fig. 1.6b.

Considering $s$ as the Laplace variable, the impedance $Z_{CPE}$ can be written as:

$$Z_{CPE} = \frac{1}{Qs^{\alpha}} \tag{1.1}$$

with $0 < \alpha < 1$, and $Q$ the constant coefficient of the CPE. The constant phase element receives its name because it has a constant phase angle smaller than 90° of a true capacitance ($\alpha = 1$). The inverse Laplace transform of $s^{\alpha}$ represents a fractional-order time derivative (Liang et al. 2015), which will be discussed in more details in the following chapter. Typically $\alpha \simeq 0.8$ in biomedical systems (McAdams, Lackermeier, et al. 1995) and (Besançon et al.

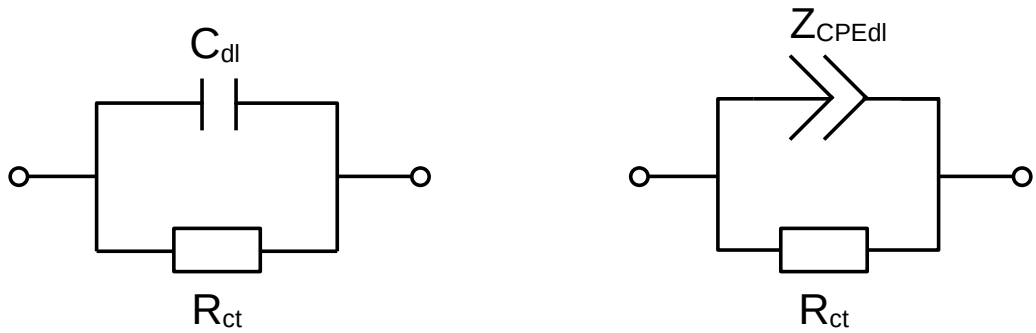


(a) Interface with capacitor (b) Interface with CPE

Figure 1.6: Most common representations of the electrode-electrolyte interface in literature. In (a) the double layer capacitance $C_{dl}$ is used in parallel with the charge transfer resistance $R_{ct}$. In (b) the double layer capacitance is substituted by a CPE $Z_{CPE_{dl}}$ in parallel with the charge transfer resistance $R_{ct}$.

2019).

In general both representations are still used in literature. The representation with the CPE is physically more accurate, but it demands extra computation when compared to the case with a normal capacitance.

Some studies on the electrode-electrolyte interface are done with the use of "phantom EEG" devices (Besançon et al. 2019), in which the impedance is measured by the insertion of electrodes in a saline solution (McAdams, Lackermeier, et al. 1995). The advantage of such studies is that one has control over the electrical stimulation signals used for the identification of the interface, which guarantees very accurate models.

### 1.4.2 Peri-electrode layer

In the case where electrodes are in direct contact with brain tissue, the nervous system reacts by creating an encapsulation layer around the implanted device called the peri-electrode region (Grill et al. 1994). There are two stages after electrode implantation: the acute stage and the chronic stage (Yousif et al. 2009). The acute stage occurs just after electrode implantation. In it, the electrode is surrounded by cerebral spinal fluid and the impedance can be simply characterised by the electrode-electrolyte interface. In the chronic stage, the peri-electrode region is either filled with giant cells or microglia. In the context of chronically implanted electrodes, the time between the acute stage and the stabilisation of the impedance in the chronic stage is of six to eight weeks (Yousif et al. 2009).

Even though the electrodes used in SEEG are not chronically implanted, the recordings are typically done one week after electrode implantation. According to the measurements done by (Lempka, Miocinovic, et al. 2009), the peri-electrode is already present and should be considered as a part of the model.

The standard electronic circuit that represents tissue encapsulation in literature (M. Johnson et al. 2005), (Sankar et al. 2014), and (Lempka, Miocinovic, et al. 2009) is formed by a resistor representing the encapsulation tissue by extracellular matrix proteins ($R_{en}$) in series with the parallel of a resistor and a capacitor representing the physical properties of the cell membrane ($R_{cl}$, and $C_{cl}$). The circuit is show in Fig. 1.7a.

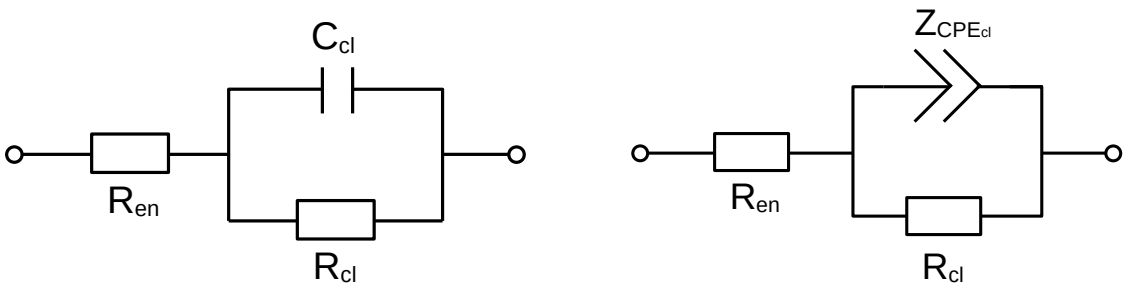


(a) Interface with capacitor (b) Interface with CPE

Figure 1.7: Most common representations of the peri-electrode interface in literature. In (a) the encapsulation resistance $R_{en}$ is in series with the parallel of a resistor $R_{cl}$ and a capacitor $C_{cl}$ representing the physical properties of the cell membrane. In (b) the capacitance $C_{cl}$ is substituted by a CPE $Z_{CPE_{cl}}$.

However, in (Lempka, Miocinovic, et al. 2009), the authors compared the fitted impedance models considering the circuit as described, and substituting the $C_{cl}$ capacitor by a CPE ($Z_{CPE_{cl}}$) to the impedance measured during *in vivo* impedance measurements in a monkey. The circuit with the $Z_{CPE_{cl}}$ had a better fit. The adapted circuit is show in Fig. 1.7b.

### 1.4.3 Medium resistance

The medium resistance $R_{med}$ is represented in both electrode-electrolyte studies (Besançon et al. 2019), and (McAdams, Lackermeier, et al. 1995), and brain-electrode interface studies (M. Johnson et al. 2005), (Sankar et al. 2014), and (Lempka, Miocinovic, et al. 2009). It represents the resistance of the propagation medium present between measuring contacts. In the cases of "phantom EEG", where the electrodes are inserted in saline solutions, this resistance represents the electrolyte resistance. In the cases where electrodes are implanted in the brain, the medium resistance represents the resistance of the brain tissue in between two measurement points.

Thus, in the scope of brain tissue classification via brain-electrode interface modelling, the medium resistance $R_{med}$ becomes a key element to be identified as it is directly related to the tissue type.

### 1.4.4 Complete model and impedance measuring

By adding the three different impedance blocks presented in the previous sections, the final circuit between two measuring contacts is found in Fig. 1.8. The choice was made to keep the CPEs instead of the capacitances as they represent more accurately the physical properties of the brain-electrode interface and tend to produce the best results (Lempka, Miocinovic, et al. 2009).

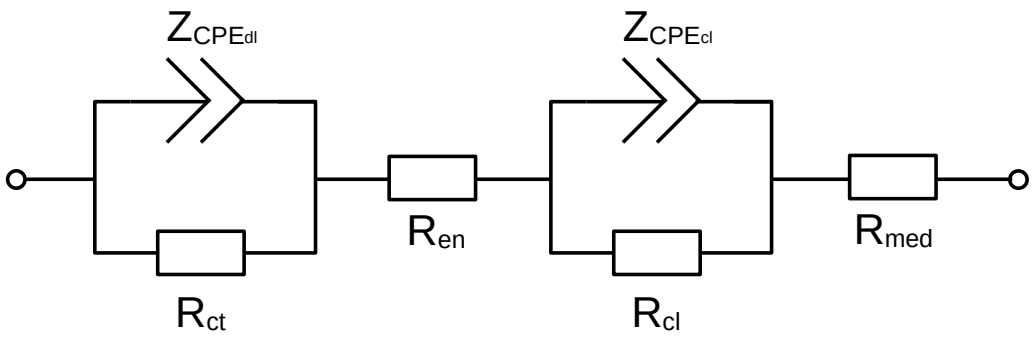


Figure 1.8: Electronic circuit model of the brain-electrode interface, based on physical properties.

In the majority of the cases where the interface model is identified, electrode impedance spectroscopy (EIS) is used (M. Johnson et al. 2005), and (Lempka, Miocinovic, et al. 2009). In this type of measurement, a two contact configuration is utilised. Multiple sine waves of similar amplitude and varying frequencies are applied as electrical stimulation, and the current output is measured. The impedance is calculated in the frequency domain by dividing the voltage by the current considering the frequency of each sine wave. The model is fitted to the impedance measurement by nonlinear regression, with the intent to minimise the difference between the real and imaginary parts of the measured and model impedance, in which the variables to be optimised are the electronic components of the circuit.

However, the current output is not always measured. In some applications, the only information available are voltage measurements. In this case, the impedance can still be measured, but it usually has to be done considering a voltage divider. An example of this can be found in (Besançon et al. 2019) for the electrode-electrolyte interface study on a "phantom EEG".

## 1.5 Conclusion

In this chapter, general concepts in pre-surgical investigation of drug-resistant epileptic patients were presented. The main focus being invasive SEEG examinations and their role in epileptogenic zone identification, and delimitation of the eloquent cortex to be avoided in surgery.

The importance of correct brain tissue classification during SEEG was highlighted for the success of the resective surgery, and the standard methods for tissue labelling were presented. The lack of tissue classification methods based on signal analysis rather than imaging was discussed, and the idea of using brain-electrode interface models to do so was introduced based on the differences of conductivity of brain tissues.

Following that, a recapitulation of the physically based models of the brain-electrode interface was done, in which the concept of constant phase elements with fractional order derivatives was presented. Finally, the standard model identification method of the brain-electrode interface was discussed.

In the following chapter, some general theoretical concepts will be recalled. The focus will predominantly be on fractional order derivatives and system identification methods.

Chapter 2

# State of the art: System identification and non-integer order derivative

The aim of system identification is to build mathematical models from the information contained in data observed from dynamical systems. Usually signals are classified in three types: input $u(t)$, output $y(t)$, and noise $\nu(t)$. Input signals are the ones that are applied to the system in order to get a response (output). The disturbances can either be directly measured or are only observed through their influence on the output.

As introduced in the previous chapter, the hypothesis is made that the identification of the impedance of the brain-electrode interface should be helpful for brain tissue classification. The problem of identifying the electronic components of the model from collected data can be described as a system identification one. In the majority of cases where electronic circuits are used for model characterisation, the relationship between the output and input is linear, thus they can be characterised by impulse or step responses, or by their frequency functions.

In this chapter, the theoretical bases of system identification are presented, as well as some identification methods based on (Ljung 1998), (Landau et al. 2006), and (Stoica et al. 1997). Because of the presence of CPEs in the model, approximations of fractional order derivatives are also discussed.

## 2.1 Time invariant linear systems

In time invariant linear systems, the output $y(t)$ can be written as a linear combination of the output and individual inputs $u(t)$, and is written as follows considering $g(\tau)$ as the impulse response of the system:

$$y(t) = \int_{\tau=0}^{\infty} g(\tau)u(t-\tau)d\tau \tag{2.1}$$

In real life applications, the available signals are measured in the discrete form, considering a sampling time $T_s$. In addition, disturbances also affect the system and need to be considered by adding the term $\nu(t)$ to the output. A time instance is given by $t_k = kT_s$, the output can be described as:

$$y(t) = \sum_{k=1}^{\infty} g(t_k)u(t - t_k) + \nu(t) \tag{2.2}$$

### 2.1.1 Transfer function

Transfer function is the name given to the z-transform of $\{g(t_k)\}_1^{\infty}$:

$$G(z) = \sum_{k=1}^{\infty} g(t_k)z^{-t_k} \tag{2.3}$$

The transition between the time domain and z-domain is straightforward and can be written as:

$$u(t_k - 1) = z^{-1}u(t_k) \tag{2.4}$$

Often times when describing dynamical systems, where differential equations are vastly used, the model is described in a continuous time representation. In this case, the transfer function is re-written using the Laplace transform of the impulse response and the input and output signals:

$$Y(s) = G(s)U(s) \tag{2.5}$$

with $s = i\omega$ the Laplace variable.

In order to go from the continuous to the discrete form of the transfer function, the Laplace variable $s$ can be replaced by a difference approximation. There are many discrete approximations available, in this work, the chosen one is the Tustin approximation:

$$s \approx \frac{2}{T_s}\frac{1 - z^{-1}}{1 + z^{-1}} \tag{2.6}$$

### 2.1.2 Bode and Nyquist plots

Considering the input as $u(t) = cos(\omega t) = \Re e^{i\omega t}$ ($\Re$ denoting the real part), the output is written as:

$$y(t) = \Re\left\{e^{i\omega t}\sum_{k=1}^{\infty} g(t_k)e^{-i\omega t_k}\right\} = |G(e^{i\omega})|cos(\omega t + \varphi) \tag{2.7}$$

with,

$$\varphi = argG(e^{i\omega}) \tag{2.8}$$

The output is a cosine of same frequency as the input, with amplitude controlled by $|G(e^{i\omega})|$ and phase shift $\varphi$. From the relationship between the z-transform and the Fourier transform $z = e^{i\omega}$, each complex number $G(e^{i\omega})$ of the transfer function contains the information of what happens at the output when the input is a sinusoïd of frequency $\omega$. In other words, the transfer function describes the dynamics between the output and the input voltages expected for each signal frequency $\omega$, and can be described via its magnitude $M$ and phase $\varphi$:

$$G(e^{i\omega}) = M(\omega)e^{i\varphi(\omega)} \tag{2.9}$$

The graphical display of $G(e^{i\omega})$ is either the Bode plot or the Nyquist plot. In the Bode plot, $|G(e^{i\omega})|$ is plotted in dB against $\log\omega$, and $\varphi$ is plotted against $\log\omega$. In the Nyquist plot, the imginary part of $G(e^{i\omega})$ is plotted against the real part of $G(e^{i\omega})$.

## 2.2 Non-parametric frequency domain identification

As mentioned, time invariant linear systems, can be characterised by their impulse response and transfer function. In cases of system identification where the model is deduced from measured data, non-parametric methods are used to get an idea of the curve shape of $\{g(t_k)\}_1^\infty$, and $G(e^{i\omega})$ (Bode plots and Nyquist plots) using only the available data. This procedure helps to get an idea of the expected dynamics of the system as well as an idea of the order of the model.

In the context of this study, the focus is given to methods of non parametric identification of the frequency response $G(e^{i\omega})$. For that two main methods are presented: Empirical transfer function estimation (ETFE), and spectral analysis (SPA).

### 2.2.1 Empirical transfer function estimate

The ETFE is an extension of the idea of using multiple sinusoidal inputs of different frequencies and estimating from the output the differences in magnitude and phase for each $\omega$. This can be done for the fact that the different frequencies of the input signal are independent from each other. The equation of the ETFE is given as follows:

$$\hat{G}_{ETFE}(e^{i\omega}) = \frac{Y_N(\omega)}{U_N(\omega)} \tag{2.10}$$

where $Y_N$ and $U_N$ are the Fourier transforms of the output and input respectively using the unitary notations used in (Ljung 1998) and Matlab:

$$U_N(\omega) = \frac{1}{\sqrt{N}} \sum_{t=1}^{N} u(t) e^{-i\omega t} \tag{2.11}$$

$$Y_N(\omega) = \frac{1}{\sqrt{N}} \sum_{t=1}^{N} y(t) e^{-i\omega t} \tag{2.12}$$

with $N$ the length of the signals.

The variance of the frequency response using ETFE for a non periodic input signal is equal to the noise-to-signal ratio at the corresponding signal (Ljung 1998). Therefore, for frequencies in which the measured signals are noisy, the resulting ETFE will also be so. Smoothed versions of the ETFE can be obtained from spectral analysis (SPA) which is presented in the next subsection.

### 2.2.2 Spectral analysis

The principle of obtaining the frequency response from spectral analysis (SPA) is based on the assumption that the values of the true transfer function at different frequencies are related. Thus, the variance can be reduced by averaging over neighbouring frequency points:

$$\hat{G}_{SPA}(e^{j\omega}) = \frac{\int_{-\pi}^{\pi} W_\gamma(\xi - \omega) |U_N(\xi)|^2 \hat{G}_{ETFE}(e^{i\xi}) d\xi}{\int_{-\pi}^{\pi} W_\gamma(\xi - \omega) |U_N(\xi)|^2 d\xi} \tag{2.13}$$

with $W_\gamma$ a window function of width $\gamma$, usually chosen as a Hamming window.

Another way of calculating the SPA, is with the ratio of the windowed periodograms of the input and output signals:

$$\hat{G}_{SPA}(e^{i\omega}) = \frac{\hat{\Phi}_{yu}(\omega)}{\hat{\Phi}_u(\omega)} \tag{2.14}$$

considering $w_\gamma(\tau)$ the inverse Fourier transform of the frequency window $W_\gamma(\omega)$. $\hat{\Phi}_{yu}(\omega)$ is equivalent to:

$$\hat{\Phi}_{yu}(\omega) = \sum_{\tau=-\infty}^{+\infty} w_\gamma(\tau) \hat{R}_{yu}(\tau) e^{-i\omega\tau} \tag{2.15}$$

which is equivalent to the Fourier transform of the cross-correlation function:

$$\hat{R}_{yu}(\tau) = \frac{1}{N}\sum_{t=0}^{N-1} y(t)u(t-\tau) \tag{2.16}$$

and $\hat{\Phi}_u(\omega)$:

$$\hat{\Phi}_u(\omega) = \sum_{\tau=-\infty}^{+\infty} w_\gamma(\tau)\hat{R}_u(\tau)e^{-i\omega\tau} \tag{2.17}$$

which is equivalent to the Fourier transform of the auto-correlation function:

$$\hat{R}_u(\tau) = \frac{1}{N}\sum_{t=0}^{N-1} u(t)u(t-\tau) \tag{2.18}$$

The choice of the width $\gamma$ of the window represents a compromise between making the variance smaller but reducing some system dynamics such as resonance peaks.

As mentioned, $\hat{G}_{SPA}(e^{i\omega})$ is the estimation of $G(e^{i\omega})$, thus it can also be written in the polar form:

$$\hat{G}_{SPA}(e^{i\omega}) = \hat{M}_{SPA}(\omega)e^{i\hat{\varphi}_{SPA}(\omega)} \tag{2.19}$$

## 2.3 Parametric system identification

Even though the non-parametric models are very useful to get insight into the dynamics of the systems, it is of great interest to describe them with mathematical equations that relate the output with the input. In other words identify the coefficients of the transfer function $G(z)$. This is called parametric identification. With a parametric model, one can simulate and predict outputs considering different inputs, design controllers, and they also can be used for diagnosis and fault detection.

Considering $T_s$ as one time unit and using $t$ to enumerate the sampling instants, getting inspiration from equation (2.2) and considering $e(t)$ as a white noise, for linear time-invariant systems, an output can be described as follows:

$$y(t) = G(z)u(t) + H(z)e(t) \tag{2.20}$$

with:

$$G(z) = \sum_{k=1}^{\infty} g(t)z^{-t} \tag{2.21}$$

$$H(z) = 1 + \sum_{k=1}^{\infty} h(t)z^{-t} \tag{2.22}$$

Considering $H(z)$ stable, invertible and monic, and $\theta$ the vector containing the parameters of the transfer function, the one-step-ahead prediction is given by equation:

$$\hat{y}(t|\theta) = H^{-1}(z)G(z)u(t) + [1 - H^{-1}(z)]y(t) \tag{2.23}$$

The main target of parametric identification is to minimise the prediction error $\varepsilon(t)$:

$$\varepsilon(t) = y(t) - \hat{y}(t|\theta) \tag{2.24}$$

In general, the model structure depends on the disturbance term $H(z)e(t)$. In the following subsections, three different model structures are presented together with their system identification methods.

### 2.3.1 Equation error model structure or auto-regressive model (ARX)

In the case of ARX models, the output of the system is written as:

$$y(t) = \frac{B(z)}{A(z)}u(t) + \frac{1}{A(z)}e(t) \tag{2.25}$$

with:

$$A(z) = 1 + A_1 z^{-1} + \cdots + A_{n_a} z^{-n_a} \tag{2.26}$$
$$B(z) = B_1 z^{-1} + \cdots + B_{n_b} z^{-n_b} \tag{2.27}$$

The one-step-ahead prediction is given by:

$$\hat{y}(t|\theta) = B(z)u(t) + [1 - A(z)]y(t) = \theta^T \varphi(t) = \varphi^T(t)\theta \tag{2.28}$$

with:

$$\theta = [A_1, \cdots, A_{n_a}, B_1, \cdots, B_{n_b}]^T \tag{2.29}$$

$$\varphi(t) = [-y(t-1), \cdots, -y(t-n_a), u(t-1), \cdots, u(t-n_b)]^T \tag{2.30}$$

From the linear relationship between the vector of unknowns $\theta$ and the predicted output $\hat{y}(t|\theta)$, the model is a linear regression. The prediction error to be minimised becomes:

$$\varepsilon(t, \theta) = y(t) - \theta^T \varphi(t) \tag{2.31}$$

In order to minimise the error, a convex cost function (cost function with an unique minimum) $V_N(\theta)$ should be proposed. In the case of ARX models, this can be easily done with the following equation:

$$V_N(\theta) = \sum_{t=1}^{N} \varepsilon^2(t, \theta) \tag{2.32}$$

which is known as the least-squares estimate (LSE). The minimum of the cost function can be found via the gradient. The values of $\hat{\theta}$ for which the gradient of $V_N$ is equal to zero, are the optimum coefficients for the transfer function:

$$\hat{\theta} = \arg\min V_N(\theta) = \left[\sum_{i=1}^{t} \varphi(i)\varphi^T(i)\right]^{-1} \sum_{i=1}^{t} \varphi(i)y(i) \tag{2.33}$$

In some applications, it might be useful to perform system identification on-line in order to make decisions about the system. On-line system identification algorithms are called *adaptive* or *recursive*. The general form of such methods is:

$$\hat{\theta}(t) = \hat{\theta}(t-1) + \alpha f(t) \tag{2.34}$$

The search direction $f(t)$ is based on information about the cost function, and $\alpha$ is a constant that represents the compromise between fast conversion of the algorithm and precision of the optimization. The search direction should be the one that minimizes the cost function. As the gradient indicates the direction in which the cost function increases, $f(t)$ should move in the opposite direction of the gradient. In the case of recursive algorithms, the prediction error $\varepsilon$ can be either considered *a priori* $\varepsilon^0(t) = y(t) - \hat{\theta}^T(t-1)\varphi(t)$ or *a posteriori* $\varepsilon(t) = y(t) - \hat{\theta}^T(t)\varphi(t)$.

Considering $F = cI$ the adaptation matrix gain with $c > 0$ and $I$ the identity matrix, and considering $f(t) = -\nabla[\varepsilon^0(t)]^2$, equation (2.55) can be rewritten as:

$$\hat{\theta}(t) = \hat{\theta}(t-1) + F\varphi(t)\varepsilon^0(t) \tag{2.35}$$

This equation can be unstable depending on the values of $c$ in regards to the magnitude of the signals. In order to avoid instability, the *a posteriori* prediction error is considered instead of the *a priori* error used so far:

$$\hat{\theta}(t) = \hat{\theta}(t-1) + F\varphi(t)\varepsilon(t) \tag{2.36}$$

One can write:

$$\varepsilon(t) = y(t) - \hat{\theta}^T(t-1)\varphi(t) - [\hat{\theta}(t) - \hat{\theta}^T(t-1)]\varphi(t) \tag{2.37}$$

from equation (2.36):

$$\hat{\theta}(t) - \hat{\theta}(t-1) = F\varphi(t)\varepsilon(t) \tag{2.38}$$

the *a posteriori* error can be written as a function of the *a priori* error:

$$\varepsilon(t) = \varepsilon^0(t) - \varphi^T(t)F\varphi(t)\varepsilon(t) \tag{2.39}$$

$$\varepsilon(t) = \frac{\varepsilon^0(t)}{1 + \varphi^T(t)F\varphi(t)} \tag{2.40}$$

with that equation (2.38), can be rewritten as:

$$\hat{\theta}(t) = \hat{\theta}(t-1) + \frac{F\varphi(t)\varepsilon^0(t)}{1 + \varphi^T(t)F\varphi(t)} \tag{2.41}$$

It is important to note that the minimization of $[\varepsilon(t)]^2$ at each step is not the same as the minimization of $V_N(\theta)$ in equation (2.32). For that the adaptation gain should vary.

From equation (2.33), if one considers:

$$F(t)^{-1} = \sum_{i=1}^{t} \varphi(i)\varphi^T(i) \tag{2.42}$$

then,

$$\hat{\theta}(t) = F(t)\sum_{i=1}^{t}\varphi(i)y(i) \tag{2.43}$$

$$F(t)^{-1} = \sum_{i=1}^{t}\varphi(i)\varphi^T(i) = F(t-1)^{-1} + \varphi(t)\varphi^T(t) \tag{2.44}$$

Given that:

$$\sum_{i=1}^{t}\varphi(i)y(i) = \sum_{i=1}^{t-1}\varphi(i)y(i) + \varphi(t)y(t) + \varphi(t)\varphi^T(t)\hat{\theta}(t-1) - \varphi(t)\varphi^T(t)\hat{\theta}(t-1) \tag{2.45}$$

one can write:

$$\sum_{i=1}^{t}\varphi(i)y(i) = F(t)^{-1}\hat{\theta}(t) = F(t-1)^{-1}\hat{\theta}(t-1) + \varphi(t)\varphi^T(t)\hat{\theta}(t-1) + \varphi(t)[y(t) - \hat{\theta}^T(t-1)\varphi(t)] \tag{2.46}$$

which results in:

$$F(t)^{-1}\hat{\theta}(t) = F(t)^{-1}\hat{\theta}(t-1) + \varphi(t)\varepsilon^0(t) \tag{2.47}$$

The recursive equation is obtained by multiplying both sides by $F(t)$:

$$\hat{\theta}(t) = \hat{\theta}(t-1) + F(t)\varphi(t)\varepsilon^0(t) \tag{2.48}$$

In this case, the gain matrix $F(t)$ is time varying, and can also be estimated recursively by inverting equation (2.44). Thus, the recursive least squares algorithm is given as:

$$\begin{cases} \hat{\theta}(t) = \hat{\theta}(t-1) + F(t)\varphi(t)\varepsilon^0(t) \\ F(t) = \left[F(t-1) - \frac{F(t-1)\varphi(t)\varphi^T(t)F(t-1)}{1+\varphi^T(t)F(t-1)\varphi(t)}\right] \\ \varepsilon^0(t) = y(t) - \hat{\theta}^T(t-1)\varphi(t) \end{cases} \tag{2.49}$$

If the recursive equation of $F(t)$ in (2.49) is re-written, one can obtain:

$$\hat{\theta}(t) - \hat{\theta}(t-1) = F(t)\varphi(t)\varepsilon^0(t) = F(t-1)\varphi(t)\frac{\varepsilon^0(t)}{1+\varphi^T(t)F(t-1)\varphi(t)} \tag{2.50}$$

From equation (2.40), the RLS algorithm can be re-written using the *a posteriori* error as follows:

$$\begin{cases} \hat{\theta}(t) = \hat{\theta}(t-1) + F(t-1)\varphi(t)\varepsilon(t) \\ F(t) = \left[F(t-1) - \frac{F(t-1)\varphi(t)\varphi^T(t)F(t-1)}{1+\varphi^T(t)F(t-1)\varphi(t)}\right] \\ \varepsilon(t) = \frac{y(t)-\hat{\theta}^T(t-1)\varphi(t)}{1+\varphi^T(t)F(t-1)\varphi(t)} \end{cases} \tag{2.51}$$

The initialization of $F$ can be given as $F(0) = (1/\delta)I$, with $0 < \delta << 1$.

### 2.3.2 Auto-regressive moving average (ARMAX)

In the ARMAX structure, the equation error is equivalent to the moving average of the white noise, in which the output is written as:

$$y(t) = \frac{B(z)}{A(z)}u(t) + \frac{C(z)}{A(z)}e(t) \tag{2.52}$$

the only difference to the ARX case is the $C(z)$ numerator multiplying the disturbance:

$$C(z) = 1 + C_1 z^{-1} + \cdots + C_{n_c} z^{-n_c} \tag{2.53}$$

The one-step-ahead prediction is given by:

$$\hat{y}(t|\theta) = B(z)u(t) + [1 - A(z)]y(t) + [C(z) - 1][y(t) - \hat{y}(t|\theta)] = \theta^T \varphi(t, \theta) \tag{2.54}$$

with:

$$\theta = [A_1, \cdots, A_{n_a}, B_1, \cdots, B_{n_b}, C_1, \cdots, C_{n_c}]^T \tag{2.55}$$

$$\varphi(t, \theta) = [-y(t-1), \cdots, -y(t-n_a), u(t-1), \cdots, u(t-n_b), \varepsilon(t-1, \theta), \cdots, \varepsilon(t-n_c, \theta)]^T \tag{2.56}$$

where:

$$\varepsilon(t, \theta) = y(t) - \hat{y}(t|\theta) \tag{2.57}$$

The aim is still minimising $\varepsilon(t, \theta)$ by choosing the optimum $\hat{\theta}$. However, the relationship between the output of the model $\hat{y}(t|\theta)$ and $\hat{\theta}$ is non-linear, as $\varphi(t, \theta)$ is dependent on $\theta$. Thus,

the cost function of equation (2.32) is not convex, meaning that the optimisation problem contains local minima, and therefore the gradient is equal to zero for several $\hat{\theta}$. Moreover, the gradient of the cost function is non-linear in $\hat{\theta}$, making it hard for it to be estimated. This is why for this case, $\hat{\theta}$ is estimated via iterative methods.

One of the possible iterative methods that can be used to solve the identification problem is the extended least squares (ELS). The algorithm itself is similar to the RLS summarized by equation (2.66), the only difference are vectors $\theta$, and $\varphi$ given by equations (2.55), and (2.56), that depend on the disturbance model.

### 2.3.3 Output error (OE)

For the output error case, the disturbance is considered as a white noise directly added to the output:

$$y(t) = \frac{B(z)}{A(z)}u(t) + e(t) \tag{2.58}$$

The one-step-ahead prediction is given by:

$$\hat{y}(t|\theta) = \frac{B(z)}{A(z)}u(t) = \theta^T \varphi(t, \theta) \tag{2.59}$$

with:

$$\theta = [A_1, \cdots, A_{n_a}, B_1, \cdots, B_{n_b}]^T \tag{2.60}$$

$$\varphi(t, \theta) = [-\hat{y}(t-1|\theta), \cdots, -\hat{y}(t-n_a|\theta), u(t-1), \cdots, u(t-n_b)]^T \tag{2.61}$$

As for the ARMAX case, $\varphi(t, \theta)$ is dependent on $\hat{\theta}$, which makes the cost function $V_N(\theta)$ non-convex. Once again, for this type of problem, $\hat{\theta}$ has to be estimated iteratively. In the case of OE systems, instrumental variable techniques are used.

Instrumental variable (IV) methods are often used in statistics, but can also be used for system identification (Young 1970). It consists of introducing an instrumental variable $\zeta$ on equation (2.33) of the least squares method:

$$\hat{\theta} = \arg\min V_N(\theta) = \left[\sum_{i=1}^{t} \zeta(i)\varphi^T(i)\right]^{-1} \sum_{i=1}^{t} \zeta(i)y(i) \tag{2.62}$$

Here, $\varphi^T(t)$ is the predictor regressor vector, and $\zeta$ is the observation vector:

$$\varphi(t) = [-y(t-1), \cdots, -y(t-n_a), u(t-1), \cdots, u(t-n_b)]^T \tag{2.63}$$
$$\zeta(t) = [-y_{IV}(t-1), \cdots, -y_{IV}(t-n_a), u(t-1), \cdots, u(t-n_b)]^T \tag{2.64}$$

with:

$$y_{IV} = \hat{\theta}(t)\zeta(t) \tag{2.65}$$

As $\zeta$ depends on $y_{IV}$ that depends on $\hat{\theta}$ at each instant, it needs to be estimated recursively. The recursive estimation of the IV method is quite similar to the RLS:

$$\begin{cases} \hat{\theta}(t) = \hat{\theta}(t-1) + F(t-1)\zeta(t)\varepsilon(t) \\ F(t) = [F(t-1) - \frac{F(t-1)\zeta(t)\varphi^T(t)F(t-1)}{1+\varphi^T(t)F(t-1)\zeta(t)}] \\ \varepsilon(t) = \frac{y(t)-\hat{\theta}^T(t-1)\varphi(t)}{1+\varphi^T(t)F(t-1)\zeta(t)} \end{cases} \tag{2.66}$$

## 2.4 Interior-point method

The methods presented in the previous section for system identification are very efficient and largely used for control applications. However, none of them allow constraints to be set on the variable being optimized. As the identification methods will be used to identify transfer function coefficients that are a combination of electronic components, positivity constraints can be useful. The interior point method (Waltz et al. 2006) and (Wächter et al. 2006) is often used in this case.

A constrained optimisation problem can be written as:

$$\begin{aligned} \underset{x\in\mathbf{R}}{\text{minimize}} \quad & f(x) \\ \text{subject to} \quad & ceq(x) = 0 \\ & c(x) \leq 0 \end{aligned} \tag{2.67}$$

in which the variable $x$ needs to be optimised in order to minimise the cost function $f(x)$ subject to some equality constraints ($ceq(x) = 0$), and some inequality constraints ($c(x) \leq 0$).

The first step is to incorporate the equality and inequality constraints into the cost function. In order to do so, the Lagrangian and the barrier function are used respectively.

The Lagrangian rewrites the cost function $f(t)$ into a new one $g(t)$ taking into account the equality constraint $ceq(x) = 0$.

If there are $i$ equality constraints, the cost function will be written as:

$$g(t) = f(x) + \lambda_1 ceq_1(x) + \lambda_2 ceq_2(x) + \cdots + \lambda_i ceq_i(x) \tag{2.68}$$

with $\lambda$ being the Lagrange multipliers which are positive.

For the case of the inequality constraints, first they are transformed into equality constraints with the use of slack variables $c(x) + s = 0$, in which $s$ represents slack variables that are added to vector $x$ to be optimised subject to $s > 0$. There are as many slack variables as there are non equality constraints.

For the simple constraints $s > 0$, a smooth solution would be the logarithmic function, as it tends to infinity as we approach the boundary (0). This is known as the barrier function. With that, rewriting the cost function considering $j$ inequality constraints will result in:

$$g(t) = f(x) + \lambda_{ceq} ceq(x) + \lambda_c(c(x) + s) - \mu \sum_{k=1}^{j} ln(s_k) \tag{2.69}$$

The term $\mu$ is the duality measure, when it is zero the optimal is achieved and the minimisation problem is similar to an unconstrained one. Sometimes the optimum is located outside of the barrier so $\mu$ can be small but never zero. Usually $\mu$ is started off with an initial value and changes with iterations.

Considering the new cost function in equation (2.69), its minimum can be found when its gradient is approximated to zero. Applying the gradient in respect to the variable x, one obtains:

$$\bigtriangledown f(x) + \lambda_{ceq} \bigtriangledown ceq(x) + \lambda_c \bigtriangledown (c(x) + s) - \mu \sum_{k=1}^{j} \frac{1}{s_k} = 0 \tag{2.70}$$

The term $\mu/s_k$ is non linear, so it will be replaced by a term $z$ ( for which $z_k = \mu/s_k$). From this point forward the equality conditions $c(s) + s$ will be included in the $ceq$ conditions. With that the Karush-Kuhn-Tucker (KKT) optimal conditions can be rewritten as:

$$\begin{cases} \bigtriangledown f(x) + \lambda_{ceq} \bigtriangledown ceq(x) + \lambda_c \bigtriangledown (c(x) + s) - z = 0 \\ ceq(x) = 0 \\ \\ XZe - \mu e = 0 \end{cases} \tag{2.71}$$

with $X$ and $Z$ diagonal matrices with the values of $x$ and $z$ respectively, and $e$ a vector of ones added to the equation to make the dimensions right. In these new optimal conditions, the third equation describes the duality gap that for a non constrained problem should be equal to zero.

In order to solve the system of equations (2.71) the Newton-Raphson method can be used. It consists in an iterative method that transforms the non linear equation (the cost function) into a second order equation approximated by the Taylor transformation as follows:

$$g(x_k + \Delta x_k) \sim g(x_k) + \bigtriangledown g(x_k)^T \Delta x_k + \frac{1}{2} \Delta x_k{}^T \bigtriangledown^2 g(x_k) \Delta x_k \tag{2.72}$$

in which the operator $\bigtriangledown^2 g(x_k)$ is called the Hessian.

With that in mind, the first thing to do would be to determine the step size between one iteration and the next one for each of the changing variables ($x$, $\lambda$ and $z$ because of the changes in $\mu$ and $x$). From the KKT conditions and the second order approximation of the cost function, the following system of equations can be written in order to find the needed step sizes ($d_k^x$, $d_k^\lambda$ and $d_k^z$):

$$\begin{bmatrix} W_k & \bigtriangledown ceq(x_k) & -I \\ \bigtriangledown ceq(x_k)^T & 0 & 0 \\ Z_k & 0 & x_k \end{bmatrix} \begin{pmatrix} d_k^x \\ d_k^\lambda \\ d_k^z \end{pmatrix} = - \begin{pmatrix} \bigtriangledown f(x_k) + \bigtriangledown ceq(x_k)\lambda_k - z_k \\ ceq(x_k) \\ X_k Z_k e - \mu_j e \end{pmatrix} \tag{2.73}$$

with:

$$W_k = \bigtriangledown_{xx}^2 (f(x) + ceq(x_k)^T \lambda_k - z_k) \tag{2.74}$$

$$X_k = \begin{bmatrix} x_1 & 0 & \cdots & 0 \\ 0 & x_2 & \cdots & 0 \\ \cdots & \cdots & \cdots & \cdots \\ 0 & \cdots & 0 & x_n \end{bmatrix} \tag{2.75}$$

$$Z_k = \begin{bmatrix} z_1 & 0 & \cdots & 0 \\ 0 & z_2 & \cdots & 0 \\ \cdots & \cdots & \cdots & \cdots \\ 0 & \cdots & 0 & z_n \end{bmatrix} \tag{2.76}$$

To solve equation (2.73), it needs to be rearranged into a symmetric linear system of the following form:

$$\begin{bmatrix} W_k + \Sigma_k & \bigtriangledown ceq(x_k) \\ \bigtriangledown ceq(x_k)^T & 0 \end{bmatrix} \begin{pmatrix} d_k^x \\ d_k^\lambda \end{pmatrix} = - \begin{pmatrix} \bigtriangledown f(x_k) + \bigtriangledown ceq(x_k)\lambda_k \\ ceq(x_k) \end{pmatrix} \tag{2.77}$$

with:

$$\Sigma_k = X_k^{-1} Z_k \tag{2.78}$$

and with that the last step size is given by:

$$d_k^z = \mu_k X_k^{-1} e - z_k - \Sigma_k d_k^x \tag{2.79}$$

With that, each of the next iterations are given by the following equations:

$$x_{k+1} = x_k + \alpha_k d_k^x \tag{2.80}$$

$$\lambda_{k+1} = \lambda_k + \alpha_k d_k^\lambda \tag{2.81}$$

$$z_{k+1} = z_k + \alpha_k d_k^z \tag{2.82}$$

The value of $\alpha$ can be either chosen with a decrease of a merit function or with filter methods. The iterations stop when a convergence criteria is reached. Based on the KKT conditions, the iterations can be stopped when the three equations in (2.71) are less or equal to a tolerance threshold $\epsilon_{tol}$:

$$\begin{cases} max| \bigtriangledown f(x) + \lambda \bigtriangledown c(x) - z| \leq \epsilon_{tol} \\ max|c(x)| \leq \epsilon_{tol} \\ max|XZe - \mu e| \leq \epsilon_{tol} \end{cases} \tag{2.83}$$

With all these equations, the iterative algorithm to solve the optimization problem goes as follows: First, initial values are set for the variables $x$, $\lambda$ and $z$, convergence is checked for these values with the system of equations (2.83) , if it does not converge equations (2.77) to (2.82) need to be solved in order to find the new values for the variables $x$, $\lambda$ and $z$. This is repeated until equations in (2.83) are satisfied.

In the cases for which the interior point method is used with non linear cost functions such as the ones for ARMAX and OE systems, there is a chance that the solution might be a local minimum. Therefore the choice of the initial point is very important to assure good results.

## 2.5 Model validation

In many real life applications little is known about the real structure of the system. Thus, a model needs to be validated through some tests. The first analysis to be done is that of the

fit of the model output compared to the real output. Quantitatively this is represented by the normalised root mean squared error in percentage:

$$fit = 100\left(1 - \frac{||y(t) - \hat{y}(t|\theta)||}{||y(t) - \overline{y}(t)||}\right) \tag{2.84}$$

with $\overline{y}(t)$ the mean of $y(t)$.

The next thing that can be done, is the visual analysis of the fit in the frequency domain. That is done by comparing Bode and Nyquist plots obtained from the identified model to the Bode and Nyquist plots obtained from the data via the ETFE or the SPA. Considering that data is affected by noise, it is hard to compute this fit quantitatively, therefore it is usually done visually.

Apart from the fit analysis, other tests can be done based on the prediction error $\varepsilon$. For structures of the type ARX and ARMAX, $\varepsilon$ is a white noise. The validation in this case should test the whiteness of the noise. In order to do so, one has to compute the normalised auto-correlation $RN_\varepsilon(i)$ of $\varepsilon$ for $i = 0, 1, \cdots, i_{max}$, with $i_{max}$ the maximum number of lags:

$$RN_\varepsilon(i) = \frac{\frac{1}{N+1}\sum_{t=1}^{N+1}\varepsilon(t)\varepsilon(t-i)}{\frac{1}{N+1}\sum_{t=1}^{N+1}\varepsilon^2(t)} \tag{2.85}$$

if $\varepsilon$ is a white noise, than $RN_\varepsilon(i) \sim 0 \,\forall\, i \neq 0$.

The second test to be performed is the cross-correlation test between output estimation error $\varepsilon$ and the input $V_1$, in order to check their independence. The normalised cross-correlation of signals $RN_{\varepsilon,u}(i)$ considering a lag $i = 0, 1, 2...i_{max}$ is given by:

$$RN_{\varepsilon,u}(i) = \frac{\frac{1}{N+1}\sum_{t=1}^{N+1}\varepsilon(t)u(t-1)}{\left[\left(\frac{1}{N+1}\sum_{t=1}^{N+1}u^2(t)\right)\left(\frac{1}{N+1}\sum_{t=1}^{N+1}\varepsilon_2^2(t)\right)\right]} \tag{2.86}$$

the signals can be considered as independent if $RN_{\varepsilon,u}(i) \sim 0 \,\forall\, i$.

For the OE case, the resulting prediction error is a coloured noise, therefore it can not be validated by the whiteness test. However, for an OE model to be validated the prediction error has to be uncorrelated with the input, and the cross-correlation test must be used.

The general rule for validation given in (Landau et al. 2006) for a 97% confidance level is:

$$RN_\varepsilon(i) < \frac{2.17}{\sqrt{N}} \;\; \forall\, i \neq 0 \tag{2.87}$$

$$RN_{\varepsilon,u}(i) < \frac{2.17}{\sqrt{N}} \;\; \forall\, i \tag{2.88}$$

## 2.6 Non-integer order derivatives

The use of non-integer derivatives in engineering is becoming more and more frequent as of recently. Even with the lack of physical or geometrical meaning, fractional calculus has a very interesting memory property. They are not local as the non-integer derivative of a function in a given time takes into account the whole past of the function. Thus, such systems have attracted some attention in the control community (see (Oustaloup 1995a) and (Podlubny 1998)) with a focus on non-integer order identification (see (Malti et al. 2006) and (Trigeassou et al. 1999)). The applications of non-integer order identification are very large on the biomedical field. In (Magin et al. 2008), it is used for modelling of the cardiac tissue electrode interface, and in (Sommacal et al. 2008) it is used to model the gastrocnemius muscle of the frog. In addition, they have also sparked some interest in different fields such as modelling of lithium-ion batteries (see (Zou et al. 2017)), and even for the design of controllers (see (Bohannan 2008)).

The first references of half-order derivatives are associated with Leibniz and L'Hôpital in 1695. To define a non-integer order derivative one has to first define the non-integer order integral. Considering a continuous function $f(t)$, its integral of order $\alpha$ known as the Riemann-Liouville integral is:

$$I_c^{\alpha} f(t) \triangleq \frac{1}{\Gamma(\alpha)} \int_0^t \frac{f(\tau)}{(t-\tau)^{1-\alpha}} d\tau \tag{2.89}$$

with $\Gamma$ the the Euler Gamma function given by:

$$\Gamma(\xi) = \int_0^{\infty} x^{\xi-1} e^{-x} dx \tag{2.90}$$

The notion of non-integer order integral is used as a basis for the definition of the non-integer order derivative (see (Samko et al. 1993)), which can be defined as an integer derivative of order $m = \lfloor \alpha \rfloor + 1$ (with $\lfloor . \rfloor$ the floor operator) of a non-integer integral of order $1-(m-\alpha)$:

$$D^{\alpha} f(t) = D^m (I^{m-\alpha} f(t)) \triangleq \frac{1}{\Gamma(m-\alpha)} \left(\frac{d}{dt}\right)^m \int_0^t \frac{f(\tau)}{(t-\tau)^{1-(m-\alpha)}} d\tau \tag{2.91}$$

The Laplace transform of a non-integer order derivative is given as (see (Oldham et al. 1974)):

$$\mathscr{L}\{D^{\alpha} f(t)\} = s^{\alpha} F(s) \tag{2.92}$$

With this definition, a transfer function of the form:

$$H(s) = \frac{Y(s)}{U(s)} = \frac{\sum_{i=0}^{n_b} b_i s^{\beta_i}}{1 + \sum_{j=1}^{n_a} a_j s^{\alpha_j}} \tag{2.93}$$

can be written in time as:

$$y(t) + a_1 D^{\alpha_1} y(t) + \cdots + a_{n_a} D^{\alpha_{n_a}} y(t) = b_0 D^{\beta_0} u(t) + b_1 D^{\beta_1} u(t) + \cdots + b_{n_b} D^{\beta_{n_b}} u(t) \tag{2.94}$$

Considering the representation in equation (2.94), there is a great interest in studying the finite difference approximations for fractional differential equations.

The Grünwald-Letnikov equation for a discrete approximation of the non-integer derivative was proposed by (Grunwald 1867) and (Letnikov 1868), based on the integer order derivative definition, and it can be written in the following form for a discrete time $k$:

$$D_{GL}^{\alpha} f(k) \simeq \frac{1}{h^{\alpha}} \sum_{i=0}^{N} (-1)^i \binom{\alpha}{i} f(k-i) \tag{2.95}$$

in which $h$ denotes the sampling time, $N+1$ the number of samples, and $\binom{\alpha}{i}$ represents the generalized Newton binomial:

$$\binom{\alpha}{i} = \frac{\Gamma(\alpha+1)}{\Gamma(i+1)\Gamma(\alpha-i+1)} \tag{2.96}$$

This discretisation method is one of the most popular ones when it comes to system identification (see (Malti et al. 2006)). One can find the *Matlab* code for this approximation in (Jonathan 2022).

In the cases of system identification for which recursive algorithms are used (ARMAX and OE models), the discretisation of the non-integer order derivative via the Grünwald-Letnikov method can be very time consuming due to its "infinite memory". In such cases, it might be a better option to approximate the non-integer order derivative to a simple IIR filter. Many authors have proposed methods for the rational approximations of fractional derivatives (see (Carlson et al. 1964), (Matsuda et al. 1993), and (Oustaloup 1995b)). Here the chosen one was proposed by (Petrás 2011), as it was already implemented in *Matlab* (see (Petráš 2003)).

In (Petrás 2011), the author proposes a continued fraction expansion (CFE) of the Al-Alaoui discretization of the fractional derivative described in (Al-Alaoui 1993).

In this procedure a generating function $\omega$ is chosen as the digital approximation of $s^{\alpha}$ ($s^{\alpha} \approx \omega(z^{-1})$), based for example in the Tustin approximation of the Laplace variable $s$. In (Petrás 2011) the generating function is chosen as in equation (2.97) below, in which $a$ is a ratio term chosen as $a = 1/7$ as the Al-Alaoui rule for the discretization of $D^{\alpha}$.

$$(\omega(z^{-1}))^{\pm\alpha} = \left(\frac{1+a}{h}\frac{1-z^{-1}}{1+az^{-1}}\right)^{\pm\alpha} \tag{2.97}$$

Applying the continued fraction expansion (CFE) in the generating function (2.97) one obtains equation (2.98) which ultimately results in equation (2.99) by truncation:

$$(\omega(z^{-1}))^{\pm\alpha} \approx \left(\frac{1+a}{h}\right)^{\pm\alpha} CFE\left\{\left(\frac{1-z^{-1}}{1+az^{-1}}\right)^{\pm\alpha}\right\}_{m,n} \tag{2.98}$$

$$(\omega(z^{-1}))^{\pm\alpha} \approx \left(\frac{1+a}{h}\right)^{\pm\alpha} \frac{c_0 + c_1 z^{-1} + \cdots + c_m z^{-m}}{d_0 + d_1 z^{-1} + \cdots + d_n z^{-n}} \tag{2.99}$$

where $c_i$ and $d_i$ are the transfer function's coefficients of the IIR filter and $m$ and $n$ are the respective nominator and denominator orders which are usually chosen to be the same. The values of $c_i$ and $d_i$ obtained from the CFE are shown in (Vinagre et al. 2003) for different orders $n$.

## 2.7 Conclusion

In the context of modelling the brain-electrode interface, this chapter introduces the state of the art in system identification. The concept of transfer function as a representation of a time invariant linear system is introduced, and time and frequency representations of such systems are discussed.

After the general context on system representation, non-parametric and parametric methods for the identification of these linear systems using input and output data are presented. For the parametric case, types of model structure are discussed depending on the type of disturbance added to the output. Once the parameters of a system are identified, methods for validating the model are presented both based on qualitative and quantitative analysis.

Lastly, because of the use of CPEs in the brain-tissue interface models, the concept of non-integer order derivatives is presented, as well as how they can be integrated with system identification methods.

Now that the general concepts of the state of the art that constitute the base of this thesis were introduced, in the next chapters we propose new methods for brain tissue classification using SEEG signals. The different approaches are based on signal analysis and the modelling of the brain-electrode interface.

Chapter 3

# Brain tissue classification using raw SEEG signals

As previously discussed in chapter 1, the classification of the brain tissue in which the SEEG contacts are inserted in is an important step in the pre-surgical evaluation of drug-resistant epileptic patients. From the fact that only grey tissues can be epileptogenic, white matter contacts are usually not taken into account when it comes to the identification of the EZ. Hence, the miss-classification of SEEG contacts can result in incorrect identification of the area of the brain to be removed in surgery. Moreover, correct tissue classification also has an impact in the case of direct brain stimulation, as stimulating white matter involves different biological processes from the case when stimulating the grey matter.

The vast majority of methods used for brain tissue classification are based on the intensity of the voxels of the co-registration of the MRI and CT scan of a patient. For this, electrodes are manually positioned in the image and labelled with the use of softwares. Alternatively, classification from the MRI can be done visually by the medical team, which is a time-consuming process. Even though these methods are highly efficient and yield good results, there are some disadvantages. The first one is that accurate co-registration procedures may not always be available and thus performed. Additionally, this method depends on the quality of the image, and the correct manual placement of electrodes in it.

There is no way of knowing exactly the accuracy of image based tissue classification methods, from the fact that the ground truth is not available, as there is no way of having a clear inside view of the brain. Therefore, methods for brain tissue classification that do not rely on imaging are of great interest, for the fact that they can be used as a support for the existing imaging methods, in the sense that they offer a different input to be taken into consideration in difficult classification cases. Furthermore, a tissue classification method from typical SEEG signals, could help neurologists with the quick classification of tissues during SEEG procedures.

The field of brain tissue classification using SEEG signals has just now started to be explored. In (Mercier et al. 2017), features such as the power spectra and absolute amplitude of spontaneous brain activity in SEEG are used to characterise differences in white and grey matter signals. However, the authors did not go as far as performing tissue classification. It is only in a more recent study (Greene et al. 2021), that SEEG signals are used directly for tissue classification. In their article, the authors propose a signal approach for tissue classification using bipolar montage and a Bayesian classifier.

In this context, new features to be extracted directly from SEEG signals are proposed in this chapter using both signal analysis and non-parametric frequency domain identification techniques. The power of discrimination between groups of these new proposed features will be compared to the ones proposed in (Greene et al. 2021) considering data recorded from 19 epileptic patients. Prior to this work, the brain tissues for each of the contacts were classified using the MRI of the patients. These previous labels are considered as the ground truth for supervised classification in order to evaluate quantitatively the classification capabilities of the new features.

The results presented in this chapter were published in (M. Machado, Voda, Besançon, Becq, and David 2021), and (M. Machado, Voda, Besançon, Becq, Kahane, et al. 2022).

## 3.1 Data sets

The SEEG signals used in this study were recorded from 19 epileptic patients during standard presurgical evaluation procedures at Grenoble-Alpes University Hospital. The processed patients were adults and suffered from temporal (n=9), frontal (n=6), insular (n=2), temporal/insular (n=1) and temporal/insular/frontal (n=1) epilepsies. The specific information for each patient can be found in Table 3.1. All the patients gave their consent for their data to be re-used by the research protocol F-TRACT (INSERM IRB 14-140).

| Patient | Gender | Age at SEEG | Epilepsy type | Lesion |
|---|---|---|---|---|
| 1 | F | 15 | Left temporal | Left hippocampus malrotation |
| 2 | F | 12 | Left frontal | Left frontal dysplasia |
| 3 | M | 29 | Right frontal | Right frontal tumor leftover and gliosis |
| 4 | M | 28 | Left temporal | Left ventricular heterotopia |
| 5 | M | 28 | Right frontal | Right frontal oligodendroglioma |
| 6 | M | 33 | Left temporal | Left temporal, periventricular nodular heterotopia |
| 7 | F | 42 | Left temporal | None |
| 8 | F | 30 | Right frontal | Right parietal dysembryoplastic neuroepithelial tumor |
| 9 | M | 14 | Right insula | None |
| 10 | F | 39 | Left temporal | Left cortical dysplasia, hippocampal gliosis |
| 11 | M | 33 | Right frontal | Right frontal dysplasia |
| 12 | M | 48 | Right temporal | Right hippocampus atrophy and hypersignal |
| 13 | F | 42 | Right frontal | Cortical dysplasia |
| 14 | M | 49 | Left temporal | Left external temporal post-operatory gliosis |
| 15 | M | 46 | Left insula | Left frontal basal cavernoma |
| 16 | M | 46 | Left temporal and insula | Right hippocampal sclerosis |
| 17 | F | 16 | Right frontal/insula/temporal | Right fronto-parieto-temporal lesions |
| 18 | F | 32 | Right temporal | Right hippocampal sclerosis |
| 19 | M | 34 | Left temporal | Left hippocampal sclerosis |

Table 3.1: Patient information.

For each patient, 6 to 15 electrodes containing each one 5 to 18 contacts have been implanted a week prior to the recordings. The electrodes were manufactured by Dixi Medical (Besançon, France). Each contact was of 0.8 mm diameter and of 1.5 mm long, separated by 3.5 mm (center to center) from the next one (see Fig. 3.1).

SEEG signals have been recorded using a Micromed (Micromed, Treviso, Italy)

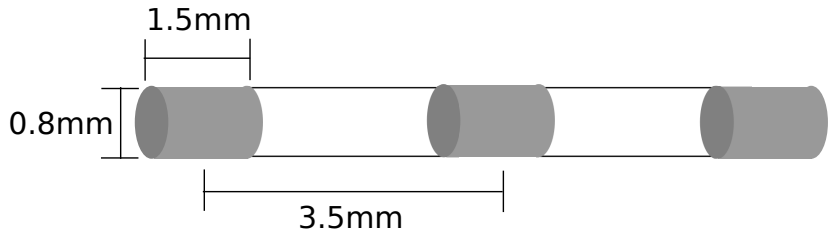


Figure 3.1: Dimensions of SEEG electrodes.

SEEG/video system, coupled to a Micromed programmable stimulator, with a sampling frequency ($f_s$) of either 1024 Hz (for 7 patients) or 512 Hz (for 12 patients) and an acquisition band-pass filter between 0.1 and 200 Hz. Data were acquired using a referential montage, with a reference contact chosen in the white matter, also known as the monopolar montage.

During the SEEG procedure, the contacts can be recorded multiple times at different instances (around 60 different recordings). For each of these, baseline recordings have been selected as 40 s periods of time while the patient was resting, as described in (David, Job, et al. 2013). An example of baseline signals recorded for one of the patients in four consecutive adjacent contacts located in the frontal lobe (the first two in grey matter and the last two in white matter) can be found in Fig.3.2.

For each patient, the brain tissue in which each contact was inserted, was classified using the MRI of the patient, following the labelling procedure described in (Deman et al. 2018) which is based on segmentation methods implemented in the FreeSurfer software. Pre-operative and post-operative MRI were acquired at the isotropic resolution of 1 mm. Post-operative CT-scans were reconstructed at the isotropic resolution of 0.45 mm. Contacts labelling was also visually checked and corrected if necessary. An average of 9 % of the contacts were corrected per patient. The majority of the corrections were from white to grey matter (average of 76 %). Contacts in grey matter were measured in both healthy and pathological tissues.

The signals of disconnected and noisy contacts were classified as bad channels by neurologists following the procedure described in (Tuyisenge et al. 2018) and are eliminated in this study.

## 3.2 Brain tissue classification using SEEG signals in monopolar montage

At first, the most commonly used time and frequency domain features for classification are considered. In this first approach, SEEG signals are used in their original form, in monopolar montage. With this simple study we aim to have a first idea of the complexity of tissue separation task considering SEEG signals. In order to test quantitatively the power of group separation of a feature, a simple classification method considering a linear frontier is consid-

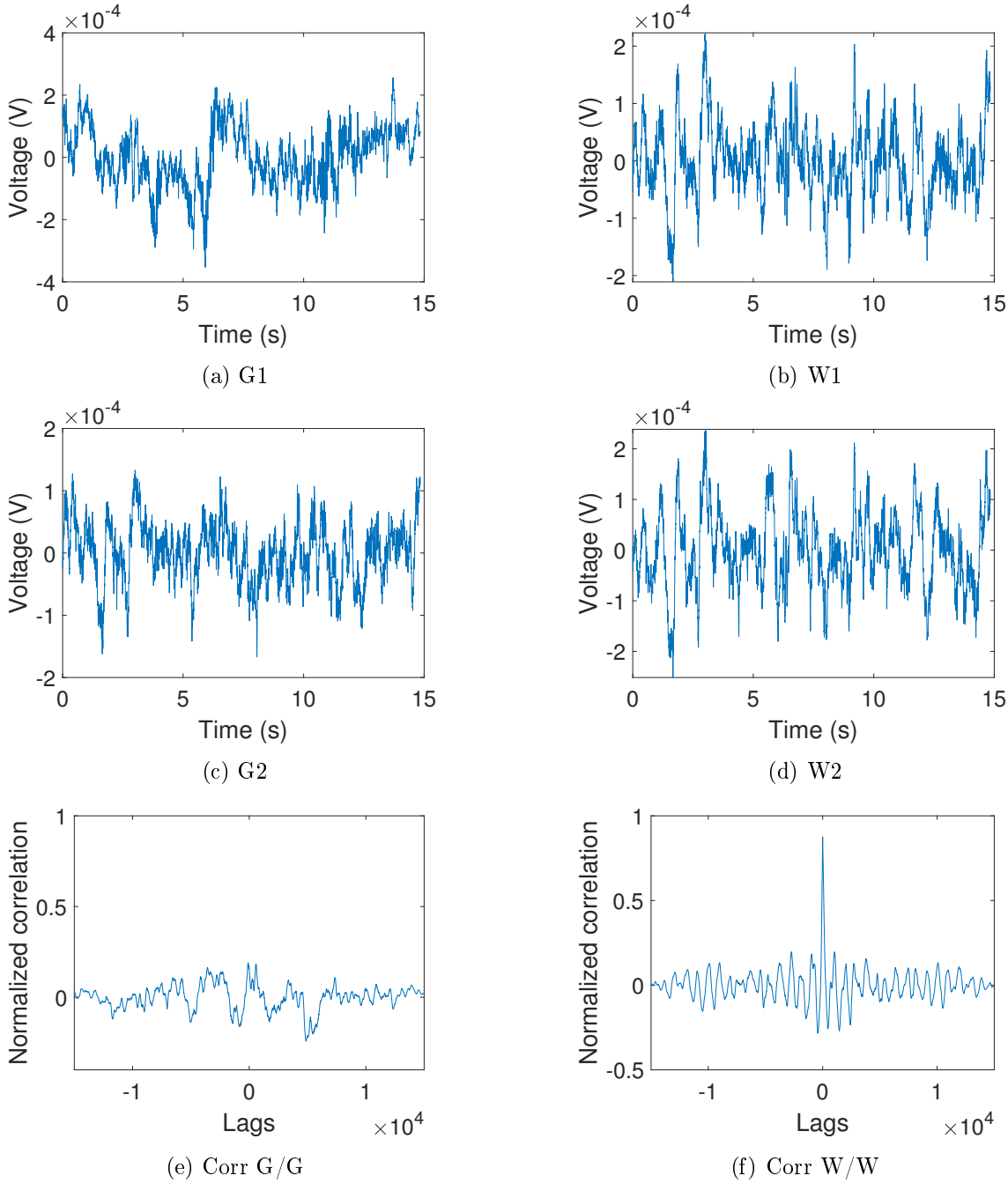


(a) G1 (b) W1

(c) G2 (d) W2

(e) Corr G/G (f) Corr W/W

Figure 3.2: Examples of signals measured in four consecutive contacts in the same electrode shank located in the frontal lobe. The first two in grey matter and the last two in white matter. a) Signal measured in the first contact in grey matter. c) Signal measured in the second contact in grey matter. e) Correlation between the grey matter signals. b) Signal measured in the first contact in white matter. d) Signal measured in the second contact in white matter. f) Correlation between the white matter signals.

ered.

### 3.2.1 Time features

The first features to be extracted from the SEEG signals measured in monopolar montage are the first four moments that describe a statistical distribution, which are mean, variance, skewness, and kurtosis (C. Lee et al. 2000).

The mean of a discrete signal $x(k)$ for $k = 1 \cdots N$ with $N$ the length of the signal, represents the central tendency of a distribution and is calculated as:

$$\mu = \frac{1}{N} \sum_{k=1}^{N} x(k) \tag{3.1}$$

the mean of a normal distribution is zero.

The variance of a distribution, also known as the second statistical moment, represents the dispersion from the mean:

$$\sigma^2 = \frac{1}{N-1} \sum_{k=1}^{N} |x(k) - \mu|^2 \tag{3.2}$$

the variance of a normal distribution is one.

The skewness of a signal $x(k)$ measures the asymmetry of the data around the mean, in other words it measures if the distribution leans to the right or to the left. The skewness value of a normal distribution is zero. It can be calculated as:

$$Skew = \frac{1}{N} \sum_{k=1}^{N} \left[ \frac{x(k) - \mu}{\sigma} \right]^3 \tag{3.3}$$

The fourth moment is called the kurtosis and is related to the outer tails of a distribution. It measures how outlier-prone a distribution is. The value of kurtosis for a normal distribution is 3, if the value is higher than 3 the signal is more outlier-prone. Its equation is given by:

$$Kurt = \frac{1}{N} \sum_{k=1}^{N} \left[ \frac{x(k) - \mu}{\sigma} \right]^4 \tag{3.4}$$

### 3.2.2 Frequency features

The frequency features that are going to be used in this first analysis are based on (Becq, Bonnet, et al. 2011) and (Becq, Kahane, et al. 2013). For each signal, the one-sided power spectral density is calculated using the periodogram method with a rectangular window and zero padding on $N = 10000$ points. It represents the Fourier transform of the biased estimate of the auto-correlation sequence. For a signal $x(k)$, sampled at $f_s$, with $h$ the sampling interval, its periodogram is given by:

$$\hat{S} = \frac{h}{N} \left| \sum_{k=1}^{N} x(k) e^{-j2\pi fhk} \right|^2 \tag{3.5}$$

for $0 < f < f_s/2$. As the one-sided periodogram is considered, the values are multiplied by two except for 0 Hz and the Nyquist frequency. In *Matlab* function *periodogram* is used.

Common features to be extracted from power spectral densities ($\hat{S}$) are the spectral powers of the signals for specific frequency bands:

$$P_b = (f_2 - f_1) \sum_{f \in [f_1, f_2]} \hat{S}(f) \tag{3.6}$$

where $P_b$ is the spectral power of the signal in band $b$ for $f \in [f_1, f_2]$.

The chosen bands for this analysis are five of the typical frequency bands of brain signals (see (Frauscher et al. 2018)): $\delta$ (0.5 - 4 Hz), $\theta$ (4 - 8 Hz), $\alpha$ (8 - 13 Hz), $\beta$ (13 - 30 Hz) and $\gamma$ (30 - 80 Hz).

### 3.2.3 Classification using linear discriminant analysis (LDA)

Different types of classifiers compute different frontier shapes to separate features belonging to each group (Hastie, Tibshirani, and Friedman 2001). Linear and quadratic frontiers can be found with a linear discriminant analysis (LDA), and a quadratic discriminant analysis (QDA) respectively. The support vector machine (SVM) classifier finds a combination of hyperplane frontiers between groups. Other methods such as K-nearest neighbours (KNN), and decision trees define more complex frontiers that are heavily based on data.

Complex methods tend to have the problem of overfitting as they are very data dependent. This is why we chose the simplest method (LDA), as well as for the advantage of a high interpretability.

The LDA method consists in determining a linear frontier for group separation according to the feature values. Assuming normal distribution, the LDA predictor computes the posterior

probability ($\hat{P}(k|x)$) of an element $x$ being a part of a group $k$ (grey or white matter) using Bayes rule with Gaussian distribution density $P(x|k)$ given by:

$$P(x|k) = \frac{1}{((2\pi)^d|\Sigma_k|)^{\frac{1}{2}}} exp\left(-\frac{1}{2}(x-\mu_k)\Sigma_k^{-1}(x-\mu_k)^T\right) \tag{3.7}$$

with $d$ the number of features, and $\Sigma_k$ and $\mu_k$ respectively the covariance and the mean of the features of group $k$. Considering the prior probability $P_k = n_k/n$ of a class $k$ as the number of samples in the class $n_k$ divided by the total number of samples in all classes $n$, and a normalization constant $P(x) = \sum_{k=1}^{n_c} P(x|k)P(k)$ with $n_c$ the number of classes, the posterior probability is given by:

$$\hat{P}(k|x) = \frac{P(x|k)P(k)}{P(x)} \tag{3.8}$$

The classification of an element is done by choosing the group with the highest posterior probability. The linear frontier between the groups represents equal probabilities of a sample being a part of each class $\hat{P}(grey|x) = \hat{P}(white|x)$.

In order to quantify the classification performance, the accuracy rate ($ACC$) is calculated taking into account the previous classification using the co-registration of MRI with CT-scan:

$$ACC = \frac{TP + TN}{TP + TN + FP + FN} \tag{3.9}$$

where $TP$ and $TN$ represent the true positives and true negatives for which the label according to the LDA classifier is the same as the MRI one, and where $FP$ and $FN$ represent the false positives and false negatives for which the labels differ.

All 9 proposed time and frequency domain features were extracted from the signals of the 19 patients (1100 contacts localised in grey matter and 968 in contacts localised in white matter) are used for classification. As the contacts were recorded at several different times, generating several different signals, the features were extracted from each of them, and the final value is given as the average across all signals.

The data set is divided randomly into training (90% of the data) and validation (10% of the data). Once the LDA classifier is trained with the training set, it is used to classify the validation set. The accuracy is obtained by the comparison of the classification of the validation data using the trained classifier, and the original MRI classification. This procedure is repeated 50 times in order to have different combinations of training and validation data. The mean accuracy obtained using the proposed features is $54 \pm 3\%$. This accuracy is small and indicates that the preliminary features proposed are not discriminant enough to separate grey and white groups. Other types of features will be proposed in the sections that follow and their discriminant power is discussed.

## 3.3 Brain tissue classification using non-parametric frequency domain identification

The preliminary study using signals in monopolar montage resulted in bad group separation between tissues. Indeed, in (Greene et al. 2021) the authors conclude that bipolar montage, where the signal of a contact is subtracted from the signal in the adjacent contact, has better results in tissue separation than the common reference montage.

Here, the proposition is to use pairs of adjacent contacts, however not in a bipolar montage. Considering the first contact as the input and the second contact as the output (both in monopolar montage), the non-parametric frequency response can be used to compare gains in different frequencies for different brain tissues. This idea is based on the fact that grey and white matters have different electrical conductivities (see (Geddes et al. 1967), (McCann et al. 2019), (Carvallo et al. 2018), and (Logothetis et al. 2007)). We expect that this difference in resistance should impact at least the gain in small frequencies, and therefore be perceived in the frequency response.

The pairs of adjacent electrodes are formed in the *ascending order*. This means that the first contact of the pair is the shallower one and the second contact is the deeper one on the brain. We call it *ascending order* because the contact number gets higher the deeper it is located. Contact pairing and order is exemplified in Fig. 3.3.

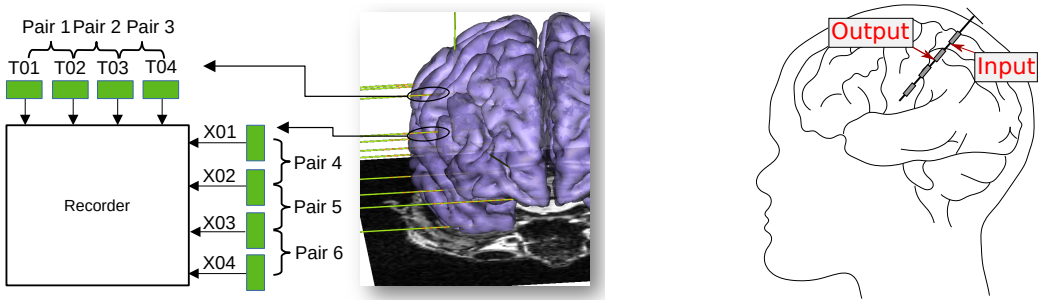


(a) Contacts pairing (b) Contacts order

Figure 3.3: (a) Example of consecutive contacts pairing. (b) Representation of the *ascending order* of contacts

As the contacts are considered by pairs, the anatomical labels defined visually are no longer just "grey" (G) or "white" (W) matter, they are "G/G" for contacts inserted in homogeneous grey matter, "W/W" for contacts in homogeneous white matter, and "G/W" and "W/G" for contacts in heterogeneous brain matter. For the purpose of tissue classification, only pairs of contacts in homogeneous tissues are considered. Contact pairs in heterogeneous tissues are harder to separate from other groups as the amount of each tissue is variable from pair to pair.

### 3.3.1 Frequency response identification

In this work, the frequency responses are estimated using Spectral Analysis (SPA). This non-parametric method was presented in section 2.2, and it is re-stated here:

$$\hat{G}_{SPA}(e^{i\omega}) = \frac{\hat{\Phi}_{yu}(\omega)}{\hat{\Phi}_{u}(\omega)} \tag{3.10}$$

with $\hat{\Phi}_{V_2V_1}(\omega)$ the Fourier transform of the cross-covariance, and $\hat{\Phi}_{V_1}(\omega)$ the Fourier transform of the covariance.

The frequency responses of the contact pairs of all 19 patients are calculated with *Matlab*, using the *spa* function, and a Hanning window of size 18 s for sampling frequency 1024 Hz, or 36 s to the sampling frequency 512 Hz, and a frequency resolution of 1 Hz, corresponding to frequency points which are equally spaced between 0 Hz and the Nyquist frequency $f_s/2$ (with $f_s$ either 1024 Hz or 512 Hz).

Since data from several recordings are available (around 60 recordings for most patients), in which, for each of them, the same contacts were used to measure brain activity at different times, one can obtain a smoother frequency response of a contact pair by taking the mean of the frequency responses over different recordings (see chapter 6 of (Ljung 1998)).

The mean of the identified frequency responses of contact pairs for each homogeneous group considering the patients with $f_s = 1024$ Hz is shown in Fig. 3.4. The frequency responses of baseline signals have been obtained from 1284 contact pairs (486 with $f_s = 1024\,Hz$, and 798 with $f_s = 512\,Hz$). The distribution of pairs per patient is 35±12 for the G/G group and 32±14 for the W/W group. The trend of the data was removed via the substraction of a polynomial straight-fit line approximation via the Matlab function *detrend*.

From a visual inspection, the magnitude of the two different groups are clearly separated, specially for frequencies from 1 Hz to 100 Hz.

The phase is not discriminating between grey and white matters for low frequencies, and high frequencies are affected by noise. Therefore, the magnitude is a more robust measure and will be considered for the remainder of our study.

The next step here would be to determine which features should be extracted from the magnitude of the frequency responses in order to perform tissue classification.

### 3.3.2 Feature extraction

In order to classify the brain tissue from the identified frequency responses, information must be extracted in the form of features. Here, two different types of features are chosen that quantify the magnitude of the frequency responses in specific frequency bands.

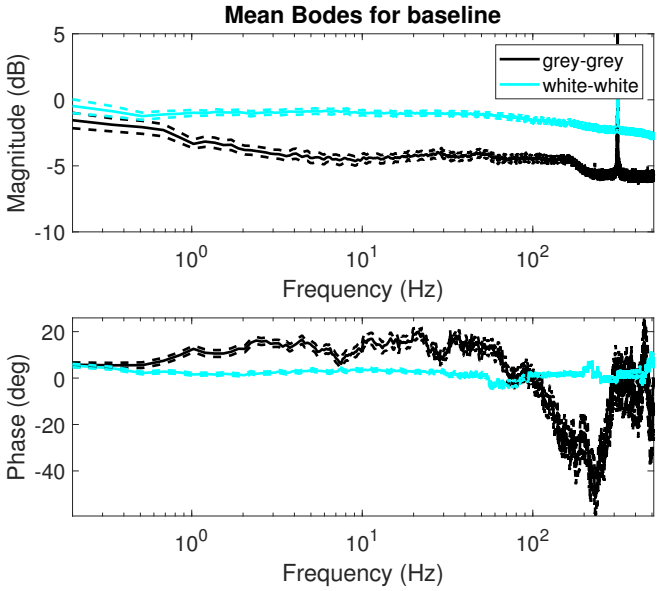


Figure 3.4: Mean frequency response obtained for each group (G/G in black and W/W in cyan). The discontinuous lines correspond to the standard error of the mean for each group.

The first type of feature to be used is the mean square of a specific frequency band. In a band $i$ ($f_1^i \leq b_i \leq f_2^i$), the mean square ($MS$) magnitude can be given as the sum of the squared magnitude values $\hat{M}_{SPA}(f_j)$ (see equation (2.19)) for every frequency $f_j \in [f_1^i, f_2^i]$ according to the sampling time $T_s$, divided by the number of points ($N_i$) in the frequency band $b_i$:

$$MS\,b_i = \frac{1}{N_i} \sum_{f_j \in [f_1^i, f_2^i]} \hat{M}_{SPA}^2(f_j) \tag{3.11}$$

The second type of feature chosen here is the relative mean square of a specific frequency band. Once again, given the magnitude of a specific frequency band ($f_1^i \leq b_i \leq f_2^i$), the relative mean square ($MS_r$) is equivalent to the $MS$ of the considered band $b_i$ divided by the $MS$ of the total frequency band ($0\,Hz \leq b \leq f_s/2\,Hz$):

$$MS_r\,b_i = \frac{MS\,b_i}{MS\,b} \tag{3.12}$$

Looking at the frequency responses in Fig. 3.4, there are two main frequency bands for which the magnitudes have more or less the same behaviour ($0\,Hz \leq b_1 < 30\,Hz$, and $30\,Hz \leq b_2 \leq 200\,Hz$). Thus, the four features used for tissue classification using only baseline signals are the $MS$ and $MS_r$ for these two bands ($MS\,b_1$, $MS\,b_2$, $MS_r\,b_1$, and $MS_r\,b_2$).

### 3.3.3 Tissue classification

The proposed features were extracted from the 1284 pairs across all 19 patients. All contact pairs with at least one feature with value higher than three scaled median absolute deviations of the feature across all pairs, is considered an outlier and is eliminated. The observed outliers are due to noise commonly observed in electronic measurements. This results in 1058 pairs to be used for classification. The combination of features can be seen in Fig.3.5. From the histograms of each feature, $MSb_1$ and $MSb_2$ seem to be the most discriminant ones.

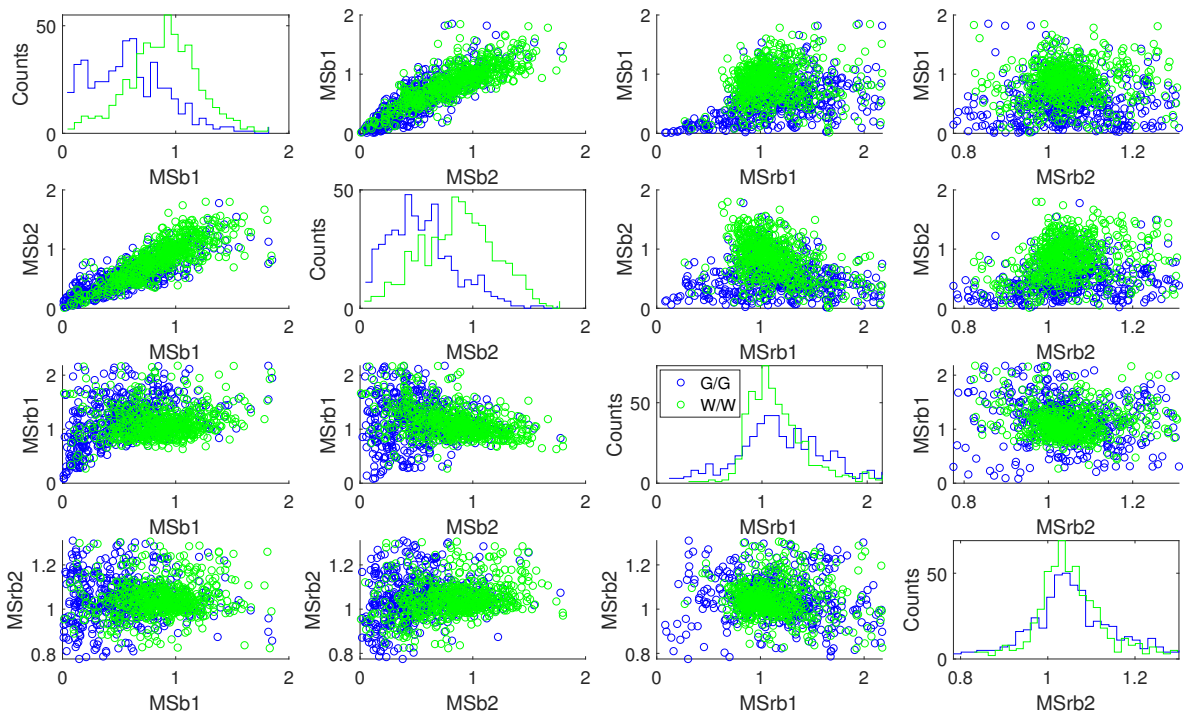


Figure 3.5: Features extracted from the frequency responses proposed in this study. MSbi, and MSrbi indicate the mean square maginitude and the relative mean square magnitude at band $b_i$ respectively.

Similar to the case of tissue classification using features from monopolar signals, the classifier of choice here is the LDA. This choice is made not only from the fact that this classifier is easy to interpret, but also it seems like a good fit giving the feature distribution in Fig. 3.5.

Moreover, the posterior probabilities of equation (3.8) might allow us to create a probability map that gives an idea of the percentage of each brain matter between two consecutive contacts (the percentage of grey matter is represented by the posterior probability of G/G, and the percentage of white matter is represented by the posterior probability of W/W). This solution is close to the idea of proximal tissue density proposed by (Mercier et al. 2017), in which the author used the MRI of patients to quantify the amount of each brain tissue present in a given region using the number of grey and white matter voxels in the contact proximity. In our case this would be done using the posterior probabilities from the prediction using the classifier.

The overall procedure for tissue classification is shown in Fig. 3.6. For the classifier training, only the contacts in homogeneous matter have been considered. Once the classifier is trained, all possible contact pairs (homogeneous and heterogeneous) are classified and posterior probabilities are calculated with equation (3.8). This posterior probabilities are studied for each group previously classified (G/G, W/W, G/W, and W/G according to MRI) as they might provide some insight into the tissue composition between contact pairs. We expect higher posterior probabilities for the previously classified homogeneous groups than for the heterogeneous groups.

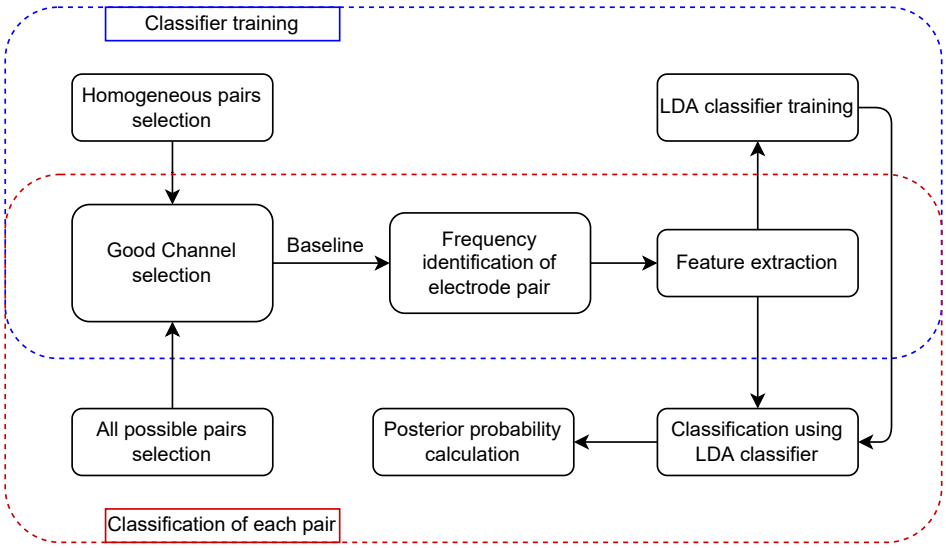


Figure 3.6: Tissue classification procedure from the classifier training to tissue classification.

The LDA classifier is trained with 90 % of data. This procedure was repeated fifty times, changing the training set each time, in order to guarantee robustness. After each classifier has been trained, the remaining 10 % of data are used for prediction. The labels from the LDA classifier are compared to the original labels given from the MRI of the patient in order to calculate the classification accuracy, using equation (3.9).

The overall accuracy using only baseline signals is $72 \pm 3\,\%$ for the separation of homogeneous groups. The confusion matrix obtained comparing the predicted classes to the MRI classification, is presented in Fig. 3.7. The distribution of G/G and W/W pairs is almost uniform (52 % of G/G pairs and 48 % of W/W pairs). Classifier sensitivity, also known as the ability of the classifier to correctly classify G/G pairs is 0.726. The classifier specificity, or the ability to correctly classify W/W pairs is 0.718. Therefore, the classifier has the ability of classifying both true positives and true negatives.

### 3.3.4 Analysis on tissue composition

Considering all pairs (homogeneous and heterogeneous ones), an analysis can be done using posterior probabilities as an indicator of tissue composition. The posterior probability value

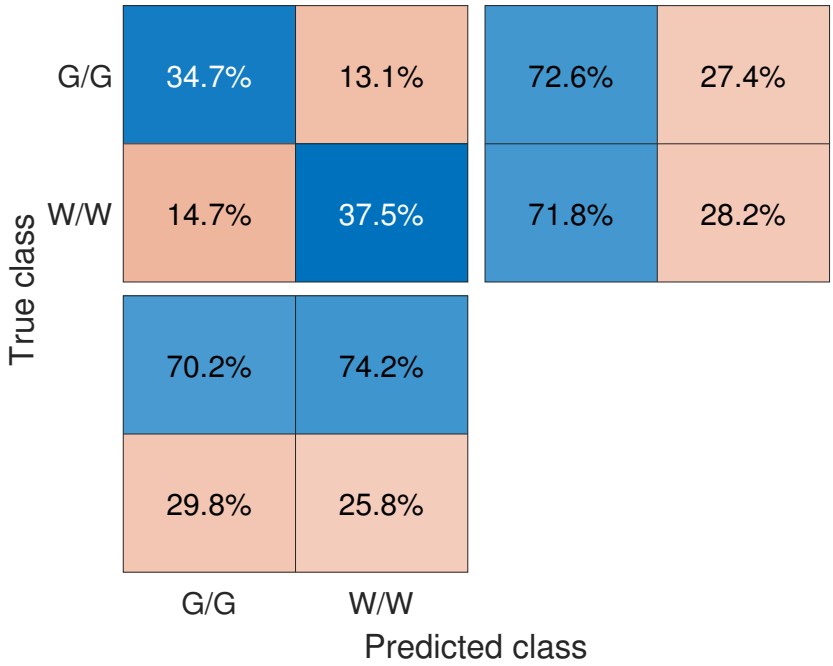


Figure 3.7: Confusion matrix comparing the predicted class obtained via the LDA classification with the true class obtained with the MRI. The matrix in the right contains the row summary, which represents the percentage of the samples of each of the two true classes that were correctly classified in blue and wrongly classified in red. The matrix in the bottom contains the column summary, which represents the percentage of samples of each of the two predicted classes that were correctly classified in blue and wrongly classified in red.

indicates how likely a pair is of being part of the first group (G/G) or the second group (W/W). The higher the probability of a pair belonging to G/G should indicate that there should be more grey matter between the contacts of the pair, so on and so forth. Here, the probabilities of each pair belonging to G/G and W/W according to the new classifier are compared with their previous MRI classification. The results are shown in Fig. 3.8.

As expected, looking at Fig. 3.8a, the contact pairs previously classified as G/G by the MRI have the highest posterior probabilities of belonging to the G/G group ($\hat{P}(G/G|x)$), and the smallest posterior probabilities of belonging to the W/W group ($\hat{P}(W/W|x)$). Exactly the same behaviour can be noticed for the pairs previously classified as W/W by the MRI. For the previously classified heterogeneous pairs G/W, and W/G, both $\hat{P}(G/G|x)$, and $\hat{P}(W/W|x)$ have values in between the posterior probabilities observed for the homogeneous groups.

In Fig. 3.8b it can be seen that approximately 74 % of the contact pairs previously classified as G/G by the MRI have larger values of $\hat{P}(G/G|x)$ than $\hat{P}(W/W|x)$. For the previously classified W/W pairs by the MRI, 71 % have higher $\hat{P}(W/W|x)$ than $\hat{P}(G/G|x)$. For both cases the majority of pairs have probabilities between 60 % and 80 %. For the heterogeneous pairs previously classified as G/W, there is in general higher $\hat{P}(G/G|x)$ than $\hat{P}(W/W|x)$ (58 % of pairs with higher $\hat{P}(G/G|x)$ against 45 % with higher $\hat{P}(W/W|x)$). For the W/G case

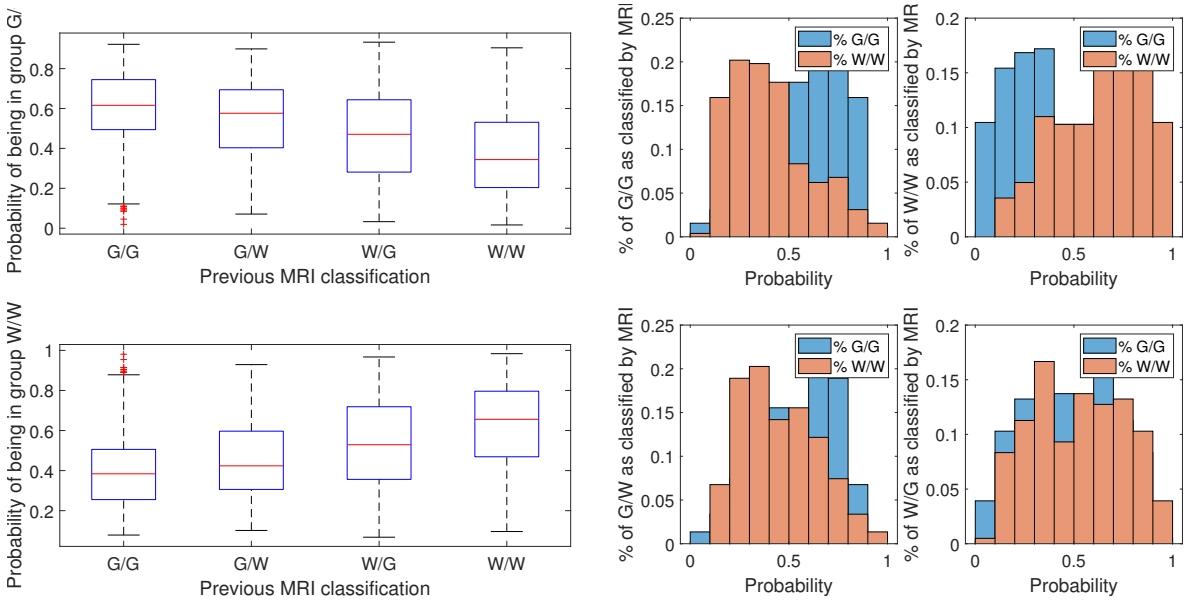


(a) Boxplot (b) Histograms

Figure 3.8: Posterior probability study of each contact pair belonging to the homogeneous groups G/G and W/W (according to the baseline LDA classifier), depending on their label from the MRI tissue classification. (a) on top posterior probabilities of a pair belonging to the G/G group are shown as a function of the MRI classification of the pair. On bottom, the same analysis for the posterior probabilities of being in the W/W group. (b) represents the distribution of each of the previously classified groups according to MRI in therms of the posterior probabilities for both G/G and W/W groups.

both $\hat{P}(G/G|x)$ and $\hat{P}(W/W|x)$ have a similar distribution (50 % of pairs classified as G/G and 50 % classified as W/W).

In general, the results show that the contact pairs have a higher probability of being in grey matter than white matter (51 % of all possible contact pairs were classified as being a part of the G/G group as opposed to 49 % of the W/W group). This is consistent with the reality, where 52 % of the measured contacts are in grey matter as opposed to 48 % in white matter.

In Fig.3.9 an example of the implanted contacts positions for one patient is shown. The dark blue contacts are inserted in grey matter, the light blue contacts are inserted in white matter, and the yellow contacts are not in brain matter. What can be seen in the plot on the right is that the measured contacts (in red) are all located closer to grey matter. The vast majority of consecutive contacts in white matter is actually not recorded. Contacts recorded in white matter on the centre of the brain are easy to classify in MRI images, and are the ones for which the certitude of classification is higher. Unfortunately, most of the white matter contacts used in this study are not the ones located with the higher certainty, most of them being close to grey matter. Thus, even though the fact that most contacts are located in the boarders of grey and white matter could justify the miss-classifications, we have limited

information on the possible use of the posterior probabilities as a direct measurement of the amount of each tissue in between two contacts. For that, more data in distant white matter should be considered.

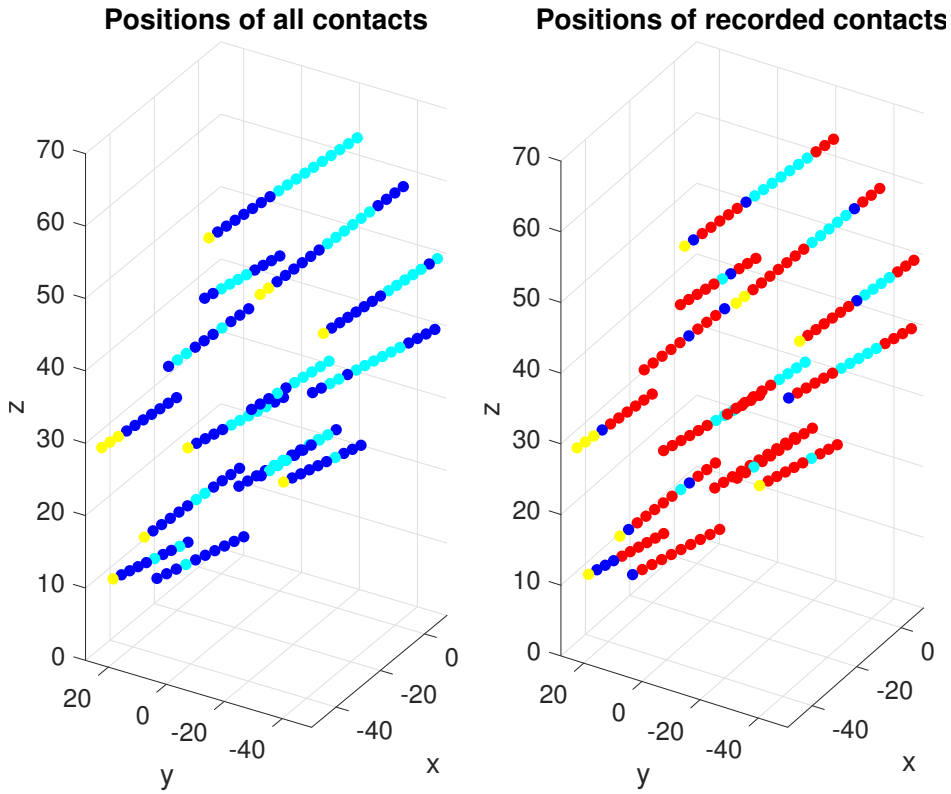


Figure 3.9: Contacts position in coordinates (x,y,z). The dark blue represent contacts in grey matter, the light blue represent contacts in white matter, and the yellow represent contacts not in brain matter. On the right the red colour refers to the recorded contacts in one measuring session.

The classifier as it is in this study, is more appropriate for support decision to coregistration of CT scan (with implanted SEEG electrodes) with preoperative MRI. The method can be implemented in routine SEEG software, to do a first pass of contact classification.

### 3.3.5 Comparison with literature

As mentioned before, brain tissue classification using SEEG signals has only been done before in one other study ( see (Greene et al. 2021)). In it, the authors propose two different features to be extracted from SEEG signals in bipolar montage and the position of the contacts. The first of them is the average shift in the power spectrum compared to the average power spectrum over all contacts (in log scale) in the band [1, 150] Hz. The second feature is the normalised distance between the contact in question and the most peripheral contact on the shaft. However, the classification method used by the authors is different from the one used in this study. If one wants to compare the discrimination abilities of the features proposed

here with the ones proposed in (Greene et al. 2021), the same classification method needs to be applied and the accuracy must be calculated considering the same patients.

Hence, the two features proposed in (Greene et al. 2021) are calculated with the signals from the 19 patients of this study using the bipolar montage, where the same adjacent contact pairs are used, but in this case, the signal of the second contact is subtracted from the first one. As the bipolar montage is used, the resulting label should also be a combination of the two contacts. As in our study, only homogeneous combinations were considered and outliers were removed.

The resulting accuracy using the features proposed by (Greene et al. 2021) with the LDA classifier is $60 \pm 4\%$. The distributions of the features proposed in (Greene et al. 2021) are shown in Fig. 3.10.

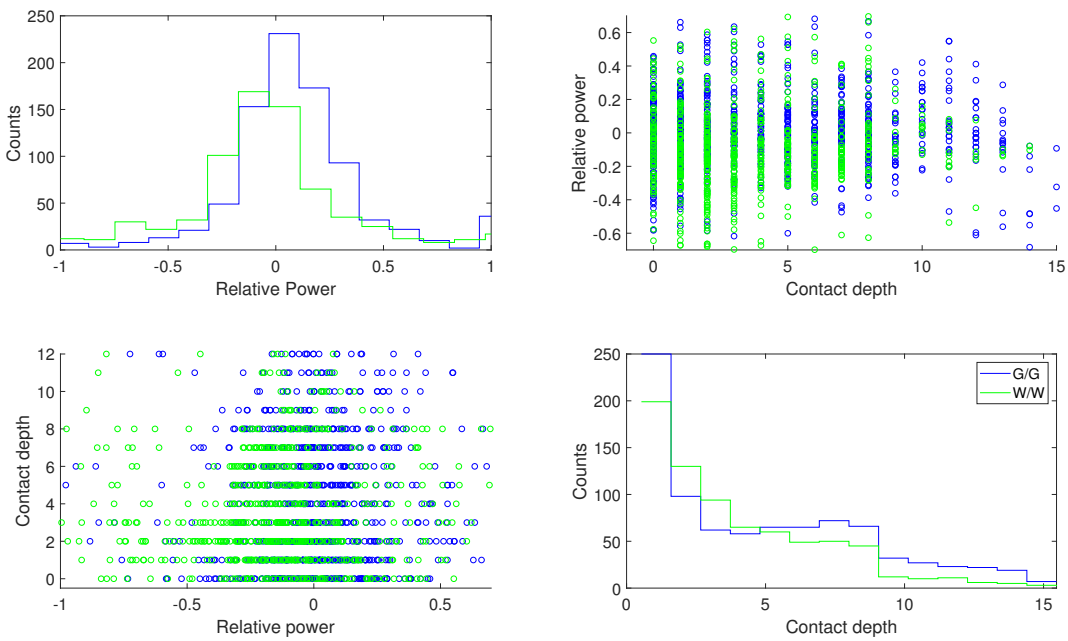


Figure 3.10: Distribution of the features extracted from signals in bipolar montage as proposed by (Greene et al. 2021).

From the accuracy obtained with the LDA classifier and looking at the histograms of the features proposed by (Greene et al. 2021), the ones proposed in this study considering frequency responses seem to be the most discriminant. However, the Bayesian classification method proposed by (Greene et al. 2021) in which the brain structure and uncertainties of parameters are considered, is more complete than the LDA one. It would be interesting as a perspective to test the accuracy of the features proposed here considering the Bayesian classification method proposed by (Greene et al. 2021).

### 3.3.6 Effect of order of contacts

As mentioned, in order to calculate the frequency response of a pair of contacts, one of the contacts is considered as the input and the other is considered as the output. The choice was made to consider contacts in an *ascending* order, in which the first contact is the shallower one, and the second is the deeper one on the shaft. To see the effect of choosing the *descending* order, Fig. 3.11 shows the difference on the frequency responses depending on the order the contacts are considered for two pairs (one in homogeneous grey matter and one in homogeneous white matter).

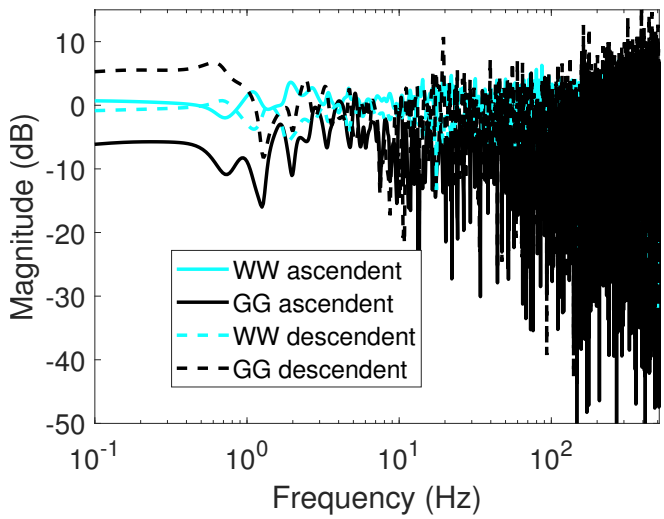


Figure 3.11: Difference in frequency response depending on the contact order for one measurement session considering two different pairs of contacts (one G/G and the other W/W). Grey matter frequency responses are represented in black, and white matter ones are in cyan. The discontinuous lines represent the responses inverting the order of the contacts.

It can be seen that the gain in white matter remains close to zero in small frequencies independently on the order of contacts. The static gain in grey matter however, goes from negative dB values to positive dB values. The gain is the ratio of the Fourier transforms of the cross-covariance and covariance of the voltage of the two contacts. Thus, the fact that the gain in white matter is close to 0 dB (or 1) for both *ascending* and *descending* orders, suggests that signals of the W/W group are more correlated than the signals in G/G. This can be confirmed by looking at Fig. 3.2e and Fig. 3.2f.

For the *ascending* order, the gain for the G/G group is smaller than 1 (0 dB) it means that the second voltage is smaller in amplitude than the first one. For the *descending* order, where the deeper contacts are considered first, the static gain for the G/G pair is higher than than 1 (0 dB), thus the voltage of the second electrode is bigger than the first one. This indicates that the deeper into the brain the contact is, the smaller the voltage in grey matter.

### 3.3.7 Effect of epileptic tissue

In literature (McCann et al. 2019), and (Akhtari et al. 2006), it has been shown that the conductivity of epileptic tissues differs from healthy grey and white matter. This fact might affect the frequency responses and induce bias in the classification.

To see the effects of epileptic tissue in the classification method proposed here, the pairs located in epileptic networks are taken into consideration. In order to do so, a spike detector (Roehri et al. 2019) was used with default parameters to obtain a spike rate for each channel in the bipolar montage. The spike rate was normalised for each patient, which is equivalent to subtracting the average and dividing by the standard deviation of all pairs. Contact pairs with a normalised spike rate greater than three times the median of spike rates across all patients were considered to be in an epileptic network. A total of 59 G/G pairs (9 %), and 80 W/W pairs (13 %) were considered as being in epileptic networks across all patients.

In Fig. 3.12, the distribution of features is shown superposed by features obtained by pairs of contacts in epileptic networks.

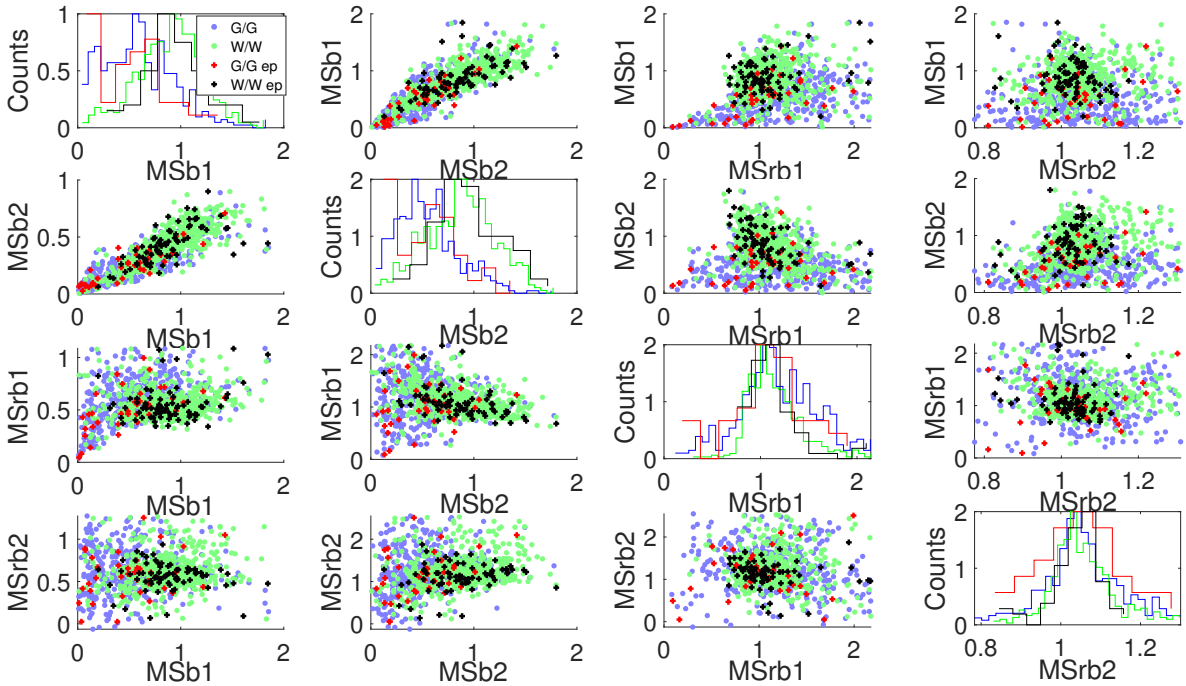


Figure 3.12: Distribution of features depending on the pair classification considering pairs in normal tissue: G/G in blue and W/W in green, and epileptic tissues (with higher spike rates): G/G ep in red and W/W ep in black. MSbi, and MSrbi indicate the mean square maginitude and the relative mean square magnitude at band $b_i$ respectively.

For both the G/G and W/W pairs, the distribution is similar considering the healthy tissues and tissues with a high spike rate. It is also important to note that pairs with high spike rate account for only 22 % of the outliers. In order to quantify the effect of these contact pairs in the brain tissue classification, a new LDA classifier is trained considering only

electrodes in healthy tissue. The accuracy obtained for the classifier is 72± 1%. This means that the areas with high spike rates do not affect the classification.

### 3.3.8 Brain region effect

In SEEG, the electrodes are not always placed in the same brain regions. Their implantation is done considering prior knowledge of where the epileptic zones should be located. Thus, it would be interesting to see if the distribution of features would change depending on the brain region the pair of contacts is inserted in. In order to do so, the contact pairs are grouped by brain regions according to *MarsAtlas* (Auzias et al. 2016) (cingular, frontal, insula, occipital, orbito-frontal, parietal, temporal). Each of these groups are separated between G/G and W/W pairs according to the MRI classification. Finally, the median value of each feature is calculated for each sub-group, and is plotted against the feature distribution map in Fig. 3.13.

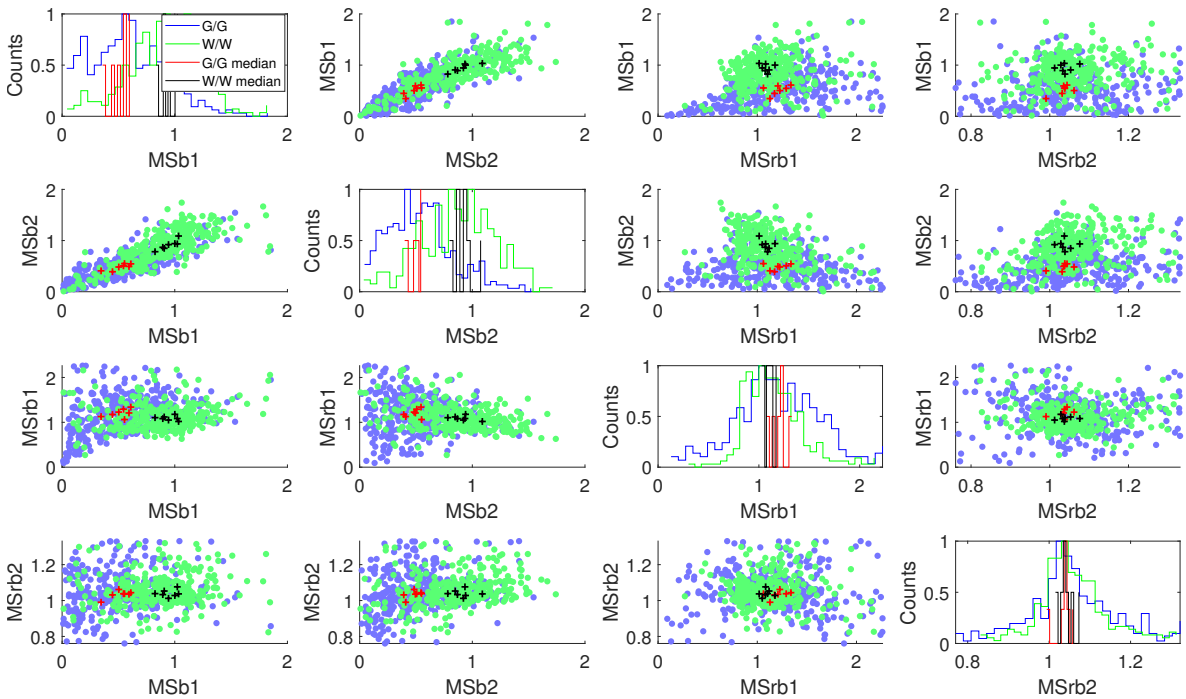


Figure 3.13: Distribution of features for each pair depending on its MRI classification: G/G in blue and W/W in green. Considering the G/G and W/W groups separately, the contact pairs that belong to the same brain region are grouped, and the median of each feature is calculated for each brain region. The superimposed crosses represent the median values of features classified as G/G in red or W/W in black depending on which of the 7 brain regions the contact pairs were inserted in. MSbi, and MSrbi indicate the mean square maginitude and the relative mean square magnitude at band $b_i$ respectively.

When looking at the first feature $MSb_1$, the median values for the G/G and W/W contact pairs are well separated for all of the regions. Thus, the features are discriminant independently of the brain region the signals are measured on.

In order to have a better idea of the impact of the brain regions in tissue separation, the classifier obtained considering all pairs is used in each of the regions separately. The results considering the G/G classification as the positives and the W/W classification as the negatives are given in Table 3.2.

| | TP | TN | FP | FN | Accuracy (%) |
|---|---|---|---|---|---|
| Cingular | 24 | 21 | 5 | 6 | 80% |
| Frontal | 76 | 52 | 19 | 32 | 72% |
| Insula | 5 | 3 | 1 | 1 | 80% |
| Occipital | 37 | 28 | 3 | 11 | 82% |
| Orbito-frontal | 19 | 18 | 7 | 4 | 77% |
| Parietal | 6 | 17 | 2 | 4 | 79% |
| Temporal | 103 | 67 | 36 | 44 | 68% |

Table 3.2: Study of classification according to brain region. The positives correspond to the G/G group, and the negatives to the W/W group.

It can be seen that the accuracies obtained for each brain region are high, proving once again that the classification can be used independently of the region. However, the accuracies obtained for the frontal and temporal regions of the cortex, even though high, are smaller than the accuracies of the other ones. There is no evident reason as to why this difference occurs. It could indicate a higher miss-classification rate on these specific regions of both grey and white tissues (in both cases about 30% of G/G and W/W samples were miss-classified). In order to verify that, more data needs to be gathered from other patients.

## 3.4 Other possible features for brain tissue classification

The first approach for tissue classification using SEEG signals presented in section 3.2 used only simple time and frequency domain features. Even though the features based on frequency responses proposed in section 3.3 achieve good results for brain tissue classification, there are still many other features that could be explored using monopolar referenced signals.

In this context, I supervised the work of Pedro Lopes to study other time and frequency domain features for tissue classification using monopolar signals commonly used when studying epileptic signals (see (Boonyakitanont et al. 2020), and (Sharmila et al. 2018)) as a part of an internship from January 2021 to June 2021. The results were published in (Lopes et al. 2021). We also tested different classification algorithms other than the LDA, that are presented hereafter.

### 3.4.1 Time and frequency domain features

For time domain features, other than the first four statistical moments already presented, (Lopes et al. 2021) also proposed the use of the mean absolute value, and the coefficient of variation ($CV$) for data dispersion:

$$CV = \sigma/\mu \tag{3.13}$$

The first ($Q_1$) and third ($Q_3$) quartiles were also proposed as features. A quartile is obtained by ordering the data and separating it in four equal parts, $Q_1$ corresponds to the data value at 25 % of the ordered sample and $Q_3$ corresponds to the data value at 75 % of the ordered sample. With these values, the inter-quartile range can be calculated:

$$IQR = Q_1 - Q_3 \tag{3.14}$$

In addition, considering $x(t)$ as the SEEG signal of $N$ samples the energy of the signal was calculated as:

$$energy = \sum_{k=1}^{N} x^2(k) \tag{3.15}$$

its average power was calculated as:

$$avr_{pow} = energy/N \tag{3.16}$$

and the root mean square power was calculated as:

$$rms_{pow} = \sqrt{avr_{pow}} \tag{3.17}$$

In the same line of features related to the energy of the signal, the nonlinear energy ($NE$) can detect formant AM-FM modulations with the following equation:

$$NE = \sum_{i=1}^{N-2} x^2(i) - x(i+1) \cdot x(i-1) \tag{3.18}$$

Another feature largely used in epilepsy for seizure detection is line length ($L$) which determines the fractal dimensionality of a signal:

$$L = \sum_{i=1}^{N-1} |x(i) - x(i-1)| \tag{3.19}$$

Shannon entropy was also calculated, and represents the information or the uncertainty of a signal. Considering $p_i$ the probability of occurrence of each value in the signal, Shannon entropy is given as:

$$ShEn = -\sum_{i} p_i log(p_i) \tag{3.20}$$

Hurst Exponent ($H$) is related to the dependence of values in a time series, acting as a long-term memory. For $0.5 < H < 1$, consecutive values in time series are long-term related, and $0 < H < 0.5$ indicates a switch between high and small consecutive values. For self-similar time-series, $H$ is also related to fractal dimension. There are many ways to estimate $H$, here the *Matlab* function *wfbmesti* is used, which calculates the linear regression of the logarithmic plot of variance of detail versus level of wavelet signal decomposition, as proposed by (Flandrin 1992).

The other two time features proposed are the number of zero crossings, and the number of slope sign changes.

In addition, in (Lopes et al. 2021) frequency domain features were also proposed using spectral density estimates of the signals via modified periodograms:

$$\hat{P}(f) = \frac{T}{N_w} \left[ \sum_{n=0}^{N_w-1} h_n x_n e^{-j2\pi fTn} \right]^2 \tag{3.21}$$

with $T$ the sampling time, and $h_n$ a Hamming window of size $N_w$. These spectral density values were used to calculate the RMS power of five typical frequency bands of brain signals (see (Frauscher et al. 2018)): $\delta$ (0.5 - 4 Hz), $\theta$ (4 - 8 Hz), $\alpha$ (8 - 13 Hz), $\beta$ (13 - 30 Hz) and $\gamma$ (30 - 80 Hz).

### 3.4.2 Classification methods

In (Lopes et al. 2021) these features were used to train six different classifiers that are all described in (Hastie, Tibshirani, Friedman, and Friedman 2009). The first proposed classifier was decision tree, which is composed by a starting node, that creates intermediate nodes from binary partitions until terminal nodes are reached. For this case, the partitions are based on the Gini Index. The assigned class to a sample is the one most present in the terminal nodes. Using decision trees as a base, the second method for classification tested in (Lopes et al. 2021) is the random forest. In it, $n$ decision trees are bagged, each one of them is trained

separately, the final class of a sample is the one with the largest number of votes across all trees. The number of trees used was $n = 150$ out of trial and error.

The next classifier tested was the K-Nearest Neighbour. Considering the labels of the training data, in order to label a test sample, the $K$ nearest training samples are selected and the label most present between them is defined as the new sample label. For this case, the $K = 11$ nearest neighbours were calculated using the euclidean distance.

Support Vector Machine (SVM) was the fourth method used for classification. It consists in the linear separation of groups in a feature space. The support vector is composed by the closest samples to the frontier. In the case where features can not be separated linearly, a kernel function is used to transform the feature space into a higher dimension one. From different performed tests, the linear kernel function was chosen.

For the fifth method, the Naive Bayes classifier was used. This classifier calculates the posterior probabilities according to the Bayes rule. Considering the class index of an observation $Y$, $\pi(Y = k)$ is the prior probability that a class index is $k$, and considering a vector of $p$ features $feat = [f_1, \cdots, f_p]$, the posterior probability according to Bayes rule is given as:

$$P(Y = k|f_1, \cdots, f_p) = \frac{\pi(Y = k)\Pi_{j=1}^{p} P(f_j|Y = k)}{\sum_{k=1}^{K} \pi(Y = k)\Pi_{j=1}^{p} P(f_j|Y = k)} \tag{3.22}$$

The class assigned to the new sample is the one with the highest posterior probability.

Finally, the last classification method tested was the artificial neural network. A neural network is formed by an input layer of as much neurons as the number of features, intermediate hidden layers formed by one or more neurons, and a single output layer. The idea is to adjust the weights at each node in order to minimise a cost function. For the case of binary classification, the lost function of choice is the cross-entropy function and the chosen optimisation algorithm is the stochastic gradient descent with momentum. The network configuration used in this case consists of a fully connected layer with 32 neurons (number obtained via trial and error). The output layer has a *softmax* transfer function to assign a probability of a sample belonging to each class.

### 3.4.3 Classification results

The 6 different classification methods were trained using all of the 23 features. The data was split into $K = 4$ different subsets. $K - 1$ of such subsets were used for the classifier training, and the remaining one to validation. This process is repeated until all possible combinations of test and training subsets are used. The final evaluation consists in the mean evaluation over all combinations. This process is repeated 20 times to get a more robust estimation of the classifiers performance.

The chosen evaluation metrics in (Lopes et al. 2021) to quantify the performance of the

classifier were: Accuracy, area under curve (AUC) of the operating characteristics (ROC) and $F_1$-Score. Here, to compare with the previously proposed features, the emphasis will be given to the accuracy values.

In (Lopes et al. 2021), only 3 patients were used in the analysis, which accounts for 275 contacts in grey matter and 223 contacts in white matter. The accuracies obtained for the 3 patients using the different classification methods are shown in Table 3.3. In order to compare between the features proposed in (Lopes et al. 2021) and the features obtained from the frequency responses, they need to be extracted from the same patients. Thus, the same classification procedures described in (Lopes et al. 2021) and presented in this section are applied to the data of the 19 patients used for the non-parametric frequency response study. For the 19 patients there are 1100 contacts in grey matter, and 968 contacts in white matter. The results are also presented in Table 3.3.

| Algorithm | Accuracy for 3 patients (%) | Accuracy for 19 patients (%) |
|---|---|---|
| Decision Tree | 66.34 ± 2.11 | 60.02 ± 0.98 |
| Random Forest | 74.03 ± 1.02 | 66.9 ± 0.59 |
| KNN | 69.86 ± 1.12 | 63.26 ± 0.74 |
| SVM | 72.03 ± 0.68 | 60.5 ± 0.54 |
| Naive Bayes | 56.90 ± 0.81 | 48.78 ± 0.17 |
| Neural Network | 69.69 ± 1.70 | 56.36 ± 2.99 |

Table 3.3: Inter-patient performance of classifiers for the three patients used in (Lopes et al. 2021) and the 19 patients used in this study

It can be seen from the results in Table 3.3, that the best performing classifier for both 3 and 19 patients was the random forest one. For the 3 patients case the accuracy achieved is $74.03 \pm 1.02\%$ and for the 19 patients case it is $66.9 \pm 0.59\%$. This results show that higher accuracies can be obtained when considering features extracted from non-parametric frequency domain identification when compared to features extracted directly from monopolar signals.

## 3.5 Conclusion

In this chapter, the concept of brain tissue classification using SEEG signals was introduced. From the fact that the vast majority of the techniques for brain tissue classification rely on the co-registration of the MRI and CT scan of a patient, there is a lot of exploration that can be done when it comes to alternative classification methods.

Hence, in this chapter brain tissue classification was proposed using features extracted either from raw SEEG signals or from the non-parametric frequency response of paired contacts. At first, a preliminary study was made considering simple time and frequency domain features extracted from signals in monopolar montage (or common reference). An LDA classifier was trained with the features extracted from 19 epileptic patients and an accuracy of $54 \pm 3\%$ was achieved. From the poor results obtained using the first proposed features, a new strategy

was suggested for brain tissue classification with the use of non-parametric frequency response identification of pairs of consecutive contacts. The idea was based on the differences of conductivity between grey and white matter. This second study, resulted in a $72 \pm 1\%$ accuracy for homogeneous group separation using the data from the 19 epileptic patients and an LDA classifier. Finally, in a parallel study that I supervised and conducted by Pedro Lopes, more complex features were extracted from the monopolar SEEG signals based on previous studies on epileptic signals (see (Boonyakitanont et al. 2020), and (Sharmila et al. 2018)). These features were used to train six different classifiers. The maximum accuracy obtained using the signals of the 19 epileptic patients was $66.9 \pm 0.59\%$ using a random forest classifier.

There is only one other study in literature that proposes brain tissue classification using SEEG signals (see (Greene et al. 2021)). The authors proposed two features extracted from signals in bipolar montage. The accuracy obtained using the features proposed by (Greene et al. 2021) and an LDA classifier is $60 \pm 4\%$ for the 19 patients of this study, which is lower compared to the accuracy obtained with the features proposed here. However, the Bayesian classification method proposed by the authors in (Greene et al. 2021) could be more robust as it considers prior knowledge in brain tissue distribution.

The approach with better results for brain tissue classification is the one with features extracted from the non-parametric frequency response identification of pairs of consecutive contacts. In addition, the results show that the method is robust to epileptic tissues, and achieves the same accuracy for tissue classification with and without considering the epileptic networks. With this performance, the tissue classification method could be used to support brain tissue classification via the coregistration of CT scan (with implanted SEEG electrodes) with preoperative MRI, helping not only with signal interpretation, but also in the choice of contacts to be recorded.

Moreover, the posterior probabilities obtained with the LDA classifier for each pair could give an idea of the tissue composition between a pair of contacts. To achieve this, more studies need to be done with signals measured in distant white matter.

The fact that the non-parametric frequency response is a good discriminator between grey and white matter, makes it interesting to study the parametric model that characterises the brain-electrode interface. The parameters of the identified model could be used for tissue classification, and give a physical insight into the differences between brain tissues. This parametric approach will be discussed in the following chapter.

Chapter 4

# Brain tissue classification from the modelling of the brain-electrode interface

The differences in conductivity of grey and white matter have been largely studied in literature as shown in section 1.3. Hence, if one has access to the resistance value between two measuring contacts, it could be used as a metric for tissue classification. Moreover, from the results of chapter 3, where the features extracted from the non-parametric frequency response were the most discriminant between brain matters, the next step would be to perform a parametric system identification of the brain-electrode interface. In addition, an appropriate interface model helps with understanding the tissues response to stimulation which can also help with artefact correction (Trebaul, Rudrauf, et al. 2016).

Previous studies have proposed electronic circuit models based on the physical properties of the brain-electrode interface. In (Lempka, Miocinovic, et al. 2009), (Sankar et al. 2014) and (M. Johnson et al. 2005) models were proposed based on (McAdams and Jossinet 1995) to study the impedance measured by electrodes chronically implanted in brain of a monkey and rats respectively. All of these previously mentioned models contain a constant phase element that introduces a non-integer derivative to the system.

To our knowledge, the only study to measure the impedance of the brain-electrode interface using *in clinico* signals obtained from SEEG electrodes is (Carvallo et al. 2018). The authors propose a simpler impedance model with no non-integer derivatives which is identified from the measured potentials in pairs of adjacent electrode contacts stimulated by a known current in two epileptic patients. Even though the results of the mentioned study are promising for grey and white matter differentiation and brain-electrode interface modelling, it does not use signals from typical clinical settings of SEEG recording sessions, which makes it hard to reproduce. In other words, even though the authors use implanted SEEG electrodes, the stimulated and measured signals used for identification are not the ones typically recorded in SEEG exploration. Despite the fact that direct brain stimulation might be performed during SEEG investigation, the voltage in the stimulated contacts is not measured, therefore the proposed analysis by the authors requires more information than usually available.

In the present study a new method for the brain-electrode interface identification is proposed using only baseline voltage signals recorded during typical clinical settings of SEEG

before resective surgery. Prior to that, a study on the physical properties of the electrode-electrolyte interface is performed in data collected on a *phantom EEG* device designed in (Becq, Voda, et al. 2017), and previously studied in (Besancon et al. 2018) and (Besançon et al. 2019). The aim is to refine the models proposed in (Besancon et al. 2018) and (Besançon et al. 2019) by adding physical components described in the literature concerning EEG measurements. The use of *phantom EEG* devices enables to identify the components precisely, as one has control over stimulation signals and knowledge of the medium properties. This preliminary study gives a good idea on what values can be expected when modelling the brain-electrode interface.

## 4.1 Study of the electrode-electrolyte interface

In this section, the preliminary study on the modelling of the electrode-electrolyte interface using the *phantom EEG* device is presented. As mentioned, the device was proposed in (Becq, Voda, et al. 2017), and previously modelled in (Besancon et al. 2018) and (Besançon et al. 2019). Here, the goal is to retrieve the dynamical and physical properties of the electrode-electrolyte interface and the values of the components that form it, to have a starting point for the study of the brain-electrode interface. The results presented in this section were published in (M. Machado, Voda, Besançon, Becq, and David 2020).

### 4.1.1 *phantom EEG* setup

The experimental setup proposed in (Becq, Voda, et al. 2017) can be represented as in Fig. 4.1. The input signal is either a white noise or a sinusoid, generally used for electrochemical impedance spectroscopy. The signals are generated in Python and are transmitted to the input electrode via a digital to analog converter (National Instruments CRIO-9263 mounted on a cDAQ-9181 Ethernet chassis). The input electrode is inserted into an electrolyte medium which is a solution of phosphate buffered saline (PBS) obtained from a dissolution of half a tablet of P4417 Sigma-Aldrich in 1 $l$ of pure water (0.1 times concentration).

The output voltage is measured in three different positions by output electrodes located at 1 cm, 3 cm, and 5 cm from the input electrode. The input and output electrodes are connected to an EEG recorder (g.tec g.USBamp) with a selected sampling frequency of 4.8 kHz. The electrodes are made out of pure platinum and have a cylindrical shape with a 0.5 mm diameter and length of 1 cm. Only about 0.5 cm of the length of the electrodes are inserted into the medium.

### 4.1.2 Previous modelling of the *phantom EEG* measurement chain

The modelling of the *phantom EEG* measurement chain, was already addressed in previous works (Becq, Voda, et al. 2017), (Besancon et al. 2018), (Besançon et al. 2019). In all previous

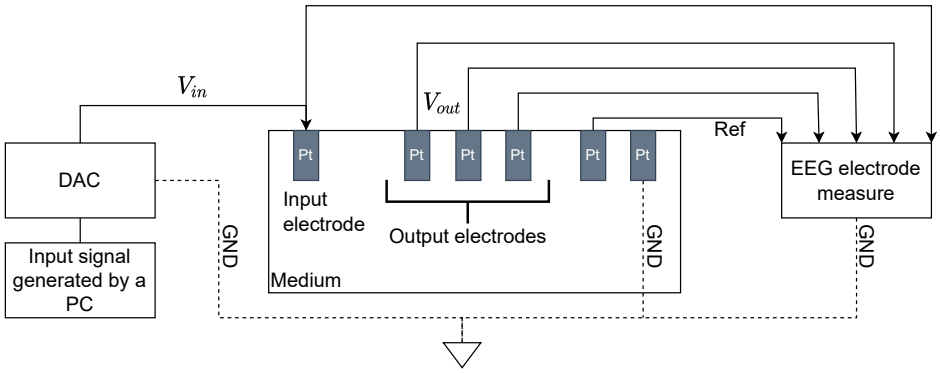


Figure 4.1: Experimental setup for data acquisition of the *phantom EEG*.

cases, the model was proposed based on the shape of the non-parametric frequency responses obtained from data, as described in section 2.2. Two cases were studied, at first the medium was composed by a sponge submerged in the electrolyte, in the second case the medium was purely formed by electrolyte. The proposed model for the medium composed by the sponge and electrolyte can be found in Fig. 4.2a. The model for electrolyte only mediums is shown in Fig. 4.2b.

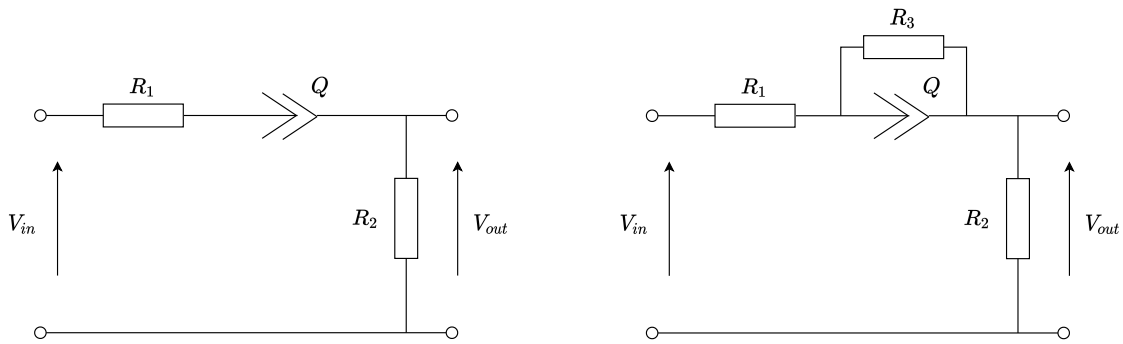


(a) First model (b) Refined model

Figure 4.2: Previous circuit models of the *phantom EEG* measurement chain proposed by (Becq, Voda, et al. 2017), (Besancon et al. 2018), and (Besançon et al. 2019). In (a) the first proposed model. In (b) the refined model considering purely electrolyte mediums.

As it was mentioned in section 1.4.1, for both models there is a CPE present of equation (1.1), which introduces a non-integer derivative to the resulting transfer function. The focus here is given to the second model of Fig. 4.2b, as the interest is to characterise a purely electrolyte medium. The transfer function can be obtained from the model considering a voltage divider, which gives:

$$H(s) = \frac{Y(s)}{U(s)} = \frac{B_0 + B_1 s^{\alpha}}{1 + A_1 s^{\alpha}} \tag{4.1}$$

with:

$$B_0 = \frac{R_2}{R_1 + R_2 + R_3} \tag{4.2}$$

$$B_1 = \frac{R_2 R_3 Q}{R_1 + R_2 + R_3} \tag{4.3}$$

$$A_1 = \frac{R_3(R_1 + R_2)Q}{R_1 + R_2 + R_3} \tag{4.4}$$

As there is a nonlinear relationship between the transfer function coefficients ($B_0$, $B_1$, and $A_1$) and the electronic components, the latter can not be retrieved directly from the identified coefficients, only the value of the ratio of resistances can be recovered:

$$\rho = \frac{B_1}{A_1} = \frac{R_2}{R_1 + R_2} \tag{4.5}$$

These first studies on the modelling of the *phantom EEG* measurement chain yield good fit to the data. The drawback lies mainly on the physical interpretation of the model, and the fact that the electronic circuit components cannot be directly retrieved from the transfer function parameters. This is why in the next sections, a model based on the physical properties of each stage in the *phantom EEG* measurement chain is proposed, and compared to the ones presented in this section. In other words, the aim is to go beyond the direct transfer function between input voltage $V_{in}$ and output voltage $V_{out}$, as it was established in (Becq, Voda, et al. 2017), (Besancon et al. 2018), and (Besançon et al. 2019), and find a model that describes separately the effects of input electrode, medium, output electrode and EEG recorder, as in Fig. 4.3.

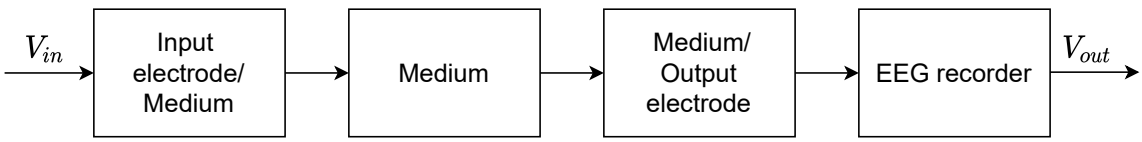


Figure 4.3: Block diagram of the different parts of the *phantom EEG* measurement chain.

### 4.1.3 Physical-based approach for the model structure

One of the first authors to propose an electronic circuit representation of the EEG measurement chain was (Robinson 1968), with a form recalled in Fig. 4.4. The difference between the model proposed by the author and the *phantom EEG* being analysed here is the input electrode that does not appear in (Robinson 1968). The signal is considered to be generated directly from neuronal activities. The author represents the solution by a resistance ($R_s$), the impedance of the output electrode by a metallic resistance ($R_m$) in series with the parallel of the shunt

capacitance of the system to the ground ($C_s$) and the input impedance of the amplifier of the recorder ($R_a$). Robinson also proposes a representation of the interface between the electrode and the electrolyte solution as the parallel between a double layer capacitance ($C_{dl}$) and a charge transfer resistance ($R_{CT}$).

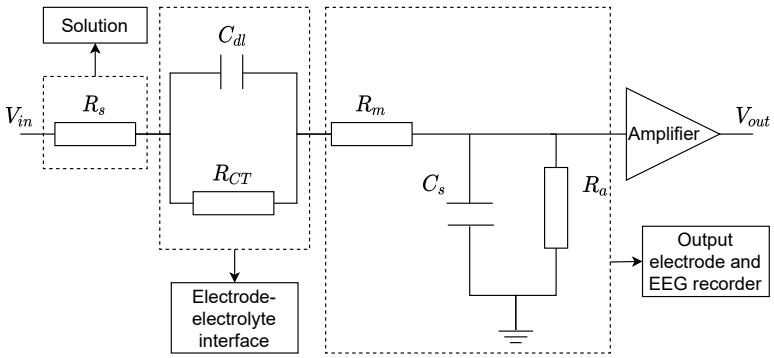


Figure 4.4: Model proposed in (Robinson 1968) for EEG measurement chain with input from neuronal activity.

Many authors have discussed fractional order representations of the electrode-electrolyte interface. For instance (Magin et al. 2008) studied the interface between cardiac tissue and electrodes and (McAdams, Lackermeier, et al. 1995) studied various different aspects of what happens when a metal is placed in an electrolyte. The most common circuit proposed for modelling the interface is shown in Fig. 4.5a.


(a) First model (b) Refined model

Figure 4.5: Commonly used models for the electrode/electrolyte interface. (a) General model. (b) Platinum electrode/electrolyte interface model.

The non-faradic processes in the interface are represented by the double layer capacitance $C_{dl}$ that corresponds to the layers of charge of opposite polarity located in the surface of the electrode and in the electrolyte. The faradic processes are represented by the charge transfer resistance $R_{CT}$ in series with the Warburg impedance $Z_W$. The resistance $R_{CT}$ represents the possible transfer of charge that occurs in the interface and $Z_W$ represents the diffusion, with a transfer function as follows (where $s$ stands for the Laplace variable):

$$Z_W = \frac{1}{C_w s^{0.5}} \tag{4.6}$$

For the specific case of this study where platinum electrodes were chosen, for potentials with absolute value under 0.5 V, the faradic processes are greatly reduced in the interface. (McAdams, Lackermeier, et al. 1995) proposed a new circuit to represent specifically the case of platinum electrodes in electrolyte medium (Fig. 4.5b). In this case, $Z_{CPE}$ is a constant phase element of equation (1.1), for $0 < \alpha < 1$ that represents the non-faradic processes in the interface instead of the capacitance $C_{dl}$. The choice to replace the double layer capacitance by a constant phase element was made because the latter better represents the adsorption and surface roughness effects. Even though the faradic processes are reduced, there might still be a charge transfer in very small amounts between the electrode and the electrolyte, as explained by (McAdams, Lackermeier, et al. 1995), that is why $R_{CT}$ is still present in the circuit.

With the preliminary study of the EEG measurement chain made by (Robinson 1968) and the interface proposed by (McAdams, Lackermeier, et al. 1995), the complete circuit that represens the *phantom EEG* setup under study is given in Fig. 4.6. $R_{med1}$, $Z_{CPE1}$, and $R_{CT1}$ represent the metallic resistance and the electrode-electrolyte interface for the input electrode, $R_s$ represents the resistance of the solution (electrolyte), $R_{med2}$, $Z_{CPE2}$, and $R_{CT2}$ represent the metallic resistance and the electrode-electrolyte interface for the output electrode, and $C_s$ represents the shunt capacitance to the ground. $R_r$ is a simplification of the impedance of the recorder viewed from the measurement chain considering that the signal is filtered and amplified.

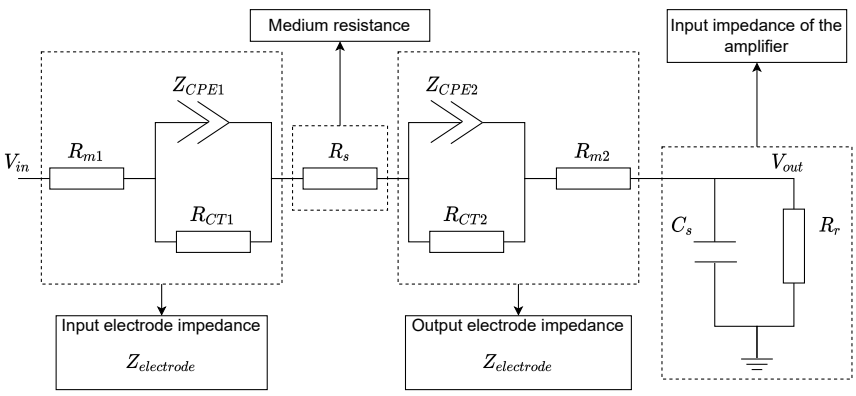


Figure 4.6: Proposed model of the *phantom EEG* measurement chain.

For the case studied here, the input and output electrodes will be considered to be the same in terms of their physical properties ($R_{m1} = R_{m2} = R_m$, $Z_{CPE1} = Z_{CPE2} = Z_{CPE}$, and $R_{CT1} = R_{CT2} = R_{CT}$). This consideration is made in order to simplify the model of the EEG measurement chain, as the identification of more complex models tend to be more sensitive to noise (as described in the results and discussion presented hereafter). This is not far from reality as both electrodes have the same dimensions, are made of the same material and they are in contact with the same electrolyte. With this assumption, and using equation (1.1) for

$Z_{CPE}$, the impedance of each electrode can be represented as follows:

$$Z_{electrode} = \frac{R_m R_{CT} Q s^{\alpha} + R_m + R_{CT}}{R_{CT} Q s^{\alpha} + 1} = \frac{p_1 s^{\alpha} + p_2}{x_1 s^{\alpha} + 1} \tag{4.7}$$

From equation (4.7), the transfer function that describes the model is:

$$H(s) = \frac{V_{out}}{V_{in}} = \frac{B_1 s^{\alpha} + B_2}{A_1 s^{\alpha+1} + A_2 s + A_3 s^{\alpha} + 1} \tag{4.8}$$

with:

$$B_1 = \frac{R_r x_1}{R_r + 2p_2 + R_s} \tag{4.9}$$

$$B_2 = \frac{R_r}{R_r + 2p_2 + R_s} \tag{4.10}$$

$$A_1 = \frac{2p_1 R_r C_s + R_s R_r C_s x_1}{R_r + 2p_2 + R_s} \tag{4.11}$$

$$A_2 = \frac{2p_2 R_r C_s + R_r C_s R_s}{R_r + 2p_2 + R_s} \tag{4.12}$$

$$A_3 = \frac{R_r x_1 + 2p_1 + x_1 R_s}{R_r + 2p_2 + R_s} \tag{4.13}$$

The aim now is to recover from the identification of transfer function (4.8), the six physical parameters of the circuit in Fig. 4.6 that are $R_m$, $R_{CT}$, $Z_{CPE}$, $R_s$, $C_s$, and $R_r$. The problem is that there are only five coefficients which are (structurally) identifiable (see (Walter et al. 1997)) from equations (4.9) to (4.13). Therefore, one of the six physical parameters has to be estimated via other considerations. The chosen physical parameter to be calculated is the medium resistance $R_s$, which can be calculated directly from the general resistance formula given in equation (4.14) hereafter, in which $\sigma\,([S/cm])$ is the electrical conductivity of the solution, $l\,([cm])$ the length of the material for which the resistance is going to be measured and $A\,([cm^2])$ the transverse surface of the material:

$$R = \frac{1}{\sigma}\frac{l}{A} \tag{4.14}$$

In the case of the resistance of the solution, the length ($l$) is the distance between the input and output electrodes. The area ($A$) is the transverse surface of electrolyte between the input and output electrodes, which can be approximated to the lateral surface of the cylinder of diameter 0.5 mm and height 0.5 cm. The electrical conductivity ($\sigma$) of the PBS presented in section 2 was already estimated in (A. Johnson et al. 2004) as being $\sigma = 0.00181$ $[S/cm]$. The resulting values of the resistance of the solution as a function of distance are given in

| Distance between electrodes | $R_s$ |
|---|---|
| 1 cm | 7.03 kΩ |
| 3 cm | 21.10 kΩ |
| 5 cm | 35.17 kΩ |

Table 4.1: Values of $R_s$ as a function of the distance between electrodes.

Table 4.1. The found values of $R_s$ are close in order to those calculated in (Robinson 1968) and (A. Johnson et al. 2004).

With the resistance of the solution ($R_s$) known, the system of equations to recover the physical parameters of the circuit shown in Fig. 4.6 is given by equation (4.15).

$$\begin{cases} x_1 = \frac{B_1}{B_2} \\ R_r(B_2 - 1) + 2p_2 B_2 = -R_s B_2 \\ 2p_1 - \frac{A_1}{B_2}\frac{1}{C_s} = -R_s \frac{B_1}{B_2} \\ \frac{A_2}{B_2}\frac{1}{C_s} - 2p_2 = R_s \\ R_r\left(\frac{B_1}{B_2} - A_3\right) + 2p_1 - 2p_2 A_3 = R_s\left(A_3 - \frac{B_1}{B_2}\right) \end{cases} \tag{4.15}$$

### 4.1.4 Identification methodology

The transfer function of the model to be identified is given in equation (4.1). As for the noise structure, the system is considered to be of the ARX form (see section 2.3). For such model, the parameters can be directly estimated considering the input and output signals using the least squares algorithm, since the relationship between the cost function and the parameters is linear (see equation (2.33)). However, the choice is made to use the recursive version of the previously mentioned algorithm, the recursive least squares (RLS) with the adaptation gain version presented in (Landau et al. 2006). The ARX model is chosen because the RLS algorithm is easily implemented when compared to others.

The system to be identified has a non-integer order. Therefore, there are fractional order derivatives that need to be approximated in order to guarantee the precision of the identification. There are many ways in which one can approximate the non-integer order derivative, most of them are presented in section 2.6. Here, the selected approximation method was proposed by Ivo Petràš in (Petrás 2011) for its small computational time and good precision. The *Matlab* algorithm *dfod1* proposed in (Petráš 2003) is used. As an input, the function takes the order of the equivalent transfer function to be found ($n = 4$) and the weighting factor for the Al-Alaoui rule ($a = 1/7$). This values were chosen via trial and error by comparison of the responses of the identified models. Thus the non-integer derivative is approximated as:

$$s^{\beta_j} \approx \frac{\sum_{i=0}^{n} c_{j,i} z^{-i}}{\sum_{i=0}^{n} d_{j,i} z^{-i}} \tag{4.16}$$

with $j = [1, 2]$, $\beta_1 = \alpha + 1$, $\beta_2 = \alpha$, $c$ and $d$ the numerator and denominator coefficients respectively given by *dfod1*. The integer order derivatives are discretized using the Tustin discretization method presented in equation (2.6).

Considering the general output of an ARX model given as:

$$\hat{y}(k+1) = \hat{\theta}^T \varphi(k) \tag{4.17}$$

with the regression vector $\hat{\theta}^T$ written as follows:

$$\hat{\theta}^T = [\hat{b}_1,\, \hat{b}_2,\, \hat{a}_1,\, \hat{a}_2,\, \hat{a}_3] \tag{4.18}$$

with:

$$\hat{b}_1 = \frac{\hat{B}_1 d_{1,0} d_{2,0} T}{T d_{1,0} d_{2,0} + \hat{A}_1 c_{1,0} d_{2,0} T + \hat{A}_2 2 d_{1,0} d_{2,0} + \hat{A}_3 T c_{2,0} d_{1,0}} \tag{4.19}$$

$$\hat{b}_2 = \frac{\hat{B}_2 d_{1,0} d_{2,0} T}{T d_{1,0} d_{2,0} + \hat{A}_1 c_{1,0} d_{2,0} T + \hat{A}_2 2 d_{1,0} d_{2,0} + \hat{A}_3 T c_{2,0} d_{1,0}} \tag{4.20}$$

$$\hat{a}_1 = \frac{\hat{A}_1 d_{1,0} d_{2,0} T}{T d_{1,0} d_{2,0} + \hat{A}_1 c_{1,0} d_{2,0} T + \hat{A}_2 2 d_{1,0} d_{2,0} + \hat{A}_3 T c_{2,0} d_{1,0}} \tag{4.21}$$

$$\hat{a}_2 = \frac{\hat{A}_2 d_{1,0} d_{2,0} T}{T d_{1,0} d_{2,0} + \hat{A}_1 c_{1,0} d_{2,0} T + \hat{A}_2 2 d_{1,0} d_{2,0} + \hat{A}_3 T c_{2,0} d_{1,0}} \tag{4.22}$$

$$\hat{a}_3 = \frac{\hat{A}_3 d_{1,0} d_{2,0} T}{T d_{1,0} d_{2,0} + \hat{A}_1 c_{1,0} d_{2,0} T + \hat{A}_2 2 d_{1,0} d_{2,0} + \hat{A}_3 T c_{2,0} d_{1,0}} \tag{4.23}$$

considering $\hat{B}_1$, $\hat{B}_2$, $\hat{A}_1$, $\hat{A}_2$, and $\hat{A}_3$ as the estimations of the transfer function coefficients, and $\varphi(k)$ the regression vector given as:

$$\varphi(k) = [U_1(k), U_2(k), -Y_1(k), -Y_2(k), -Y_3(k)] \tag{4.24}$$

with:

$$U_1(k) = \frac{1}{d_{2,0}} \left[ \sum_{i=0}^{n} c_{2,i} V_{in}(k-i) - \sum_{i=1}^{n} d_{2,i} U_1(k-i) \right] \tag{4.25}$$

$$U_2(k) = V_{in}(k) \tag{4.26}$$

$$Y_1(k) = \frac{1}{d_{1,0}} \left[ \sum_{i=0}^{n} c_{1,i} V_{out}(k-i) - \sum_{i=1}^{n} d_{1,i} Y_1(k-i) \right] \tag{4.27}$$

$$Y_2(k) = -\frac{2}{T} V_{out}(k-1) - Y_2(k-1) \tag{4.28}$$

$$Y_3(k) = \frac{1}{d_{2,0}} \left[ \sum_{i=0}^{n} c_{2,i} V_{out}(k-i) - \sum_{i=1}^{n} d_{2,i} Y_3(k-i) \right] \tag{4.29}$$

As mentioned, the choice is made to use the RLS algorithm (presented in section 2.3) to identify $\hat{\theta}$. As a reminder, it consists of the system (4.30), with $\lambda$ representing the forgetting factor, meaning the given importance for past values in the current time estimation. In this application, it is chosen as $\lambda = 0.99$ as it resulted in identified coefficients less sensitive to noise.

$$\begin{cases} \hat{\theta}(k+1) = \hat{\theta}(k) + F(k)\varphi(k)\epsilon(k+1) \\ F(k+1) = \frac{1}{\lambda}[F(k) - \frac{F(k)\varphi(k)\varphi^T(k)F(k)}{\lambda+\varphi^T(k)F(k)\varphi(k)}] \\ \epsilon(k+1) = \frac{y(k+1)-\hat{\theta}^T(k)\varphi(k)}{1+\varphi^T(k)F(k)\varphi(k)} \end{cases} \tag{4.30}$$

Here, $F(k)$ is initialised as $F = gI$, where $I$ represents the identity matrix, and $g = 10^5$ (see (Landau et al. 2006)).

In order to determine if an identified model is not biased, a validation test must be performed. The recursive least squares method is based on the whitening of the prediction error (see section 2.5). Therefore, in order to validate the identified model, whiteness and cross-correlation tests must be performed (see equations (2.85) and (2.86)). Once the values of $\hat{\theta}$ are identified and the model is validated, one can retrieve the transfer function coefficients using the following equations:

$$\hat{B}_1 = \frac{-\hat{b}_1 T d_{1,0} d_{2,0}}{2\hat{a}_2 d_{1,0} d_{2,0} - T d_{1,0} d_{2,0} + \hat{a}_1 T c_{1,0} d_{2,0} + \hat{a}_3 T c_{2,0} d_{1,0}} \tag{4.31}$$

$$\hat{B}_2 = \frac{-\hat{b}_2 T d_{1,0} d_{2,0}}{2\hat{a}_2 d_{1,0} d_{2,0} - T d_{1,0} d_{2,0} + \hat{a}_1 T c_{1,0} d_{2,0} + \hat{a}_3 T c_{2,0} d_{1,0}} \tag{4.32}$$

$$\hat{A}_1 = \frac{-\hat{a}_1 T d_{1,0} d_{2,0}}{2\hat{a}_2 d_{1,0} d_{2,0} - T d_{1,0} d_{2,0} + \hat{a}_1 T c_{1,0} d_{2,0} + \hat{a}_3 T c_{2,0} d_{1,0}} \tag{4.33}$$

$$\hat{A}_2 = \frac{-\hat{a}_2 T d_{1,0} d_{2,0}}{2\hat{a}_2 d_{1,0} d_{2,0} - T d_{1,0} d_{2,0} + \hat{a}_1 T c_{1,0} d_{2,0} + \hat{a}_3 T c_{2,0} d_{1,0}} \tag{4.34}$$

$$\hat{A}_3 = \frac{-\hat{a}_3 T d_{1,0} d_{2,0}}{2\hat{a}_2 d_{1,0} d_{2,0} - T d_{1,0} d_{2,0} + \hat{a}_1 T c_{1,0} d_{2,0} + \hat{a}_3 T c_{2,0} d_{1,0}} \tag{4.35}$$

The overall identification algorithm can be summarised by the following flowchart given in Fig. 4.7.

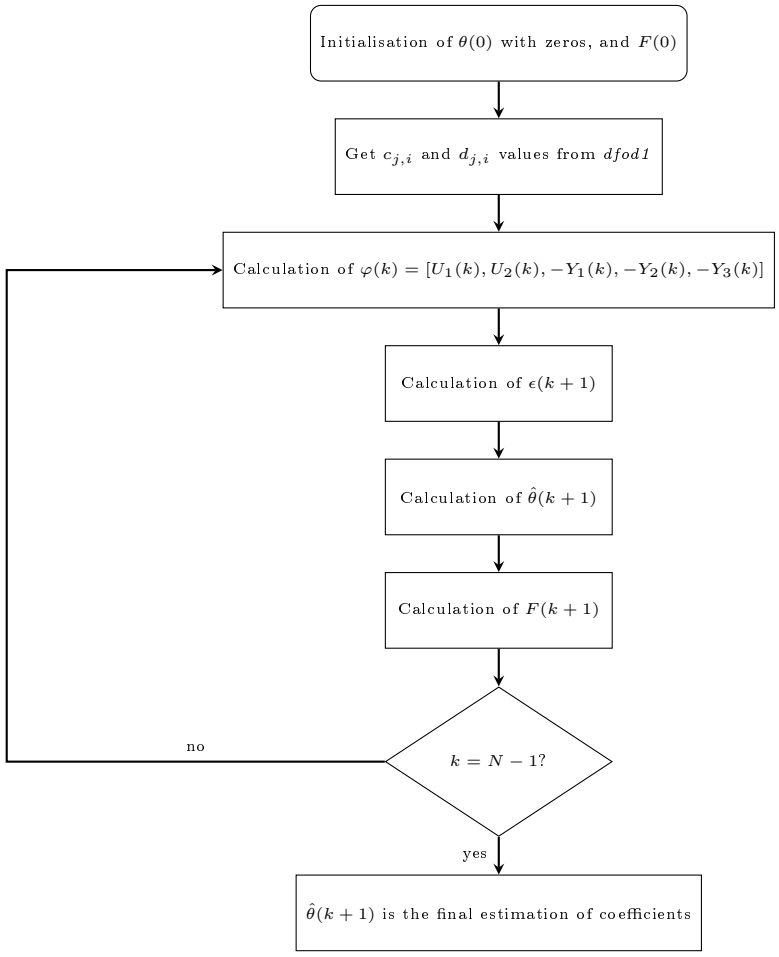


Figure 4.7: Flowchart representing the identification algorithm of the *phantom EEG*.

### 4.1.5 Identification of non-integer order $\alpha$

In the identification methodology presented in the previous subsection, a constant non-integer order is assumed. In order to determine this value, a system is identified for various different fixed non-integer orders in the interval $0 < \alpha < 1$. The chosen order is the one corresponding to the best identified system. The main criterion considered here for the comparison between identified systems is the best fitted Nyquist plot (when comparing model to data). An example of Nyquist plots for a small interval of $\alpha$ values is given in Fig. 4.8 considering the distance of 1cm between electrodes.

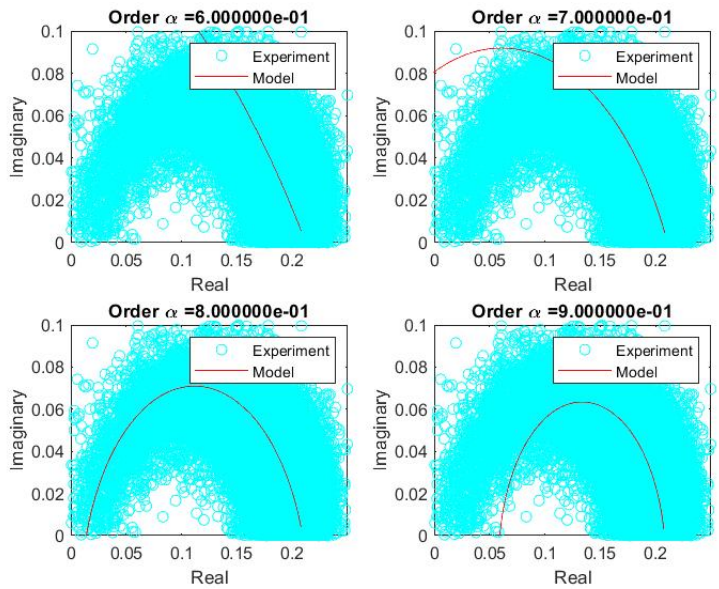


Figure 4.8: Comparison between Nyquist plots for order selection ($\alpha$).

This criterion is chosen for the fact that the Nyquist plots analysis is subject to the largest variations under order changes, in comparison to time responses and Bode plots. The selected non-integer order is $\alpha = 0.8$. The same test was repeated considering the other distances and $\alpha = 0.8$ was selected as the optimal order for all of the cases.

### 4.1.6 Identification results

After the selection of the non-integer order, the identification methodology presented in subsection 4.1.4 is applied considering the signals measured at the three different positions. The identified transfer function coefficients can be found in Table 4.2.

The values of $\hat{A}_1$ are negative for all of the distance cases, which is not expected as the coefficients describe electronic components. However, since the value of $\hat{A}_1$ is really small when compared to $\hat{B}_1$, $\hat{B}_2$ and $\hat{A}_3$, it can be considered to be zero. With that, the system of

| | 1cm | 3cm | 5cm |
|---|---|---|---|
| $\hat{B}_1$ | 1.0160e-03 | 5.3042e-04 | 3.7735e-04 |
| $\hat{B}_2$ | 1.4043e-02 | 5.3900e-02 | 7.4789e-02 |
| $\hat{A}_1$ | -5.4077e-08 | -8.1570e-08 | -2.0437e-07 |
| $\hat{A}_2$ | 7.3782e-09 | 9.1186e-09 | 1.1944e-08 |
| $\hat{A}_3$ | 4.8536e-03 | 4.9977e-03 | 7.1832e-03 |

Table 4.2: Identified coefficients with RLS method for each of the different distances.

equations given in (4.15) can be used to recover the physical parameters when $R_s$ is considered known with values in Table 4.1. However, the condition number of the matrix containing the weights of each variable is too high (1.9586e+09), which means that small variations in the results can imply big variations in the identified coefficients. In other words, the system is ill-conditioned and is not trustworthy to recover the physical parameters. This was also observed in simulation. As a remedy, a simplification of the model given by equation (4.8) can be considered. What can be seen from the obtained coefficients shown in table 4.2 indeed, is that not only $\hat{A}_1$ can be approximated as zero, but also $\hat{A}_2$. With these remarks, the transfer function can be rewritten as:

$$H(s) = \frac{B_1 s^\alpha + B_2}{A s^\alpha + 1} \tag{4.36}$$

Notice that the number of equations in the system is reduced, but $C_s$ is no longer a variable to be identified, and, with $R_s$ known there are only four physical parameters to be identified: $R_m$, $R_{CT}$, $Z_{CPE}$ (that are combined to form $p_1$, $p_2$ and $x_1$), and $R_r$. Even with a reduced number of parameters there is still one more physical parameter than there are equations, therefore $R_m$ has to be calculated. The calculation can indeed be done in the same way as that of $R_s$ using equation (4.14). In this case $\sigma$ is the electrical conductivity of platinum that can be found in (Cantrell et al. 2007), $l$ is the length of the electrode (1 cm) and $A$ can be approximated as the transverse surface of the electrode assuming that the current flows uniformly inside it. With that, the value of the metallic resistance of the electrode is given by:

$$R_m = \frac{1}{9.4 \times 10^6} \frac{0.01}{\pi (2.5 \times 10^{-4})^2} = 0.0054 \ [\Omega] \tag{4.37}$$

The value of $R_m$ is very small when compared to the other resistances, so it does not have an impact in the final physical values. The problem is that $R_m$ is not written explicitly in the system of equations (4.15). But there is a way of expressing $R_r$ as a function of $R_s$ and $R_m$. This can be achieved by dividing the coefficient $B_1$ of equation (4.9) by the coefficient $A_3$ of equation (4.12), and by writing $p_1$ and $x_1$ as functions of the electronic components. The system of equations (4.15) can be rewritten as (4.38):

$$\begin{cases} R_r = \frac{(\frac{B_1}{A})2R_m + (\frac{B_1}{A})R_s}{1-\frac{B_1}{A}} \\ x_1 = \frac{B_1}{B_2} \\ 2p_2B_2 = -R_sB_2 - R_r(B_2 - 1) \\ 2p_1 - 2p_2a = R_s\left(A - \frac{B_1}{B_2}\right) - R_r\left(\frac{B_1}{B_2} - A\right) \end{cases} \tag{4.38}$$

As the data for 3 cm and 5 cm of distance were found to have important noise, a new identification is done, considering only three parameters for these two cases, resulting in identified coefficients less sensitive to noise. The final coefficients identified for each of the cases are given in table 4.3. The coefficients were found not to be biased as they were validated by the whiteness and cross-correlation tests.

| | 1cm | 3cm | 5cm |
|---|---|---|---|
| $\hat{B}_1$ | 1.0160e-03 | 4.4200e-04 | 2.7536e-04 |
| $\hat{B}_2$ | 1.4043e-02 | 1.2687e-02 | 5.7549e-03 |
| $\hat{A}$ | 4.8536e-03 | 3.3536e-03 | 3.4787e-03 |

Table 4.3: Identified coefficients with RLS method for each of the different distances.

From these identified coefficients, equation (4.14), and the solution of (4.38), the physical parameters can be recovered directly from the following system of equations, with $l$ being the distance between input and output electrodes:

$$\begin{cases} R_s = (2.2099 \times 10^4)\, l \\ R_m = 0.0054 \\ R_r = \frac{(\frac{B_1}{A})2R_m + (\frac{B_1}{A})R_s}{1-\frac{B_1}{A}} \\ R_{CT} = p_2 - R_m \\ Q = \frac{x_1}{R_{CT}} \end{cases} \tag{4.39}$$

The solution of (4.39) gives the physical parameters summarized in table 4.4. The recovery of the physical parameters gives an idea of the order of magnitude of the electronic components that can be expected when it comes to the electrode-electrolyte interface. It can be seen that not only the values of $R_s$ change with the distance between input and output electrodes, but also $R_{CT}$, and $Q$ values depend on the separation of electrodes. The values of $R_r$ are not that affected by the distance between electrodes. However, its values are considerably small when compared to the expected input impedance of an amplifier ($\sim$ 1M$\Omega$). This could be justified from the fact that the reference electrode is situated in the saline solution, thus the input impedance of the amplifier is in parallel with the resistance between the output electrode and the reference electrode. As the resistance between electrodes on the saline solution is smaller than the input impedance, the resulting resistance is dominated by the smaller one. This is why the values of $R_r$ are close in magnitude to $R_s$.

| | 1cm | 3cm | 5cm |
|---|---|---|---|
| $R_s$ $[k\Omega]$ | 7.03 | 21.10 | 35.17 |
| $R_m$ $[\Omega]$ | 0.0054 | 0.0054 | 0.0054 |
| $R_{CT}$ $[k\Omega]$ | 61.86 | 114.10 | 243.58 |
| $Q$ $[Fs^{-1+\alpha}]$ | 1.17e-06 | 3.0534e-07 | 1.96e-07 |
| $R_r$ $[k\Omega]$ | 1.86 | 3.20 | 3.02 |

Table 4.4: Physical parameters recovered from the results of the black box identification.

As it was mentioned, the identified models were validated by the whiteness and cross-correlation tests. As a second validation method it can be seen in Fig. 4.9 that the Nyquist plots generated from the identified models fit well with the Nyquist plots obtained from the ETFE of the data for every considered distance between input and output electrodes.

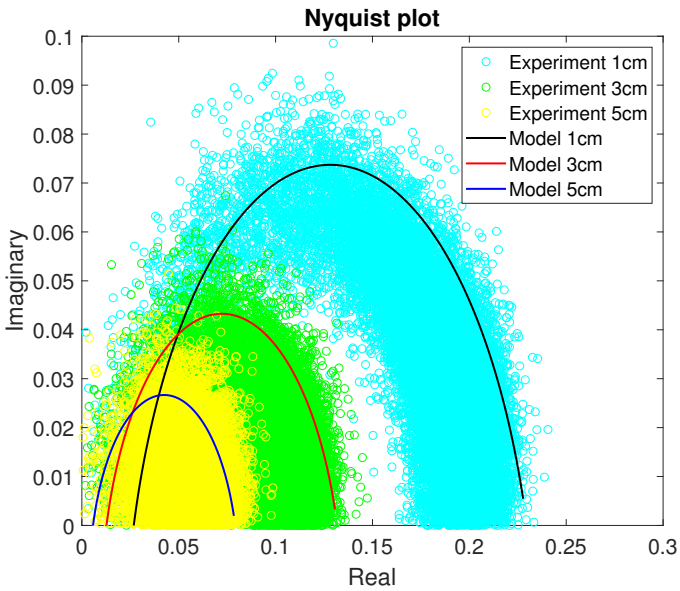


Figure 4.9: Nyquist plots for all of the three distances between input and output electrodes. The continuous lines represent the Nyquist plots obtained from the identified models, and the points represent the Nyquist plots obtained from the ETFE of the data.

## 4.2 Brain-electrode interface

In this section, the brain-electrode interface is modelled using the data from the 19 epileptic patients previously presented in section 3.1. A review of the state of the art on the proposed models of the brain-electrode interface was done in section 1.4. These previous models consist in three distinct parts: The electrode-electrolyte interface, the peri-electrode region, and the medium resistance. The model proposed in the previous section for the *phantom EEG* device,

can be used as a starting point for the modelling of the brain-electrode interface. The only part that is missing is the peri-electrode region.

As mentioned, even though the brain-electrode interface has been previously identified in literature for deep brain stimulation, to our knowledge, only one study (Carvallo et al. 2018) up to now has succeeded in measuring the impedance and fitting a model to *in clinico* signals obtained from SEEG electrodes in two epileptic patients. The proposed model in (Carvallo et al. 2018) had no non-integer derivatives, and was identified from the measured potentials in pairs of adjacent contacts stimulated by a known current. The values of medium resistance retrieved were dependent on the type of tissue the contacts were inserted in, which is promising for grey and white matter differentiation. However, the brain-electrode interface modelling proposed in (Carvallo et al. 2018) does not use signals from typical clinical settings of SEEG recording sessions, which makes it hard to reproduce. Thus, in the present study, a new method for the brain-electrode interface identification is proposed using only baseline signals recorded during typical clinical settings of SEEG. The aim is to use the information retrieved from the identified models to characterise different brain tissues.

### 4.2.1 Modelling

In the case of this study, the brain-electrode interface between two consecutive contacts is considered. In this context, the electrode-electrolyte interface and the peri-electrode layer should be considered twice. In (Carvallo et al. 2018), when comparing the values of the electrode-electrolyte electronic components obtained for grey and white matter, there does not seem to be a lot of differences. This is why, for simplification, $Q_{int}$, and $R_{ct}$ are considered as constant for all contacts. For the peri-electrode region, previous studies (Sankar et al. 2014; M. Johnson et al. 2005; Lempka, Miocinovic, et al. 2009) have not differentiated the values of components according to the tissue type. Therefore, the values of $R_{cl}$, $Q_{cl}$, and $R_{en}$ are also considered to be constant. In the literature (M. Johnson et al. 2005), (Lempka, Miocinovic, et al. 2009), the brain-electrode model is usually fitted to the impedance measured via electrochemical impedance spectroscopy (EIS) where both the current and voltages of two contacts are known. Here, the only information available reduces to the voltages measured during the SEEG procedure. Thus, a more complete circuit compared to the ones in literature needs to be proposed considering a voltage divider.

As mentioned, all voltages are measured with respect to a contact located in distant white matter (contact in a different electrode). However, if the voltages of two consecutive contacts are re-referenced with respect to the next adjacent contact after the second one, the circuit between the second contact and the third one is similar to the circuit between the first and second contacts. Therefore, the resulting model that will be identified in this study is given in Fig. 4.10.

The voltage measured by the first contact in regard to the third contact is considered to be the input voltage ($V_1$), and the one measured by the second contact in regard to the third contact is considered as the output voltage ($V_2$). As the distance between the first and the

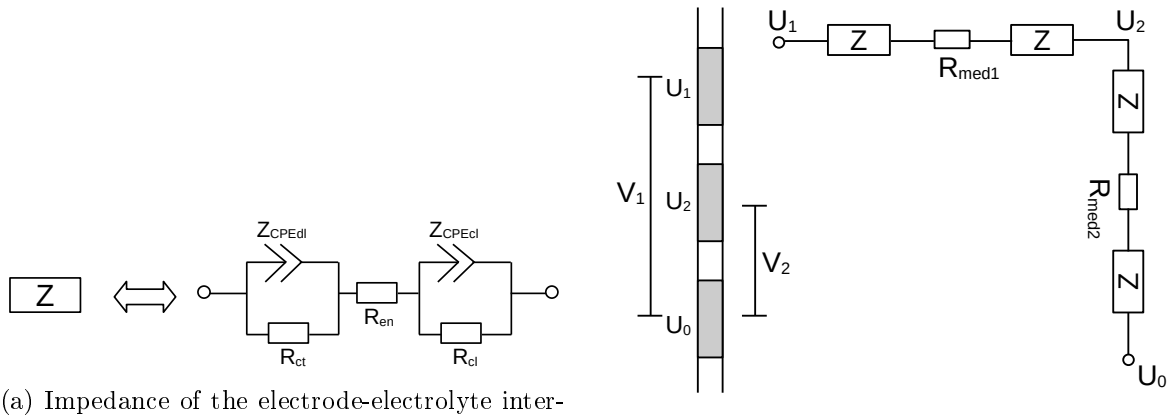


(a) Impedance of the electrode-electrolyte interface and peri-electrode region

(b) Brain-electrode interface model

Figure 4.10: Circuit that represents the appropriate brain-electrode interface model for SEEG signals to be identified using voltages $V_1$ and $V_2$ considering three consecutive electrodes. In (a) the electrode-electrolyte interface as well as the peri-electrode region are represented as an impedance $Z$. In (b) the complete model of the brain-electrode interface is shown in respect to the measured voltages.

second contacts is the same as the distance between the second contact and the reference, the order of magnitude of the electronic components between $U_1$ and $U_2$ is the same as the ones between $U_2$ and $U_0$.

In order to reduce the complexity of the model, the non-integer orders of both constant phase elements are considered to be the same and equal to $\alpha$, which is what is observed in (Lempka, Miocinovic, et al. 2009) some days after electrode insertion. The transfer function $H$ of the model can be easily found considering it as a voltage divider:

$$H(s) = \frac{V_{LT2}(s)}{V_{LT1}(s)} = \frac{B_1 s^{2\alpha} + B_2 s^{\alpha} + B_3}{A_1 s^{2\alpha} + A_2 s^{\alpha} + 1} \tag{4.40}$$

with $V_{LT1}(s)$ and $V_{LT2}(s)$ the Laplace transforms of $V_1$ and $V_2$.

The coefficients $[B_1, B_2, B_3, A_1, A_2]$ of the transfer function are expressed as a function of the electronic components as follows:

$$B_1 = \frac{Q_{int}Q_{cl}R_{ct}R_{cl}(R_{med2} + 2R_{en})}{4R_{ct} + 4R_{cl} + 4R_{en} + R_{med1} + R_{med2}} \tag{4.41}$$

$$B_2 = \frac{(Q_{int}R_{ct} + Q_{cl}R_{cl})(2R_{en} + R_{med2}) + 2R_{ct}R_{cl}(Q_{cl} + Q_{int})}{4R_{ct} + 4R_{cl} + 4R_{en} + R_{med1} + R_{med2}} \tag{4.42}$$

$$B_3 = \frac{2R_{ct} + 2R_{cl} + 2R_{en} + R_{med2}}{4R_{ct} + 4R_{cl} + 4R_{en} + R_{med1} + R_{med2}} \tag{4.43}$$

$$A_1 = \frac{Q_{int}Q_{cl}R_{ct}R_{cl}(4R_{en} + R_{med1} + R_{med2})}{4R_{ct} + 4R_{cl} + 4R_{en} + R_{med1} + R_{med2}} \tag{4.44}$$

$$A_2 = \frac{4R_{ct}R_{cl}(Q_{int} + Q_{cl}) + (4R_{en} + R_{med1} + R_{med2})(R_{ct}Q_{int} + R_{cl}Q_{cl})}{4R_{ct} + 4R_{cl} + 4R_{en} + R_{med1} + R_{med2}} \tag{4.45}$$

The relationship between the transfer function coefficients and the electronic circuit components is non-linear. Moreover, there are 5 identifiable transfer function coefficients and 7 component values to be retrieved. Thus, it is not possible to recover $Q_{int}$, $Q_{cl}$, $R_{int}$, $R_{cl}$, $R_{en}$, $R_{med1}$, and $R_{med2}$ directly. From the identified coefficients, it is possible nonetheless to get an idea of the difference in the resistances $R_{med1}$ and $R_{med2}$ in regards to the tissue type. For that, the transfer function coefficients can be rearranged in the following manners:

$$\left(\frac{B_1}{A_1}\right) = \frac{2R_{en} + R_{med2}}{4R_{en} + R_{med1} + R_{med2}} \tag{4.46}$$

$$\left(\frac{B_2}{A_2}\right) = \frac{c_1(2R_{en} + R_{med2}) + c_2}{(4R_{en} + R_{med1} + R_{med2})c_1 + 2c_2} \tag{4.47}$$

$$B_3 = \frac{2R_{ct} + 2R_{cl} + 2R_{en} + R_{med2}}{4R_{ct} + 4R_{cl} + 4R_{en} + R_{med1} + R_{med2}} \tag{4.48}$$

with: $c_1 = Q_{int}R_{ct} + Q_{cl}R_{cl}$, and $c_2 = 2R_{ct}R_{cl}(Q_{cl} + Q_{int})$.

For all cases, if $R_{med1} = R_{med2}$ then $(B_1/A_1) = 0.5$, if $R_{med1} < R_{med2}$ then $(B_1/A_1) > 0.5$, and if $R_{med1} > R_{med2}$ then $(B_1/A_1) < 0.5$.

As for the *phantom EEG* case, the noise model here is considered to be an ARX. This choice was made for the fact that an ARX model does not need to be identified using recursive algorithms that can take a long time to run considering the size of the data (see section 2.3).

### 4.2.2 Linear regression

As the available data are time series, the model needs to be re-written. Based on (Liang et al. 2015), the following equation can be written:

$$A_1\left(\frac{d}{dt}\right)^{2\alpha}V_2(t)+A_2\left(\frac{d}{dt}\right)^{\alpha}V_2(t)+V_2(t)= \\ B_1\left(\frac{d}{dt}\right)^{2\alpha}V_1(t)+B_2\left(\frac{d}{dt}\right)^{\alpha}V_1(t)+B_3V_1(t) \quad (4.49)$$

The approximation of the non-integer order derivative used here is the one proposed by Grünwald–Letnikov (Grunwald 1867), (Letnikov 1868) as it was previously used in other studies such as (Besançon et al. 2019). This approximation was chosen instead of the one used in the *phantom EEG* because it can be used in non-recursive manner, reducing the computation time. Considering a discrete signal $V$, with $N+1$ samples and the sampling time $h$, the fractional derivative of order $\alpha$ of the signal is given by equation (2.95), and is re-stated here:

$$\left(\frac{d}{dt}\right)^{\alpha}V(k)\simeq\frac{1}{h^{\alpha}}\sum_{i=0}^{N}(-1)^i\binom{\alpha}{i}V(k-i) \quad (4.50)$$

With this approximation, the output of the model at a discrete time k ($\hat{V}_2(k)$) is written as:

$$\hat{V}_2(k)=\hat{\theta}\varphi \quad (4.51)$$

with $\hat{\theta}$:

$$\hat{\theta}=[\hat{b}_1,\hat{b}_2,\hat{b}_3,\hat{a}_1,\hat{a}_2] \quad (4.52)$$

that represents the vector of regression coefficients, as function of the estimated transfer function coefficients $[\hat{B}_1,\hat{B}_2,\hat{B}_3,\hat{A}_1,\hat{A}_2]$:

$$\hat{b}_1=\frac{\hat{B}_1h^{2\alpha}}{h^{2\alpha}+\hat{A}_1+\hat{A}_2h^{\alpha}} \quad (4.53)$$

$$\hat{b}_2=\frac{\hat{B}_2h^{2\alpha}}{h^{2\alpha}+\hat{A}_1+\hat{A}_2h^{\alpha}} \quad (4.54)$$

$$\hat{b}_3=\frac{\hat{B}_3h^{2\alpha}}{h^{2\alpha}+\hat{A}_1+\hat{A}_2h^{\alpha}} \quad (4.55)$$

$$\hat{a}_1=\frac{\hat{A}_1h^{2\alpha}}{h^{2\alpha}+\hat{A}_1+\hat{A}_2h^{\alpha}} \quad (4.56)$$

$$\hat{a}_2=\frac{\hat{A}_2h^{2\alpha}}{h^{2\alpha}+\hat{A}_1+\hat{A}_2h^{\alpha}} \quad (4.57)$$

and $\varphi$:

$$\varphi = [V_{11}(k), V_{12}(k), V_{13}(k), -V_{21}(k), -V_{22}(k)]^T \tag{4.58}$$

that represents a matrix containing the modified data vectors given by:

$$V_{11}(k) = \frac{1}{h^{2\alpha}} \sum_{i=0}^{k} (-1)^i \binom{2\alpha}{i} V_1(k-i) \tag{4.59}$$

$$V_{12}(k) = \frac{1}{h^{\alpha}} \sum_{i=0}^{k} (-1)^i \binom{\alpha}{i} V_1(k-i) \tag{4.60}$$

$$V_{13}(k) = V_1(k) \tag{4.61}$$

$$V_{21}(k) = \frac{1}{h^{2\alpha}} \sum_{i=1}^{k} (-1)^i \binom{2\alpha}{i} V_2(k-i) \tag{4.62}$$

$$V_{22}(k) = \frac{1}{h^{\alpha}} \sum_{i=1}^{k} (-1)^i \binom{\alpha}{i} V_2(k-i) \tag{4.63}$$

where the creation of the data vectors is done based on (Jonathan 2022).

Equation (4.51) highlights the linear relationship between the output of the model $\hat{V}_2$ and the regression coefficients $\hat{\theta}$, which make them easy to identify. The transfer function coefficients $(\hat{B}_1, \hat{B}_2, \hat{B}_3, \hat{A}_1, \hat{A}_2)$ can be easily retrieved from the regression ones with the following equations:

$$\hat{B}_1 = \frac{-\hat{b}_1 h^{2\alpha}}{\hat{a}_1 + h^{\alpha}\hat{a}_2 - h^{2\alpha}} \tag{4.64}$$

$$\hat{B}_2 = \frac{-\hat{b}_2 h^{2\alpha}}{\hat{a}_1 + h^{\alpha}\hat{a}_2 - h^{2\alpha}} \tag{4.65}$$

$$\hat{B}_3 = \frac{-\hat{b}_3 h^{2\alpha}}{\hat{a}_1 + h^{\alpha}\hat{a}_2 - h^{2\alpha}} \tag{4.66}$$

$$\hat{A}_1 = \frac{-\hat{a}_1 h^{2\alpha}}{\hat{a}_1 + h^{\alpha}\hat{a}_2 - h^{2\alpha}} \tag{4.67}$$

$$\hat{A}_2 = \frac{-\hat{a}_2 h^{2\alpha}}{\hat{a}_1 + h^{\alpha}\hat{a}_2 - h^{2\alpha}} \tag{4.68}$$

### 4.2.3 Data pre-processing

As previously stated, the data used here was recorded in SEEG investigations of 19 epileptic patients. The data were sampled at either 1024 Hz (for 7 patients) or 512 Hz (for 12 pa-

tients) and was filtered by an acquisition band-pass filter between 0.1 and 200 Hz to eliminate noise. With the filtering of high frequencies, the useful information is concentrated in smaller frequencies, therefore the data are re-sampled at 256 Hz for all patients using the *resample* function in *Matlab* (see chapter 14 of (Ljung 1998)). The function applies an antialiasing lowpass filter in the form of a Kaiser window with cutoff frequency $\pi/4$ or $\pi/2$, and order 80 or 40 for signals with $f_s = 1024$ Hz and $f_s = 512$ Hz respectively, and then down-samples the filtered data.

The general data acquisition and processing schematics from the measured signals to the ones used for system identification is shown in Fig. 4.11. The last Butterworth low-pass filter is explained in the following subsection.

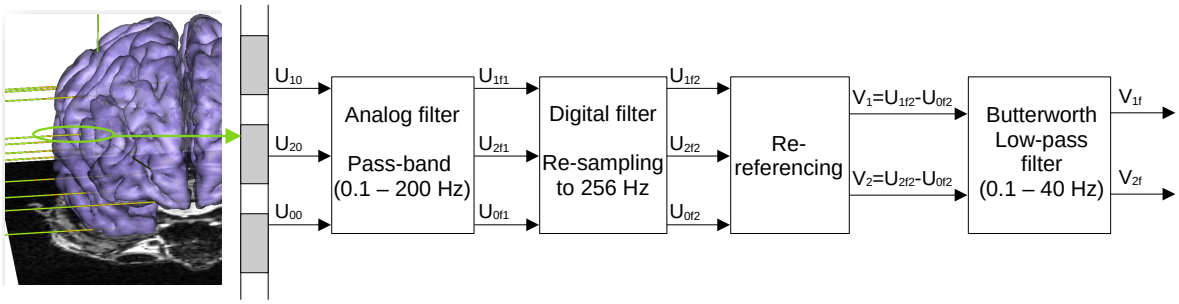


Figure 4.11: Schematic representing the SEEG data acquisition and processing before the identification algorithm.

### 4.2.4 Study of the frequency response

In the previous chapter, the non-parametric frequency responses of consecutive pairs of contacts were used for tissue classification. Because of the fact that in this case signals are re-referenced with respect to the consecutive contact after the second one of the pair, there might be some changes in the obtained frequency responses, compared to the ones obtained in the previous chapter.

Thus, the non-parametric frequency response is recalculated here to get more insight on the dynamics between the two re-referenced contacts. For it, the corresponding *Matlab* function *spa* is used, with a Hanning window of size 3.5 s. The size of the window is chosen as a high one in order not to loose information during the estimation. The average frequency response obtained from all combination of contacts over the 19 subjects considering 20s baseline signals is found in Fig 4.12a.

From the frequency response, it can be seen that the dynamics between two re-referenced contacts are frequency dependent, with a slight gain drop in higher frequencies. For a 50 Hz frequency, the gain and phase present a negative spike caused probably by a notch filter, which is repeated for 100 Hz, this indicates the presence of noise. Because of this, the signals $V_1$ and $V_2$ are filtered by a low pass Butterworth filter of order 6 and cutoff frequency of 40 Hz before they are used for identification (see Fig. 4.11). The resulting Bode diagram can be

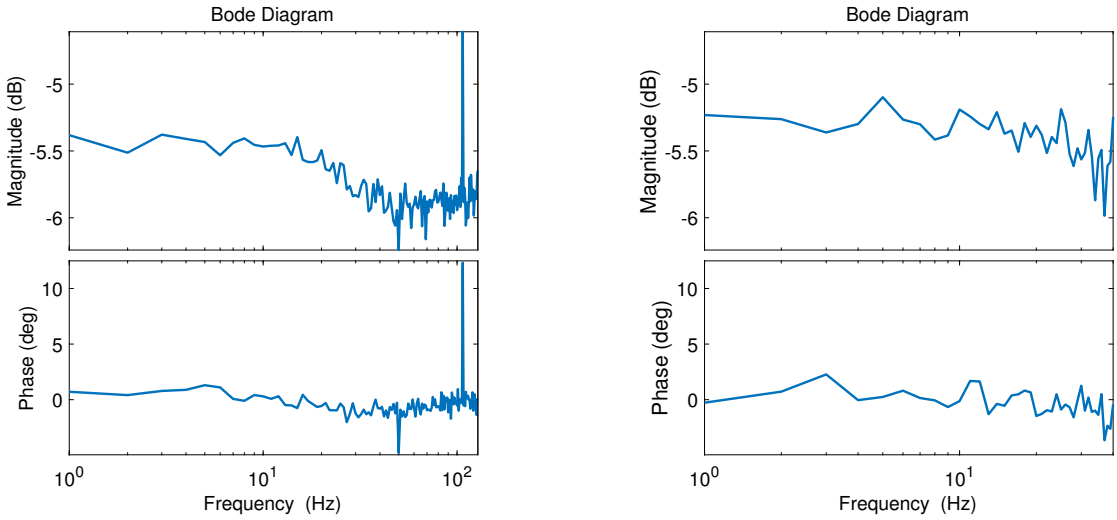


(a) Mean Bode

(b) Mean bode of filtered signals

Figure 4.12: (a) Bode plot of the mean frequency response obtained from the SPA of the data. (b) Bode plot obtained from the filtered data.

found in Fig. 4.12b.

### 4.2.5 Identification methodology

Given the number of coefficients to be identified, the nature of the signals used, as well as the complexity brought by the non-integer order derivative, the choice is made to use the interior point method instead of the RLS method used for the *phantom EEG* case. As mentioned in section 2.4, the interior point method allows for the optimisation of transfer function coefficients considering constraints, such as the positivity constraint necessary in this case as the transfer function coefficients are formed by the sums and multiplications of electronic components which are always positive.

As a reminder, the interior point optimisation problem can be described by the following:

$$\begin{aligned} \underset{x\in\mathbb{R}}{\text{minimize}} \quad & f(x) \\ \text{subject to} \quad & c(x) = 0 \\ & d(x) \geq 0 \end{aligned} \tag{4.69}$$

The aim is to find the values of $x$ that minimise the cost function $f(x)$ with respect to the equality and inequality constraints ($c(x)$ and $d(x)$). In Matlab, *fmincon* is designed to solve such a problem, and is used here. The details on the optimisation are given in the following subsections.

#### 4.2.5.1 Cost function

The aim of the identification problem is to find the regression coefficients $\hat{\theta}$ that minimise the difference between the output of the system $V_2$ and the output of the model $\hat{V}_2$. From the linear relationship between $\hat{V}_2$ and $\hat{\theta}$, a convex cost function can be easily written as the mean squared error as follows, with $N+1$ data samples:

$$f(\hat{\theta}) = \frac{1}{N+1} \sum_{k=1}^{N+1} (V_2(k) - \hat{V}_2(k, \hat{\theta}))^2 \tag{4.70}$$

As the magnitude of the signals is small, the error is also small and might make the solver converge to a bad point. Therefore, the cost function is harmonised by multiplying it by the inverse of the order of magnitude of the cost considering the initial point.

#### 4.2.5.2 Constraints

The first constraint to be implied is the positivity of the transfer function coefficients. This condition is necessary because they are formed by the sum of the electronic components which are always positive. In order to guarantee this positivity, the following constraints on the regression coefficients must be respected:

$$d1 : \hat{\theta} > 0 \tag{4.71}$$

$$d2 : \hat{a}_1 - h^{2\alpha} + \hat{a}_2 h^{\alpha} < 0 \tag{4.72}$$

$d1$ is deduced from the discretised transfer function coefficients of equations (4.53) - (4.57), and $d2$ is deduced from equations (4.64) - (4.68). In addition, looking at the transfer function coefficients in equations (4.41) to (4.45), the following constraints have to be added:

$$d3 : \hat{b}_1 < \hat{a}_1 \tag{4.73}$$

$$d4 : \hat{b}_2 < \hat{a}_2 \tag{4.74}$$

Finally, one equality constraint is added inspired by the results obtained with the non parametric frequency identification between pairs of adjacent contacts for tissue classification. Looking at the model, the static gain corresponds to $H(s \to 0) = B_3$. Thus, the transfer function coefficient $B_3$ can be directly identified from the frequency response obtained with equation (2.14). In order to impose the correct value of $B_3$ from the identified regression coefficients, the following constraint is written:

$$c1 : \hat{a}_1 B_3 - h^{2\alpha} B_3 + \hat{a}_2 B_3 h^{\alpha} + B_3 h^{2\alpha} = 0 \tag{4.75}$$

#### 4.2.5.3 Initial point

Even though the cost function is convex, the defined constraints introduce some non-linearities to the problem. Therefore, the results are dependent on the choice of the initial values of $\hat{\theta}$ ($\hat{\theta}_0$). This is why all previous knowledge on the values of $\hat{\theta}$ should be used to construct $\hat{\theta}_0$. It is known that the coefficients in $\hat{\theta}$ are a combination of the transfer function coefficients, which in turn are a combination of the electronic components. Based on (Lempka, Miocinovic, et al. 2009), (Carvallo et al. 2018), (Robinson 1968), and the previous *phantom EEG* study, the expected values should be as follows: $500\,\Omega < R_{med1} < 20\,k\Omega$, $500\,\Omega < R_{med2} < 20\,k\Omega$, $500\,\Omega < R_{en} < 20\,k\Omega$, $1\,k\Omega < R_{c1} < 2000\,k\Omega$, $1\,k\Omega < R_{c2} < 2000\,k\Omega$, $0.1\,\mu F < Q_{int} < 15\,\mu F$, and $0.1\,\mu F < Q_{cl} < 15\,\mu F$.

Considering the defined limits of the electronic components, the initial point $\hat{\theta}_0$ will be created by selecting random values of $R_{med1}$, $R_{en}$, $R_{ct}$, $R_{cl}$, $Q_{int}$, and $Q_{cl}$ constrained by the expected intervals. The values of $R_{med1}$ and $R_{med2}$ should be close in magnitude, considering that the distance between two contacts is small and conductivities of white and grey matter are known to be close to one another (Carvallo et al. 2018). Thus, the initial value of $R_{med2}$ is chosen by randomly adding or subtracting $200\Omega$ from $R_{med1}$.

Because of the different orders of magnitude of the electronic components, the resulting transfer function coefficients might also have the same problem. In optimisation, if the variables to be optimised have varying orders of magnitude, it is hard to guarantee a good fit for all of them. This is why a harmonisation of $\hat{\theta}$ is done. In it, all the coefficients are multiplied by the inverse of their orders of magnitude, and they are multiplied by their orders of magnitude when they appear in the cost function.

#### 4.2.5.4 Non-integer order

The optimisation problem is defined considering a fixed non-integer order value. However $\alpha$ remains unknown. Getting inspiration from (Besançon et al. 2019), the identification method is performed for different non-integer orders in the interval $0.6 < \alpha < 0.85$, and the $\alpha$ for which the identified model has the lowest cost is selected. The lower and upper bounds of the non-integer order are defined based on results obtained in (Besançon et al. 2019), and the results obtained on the *phantom EEG*.

#### 4.2.5.5 Identification using multiple recordings

During the SEEG procedure, the contacts can be recorded multiple different times. These different measurements can be used to enhance model estimation. For each patient, ten different recordings are randomly selected, and for each of them the identification method is applied using 20s of the baseline signals measured by the contacts. This results in ten identified models for each combination of three contacts. The final model is obtained by taking the average values of the coefficients of the ten separate models. This strategy reduces

errors induced by noisy signals. The number and duration of recordings is chosen as such to reduce computation time that can become quite extensive when considering more data.

#### 4.2.5.6 Model validation

As was mentioned in section 2.5, there are validation tests that need to be performed in order to guarantee if the identified coefficients are not biased. Given the ARX structure used here, to decide whether an identified model is biased or not, there are two validation tests that need to be performed. The chosen structure and identification method are based on the whitening of the prediction error $\varepsilon = V_2 - \hat{V}_2$. Therefore, the two tests to be performed are the whiteness and cross-correlation tests. The first one is used to see if $\varepsilon$ is a white noise. However, because of the fact that signals $V_1$ and $V_2$ are filtered, the resulting $\varepsilon$ will also be filtered, and therefore it is not a white noise. Thus, only the second cross-correlation test can be performed. Only the validated models are considered.

In addition, in order to properly guarantee identifiability, the input voltage needs to be sufficiently exciting. In other words, the signal should be sufficiently rich in frequencies. In the specific case of this study, baseline signals corresponding to the brain activity of patients at rest are used. In such conditions, the predominant brain waves observed are $\alpha$ (8-13 Hz), and possibly $\beta$ (13-30 Hz) depending on: a) brain region signals were recorded in, b) stress level, or c) whether patients had their eyes opened or closed. Indeed, when looking at the power spectral density estimate of one of the input signals in Fig. 4.13, the power is mostly concentrated between 1-40 Hz with a peak close to the $\alpha$, and $\beta$ frequency ranges, even though of low magnitude. To verify that the input signals were sufficiently rich, a model like the one presented in this paper was simulated, and stimulated with the same input signals. Using the identification algorithm described in this paper, the estimated parameters exactly recovered the model ones in absence of noise.

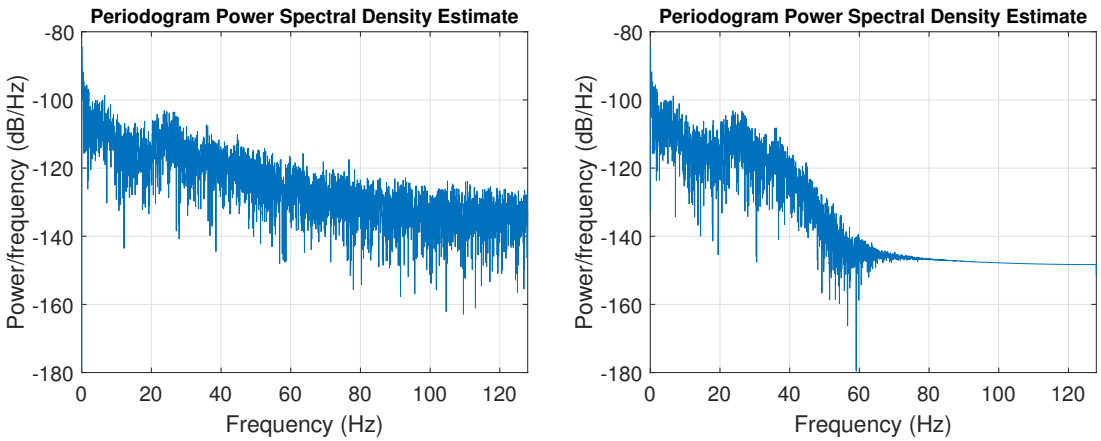


(a) (b)

Figure 4.13: Example of the power spectral density estimate of (a) input signal before low-pass filter at 40 Hz, and (b) input signal after 40 Hz low-pass filter.

The system identification of a trio of contacts considering one recording is summarised in Fig. 4.14.

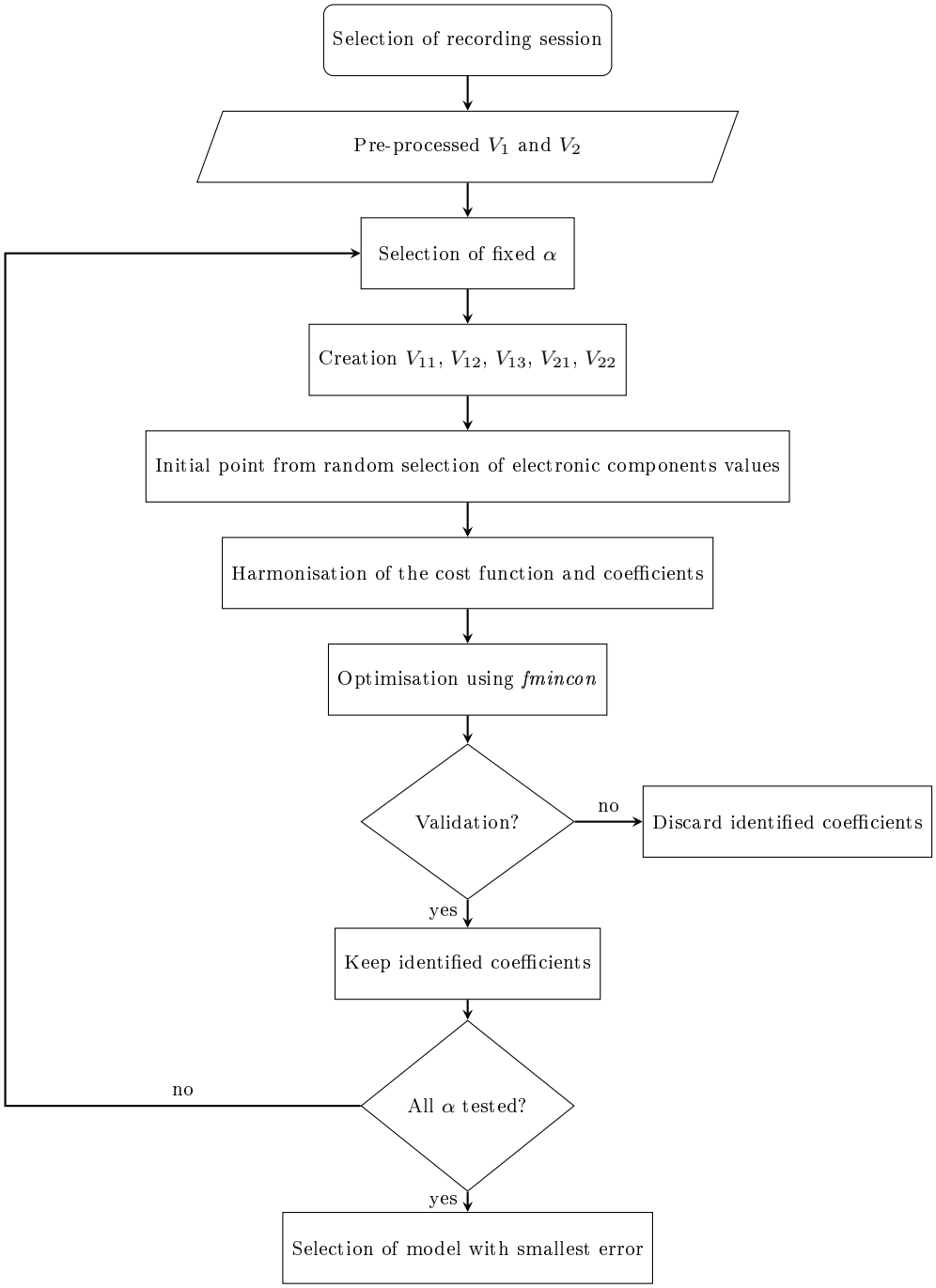


Figure 4.14: Flowchart representing the identification algorithm of a trio of contacts.

### 4.2.6 System identification results

The identification methodology is applied on data of the 19 epileptic patients. At each time, three consecutive contacts are considered, and together they constitute one triplet. The first contact is the shallower one, and the following two are located deeper in the brain. The signal of the deeper contact of the triplet is subtracted from the first and second contacts to create the input and output signals that are pre-processed using the procedure shown in Fig. 4.11. These input and output signals are used for the identification method.

A total of 356 triplets across all patients had validated models. In order to further see how well the models fit the data, the time and frequency responses of the identified models are compared to the data.

Five groups are studied separately according to the tissue composition between the three adjacent contacts following previous classification from co-registration of MRI with CT-scan. The group "Grey" (106 triplets) represents contacts combinations where the three contacts are in grey matter. Group "White" (95 triplets) is made of cases in which all contacts are in white matter. Groups "Grey/White" (73 triplets) and "White/Grey" (63 triplets) represent respectively cases in which there is more grey matter between the first and second contacts than between the second and reference contacts, and cases in which there is more white matter between the first and second contacts than between the second and reference contacts. The "mix" (19 triplets) group represents cases in which the quantity of grey and white matter is similar between the first and second contacts and the second and reference contacts.

The mean of the frequency domain responses of identified models and SEEG data are shown in Fig. 4.15 separated by groups depending on the tissue composition in between the three contacts. Only the first 40 Hz are shown because of the noise observed for higher frequencies.

By a visual inspection of Fig. 4.15, the identified models in red have similar dynamics to the SEEG data. Some small differences can be perceived in the static gain for some groups, even with the equality constraint given in equation (4.75). This can be justified from the fact that Bode plots are shown starting from 1 Hz, thus the gain value at 0 Hz is the same but it quickly changes due to high values of $B_2$ and $A_2$ that start acting at small frequencies.

Looking at the Nyquist plots in Fig. 4.15, some limitations can be seen with the model not covering all of the points, and for cases such as the "White" and "White/Grey" ones where the model has a semi-circle shape. This differences could be justified by the presence of noise even in small frequencies.

The fit in time is calculated quantitatively with the following normalised root mean squared error in percentage:

$$fit = 100\left(1 - \frac{||V_2 - \hat{V}_2||}{||V_2 - mean(V_2)||}\right) \tag{4.76}$$

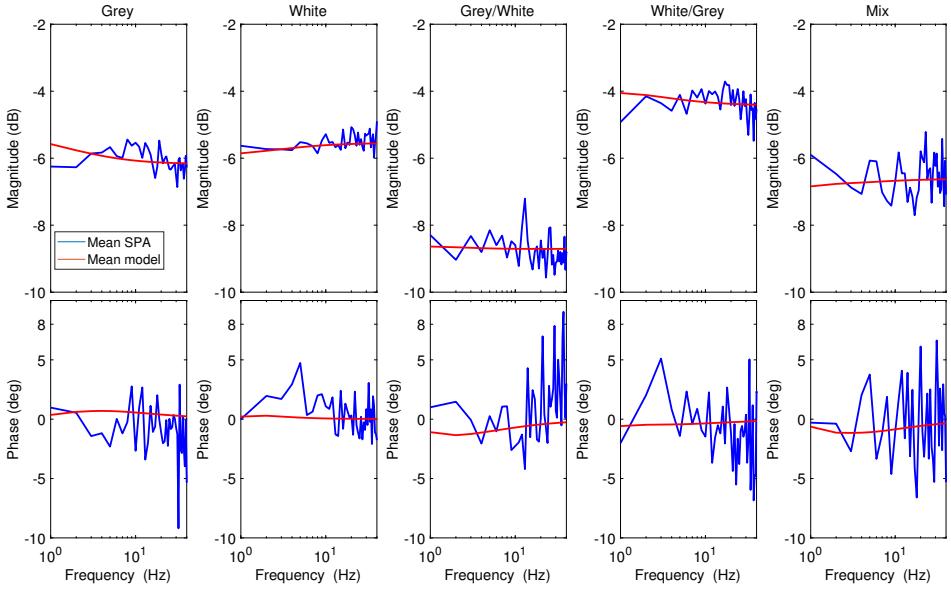


(a) Bode

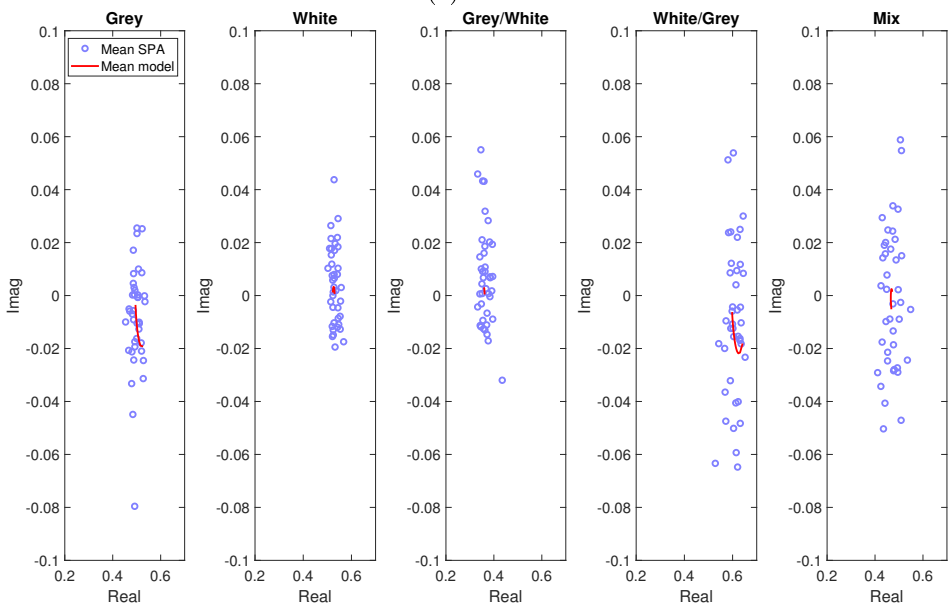


(b) Nyquist

Figure 4.15: Comparison between the identified models (in red), and the expected response from the data (in blue). In (a) the Bode plot of the mean frequency responses of the model of each tissue group is compared with their mean SPA frequency response. In (b) the corresponding Nyquist plots for the models in (a) are shown compared to the mean frequency responses obtained with SPA.

The mean values of $fit$ for each of the groups are: $94 \pm 3\%$ for the "Grey" group, $93 \pm 4\%$ for the "White" group, $93 \pm 4\%$ for the "Grey/White" group, $92 \pm 13\%$ for the "White/Grey" group, and $93 \pm 4\%$ for the "mix" group. These values represent a good fit of the identified model in time.

In addition, in Fig. 4.16, the ratio between the input signal energy and noise energy are shown for 32 identified models for one of the 19 patients. The energy of the input signal $u$ is approximated by its auto-correlation at the origin:

$$E_u \approx \frac{1}{N}\sum_{k=1}^{N}[u(k)]^2 \tag{4.77}$$

As for the noise energy ($E_v$), it can be approximated to the prediction error energy ($E_v \sim E_\varepsilon$), with $\varepsilon(k) = V_2(k) - \hat{V}_2(k, \hat{\theta})$, which is approximated to the estimated variance:

$$E_v \approx \frac{1}{N-d}\sum_{k=1}^{N}[\varepsilon(k)]^2 \tag{4.78}$$

with $d$ the length of vector $\theta$.

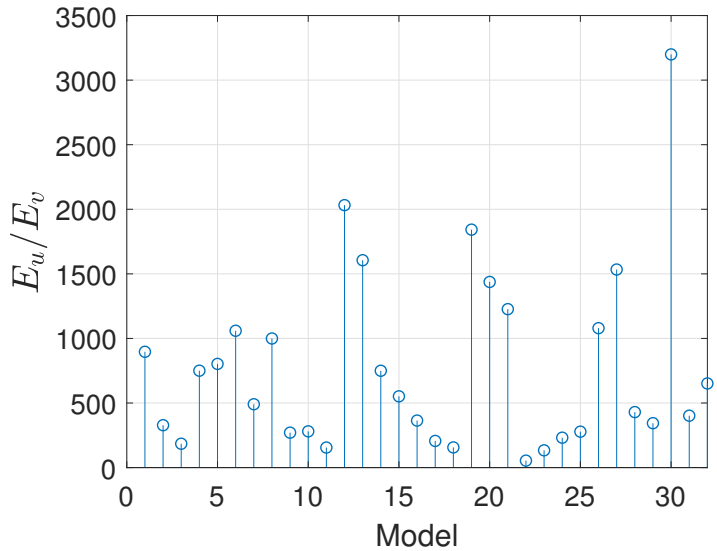


Figure 4.16: Ratio between input signal energy and noise signal energy for 32 identified models of one patient.

As it can be seen in Fig. 4.16 the input signal has sufficiently more energy when compared to the noise. This illustrates that the input has enough relevance for identification.

One can also use the ratio between the energy of the output of the model $E_{\hat{V}_2}$, and the energy of the noise $E_v$, to illustrate the boundedness of the prediction error, considering:

$$E_{\hat{V}_2} \approx \frac{1}{N}\sum_{k=1}^{N}[\hat{V}_2(k)]^2 \tag{4.79}$$

The report between $E_{\hat{V}_2}$, and $E_v$ represents the signal to noise ratio of the output of the

model, and can be found in Fig. 4.17 for 32 different models of 1 patient. As it can be seen, the difference in energy of the output of the model and the prediction error is significant.

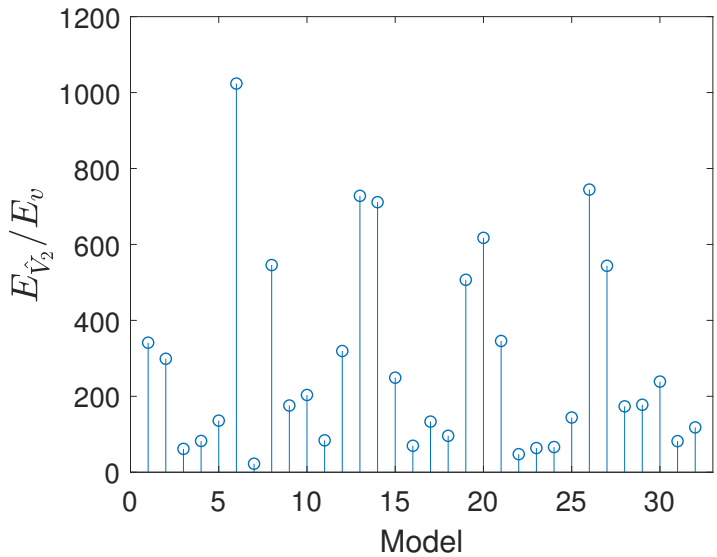


Figure 4.17: Ratio between the energy of the output of the model and the noise for 32 identified models of one patient.

As in the case of integer order system identification, the choice of the discretization method (in this case discrete approximation of the non-integer order derivative) has an influence on the identified system, as it is used to create the regression vectors (given in equations (4.52) and (4.58)). The same can be said for the sampling period $h$. In the case of this study where the Grünwald–Letnikov approximation is used, the smaller the $h$ the better the non-integer approximation is to the non-integer order derivative (see (Scherer et al. 2011)).
The sampling frequency used here (256 Hz) is approximately eight times larger than the 30 Hz of the $\beta$ brain activity, making it sufficiently large. However, if the method is also applied to measured signals during brain stimulation in the future, the sampling frequency may be higher, and the 40 Hz low-pass filter may be removed from the pipeline.

The distribution of transfer function coefficients as well as non-integer order is given in Fig. 4.18. It can be seen that there is not a lot of discrepancy between the orders of magnitude of the coefficients, with $B_2$ and $A_2$ being higher in general. One can also verify that the constraints given in equations (4.73) and (4.74) are respected, with the median value of $A_1$ being higher than the median value of $B_1$, and the median value of $A_2$ being higher than $B_2$. It can also be seen that the positivity constraint is respected.

Furthermore, there is very little variance on the non-integer order $\alpha$ which is for most cases equal to 0.8 which is an indicator that the non-integer orders do not depend on the tissue the contacts are inserted in.

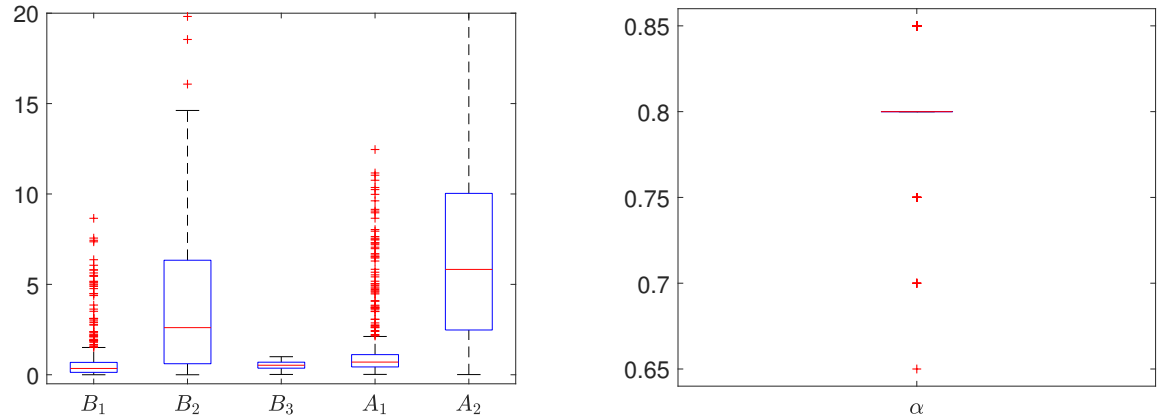


(a) Transfer function coefficients

(b) Non-integer orders

Figure 4.18: Boxplot representing (a) the distribution of transfer function coefficients, and (b) the distribution of non-integer orders.

## 4.3 Tissue conductivity analysis and classification

Due to the complexity of the proposed model and the type of data available, the values of electronic components can not be directly retrieved from the identified transfer function coefficients. However, equations (4.46), (4.47), and (4.48) can be used to get a comparison of the resistance of different tissues.

Fig. 4.19a shows a boxplot of the distribution of $(B_1/A_1)$ according to the tissue in which each of the contacts is inserted in following previous classification, Fig. 4.19b shows a boxplot of the distribution of $(B_2/A_2)$, and Fig. 4.19c shows a boxplot of the distribution of $(B_3)$.

For the cases "Grey" and "White", as $R_{med1} = R_{med2}$, the values of $(B_1/A_1)$, $(B_2/A_2)$, and $B_3$ are expected to be close to 0.5 for the homogeneous groups, which can be observed in Fig. 4.19.

It can also be observed that the "Grey/White" group has values of $(B_1/A_1)$, $(B_2/A_2)$, and $B_3$ smaller than 0.5, which indicates $R_{med1} > R_{med2}$. The exact opposite is observed for the "White/Grey" case in which for all of the cases the values are bigger than 0.5, which suggests $R_{med1} < R_{med2}$.

In the "mix" group, as there is the same amount of grey and white tissue in between the first and second contacts and the second and third contacts, $R_{med1} = R_{med2}$, which means that $(B_1/A_1)$, $(B_2/A_2)$, and $B_3$ should be close to 0.5. This is what is seen in Fig. 4.19a, Fig. 4.19b, and Fig. 4.19c.

The observed results are consistent with one another, and are in accordance with the fact that the resistance in white matter is smaller than the resistance in grey matter. Notice that in the literature there are opposing views as to the exact conductivity of different brain

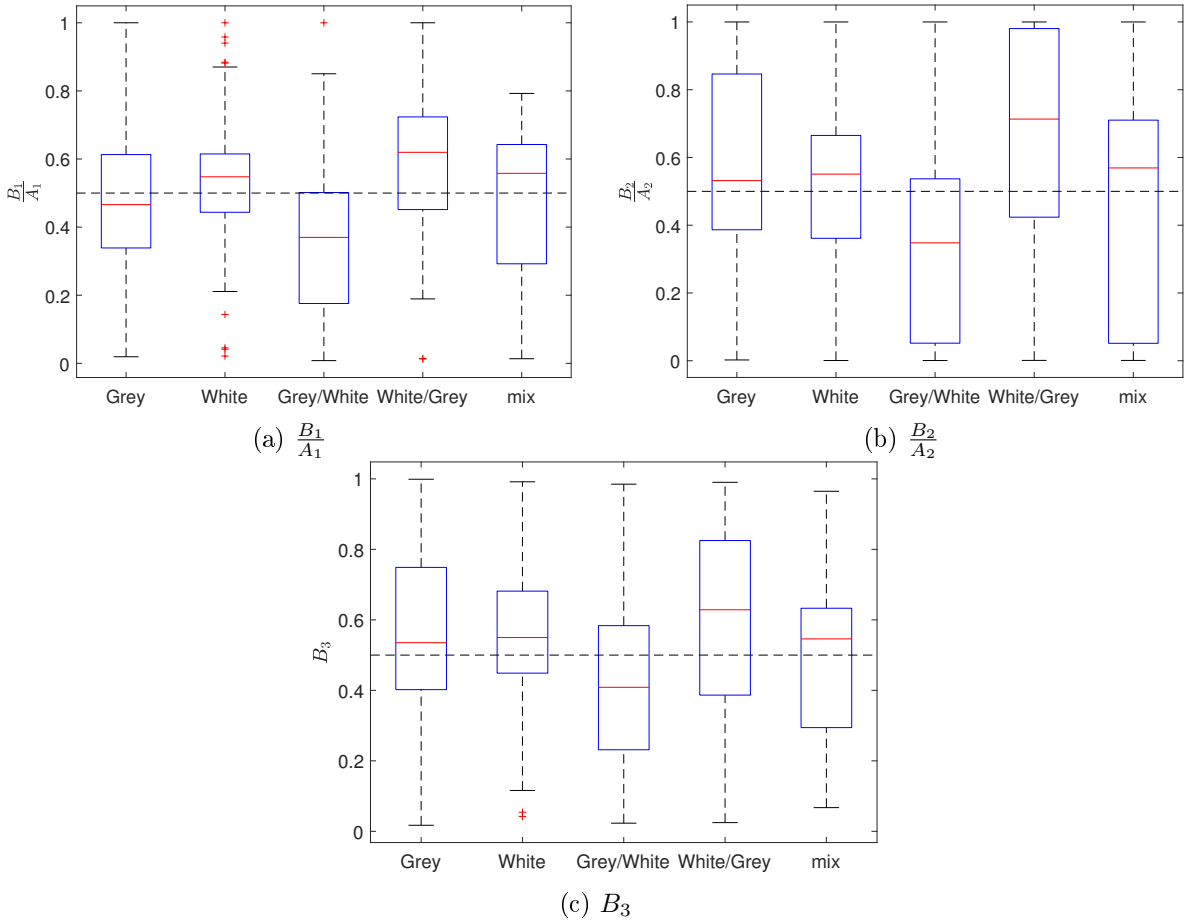


Figure 4.19: Boxplot representing the distribution of the values of $B_1/A_1$ in (a), of $B_2/A_2$ in (b), and of $B_3$ in (c), in respect to the tissue classification of the trio of contacts according to the co-registration of the CT-scan and MRI.

tissues. The differences observed arise from the fact that the conductivity measurements are not always performed under the same circumstances (varying methodologies of brain signal acquisition, different patient pathologies, etc.) as indicated in (McCann et al. 2019). In the cases of (Carvallo et al. 2018), and (Geddes et al. 1967) for example, the resistance of white matter is considered to be higher than the one in grey matter. In (Carvallo et al. 2018), the conductivities were measured in two different patients via the stimulation of SEEG contacts. In (Geddes et al. 1967) the values of tissue resistances measured in animals either *in vitro* or *in vivo* are shown. On the other hand, (Satzer et al. 2015) reports higher measured conductivities in white matter than grey matter when measuring the impedance of chronically implanted electrodes in 73 patients suffering with Parkinson's disease. In general, (Logothetis et al. 2007), the conductivity of white matter depends in fact on fiber orientation and it can take values that can be either greater or smaller than grey matter. Thus, the results of this study, being consistent with each other, are also comparable to previous literature.

To test the discrimination power of $(B_1/A_1)$, $(B_2/A_2)$, and $B_3$ for the heterogeneous cases

(Grey/White and White/Grey), a simple linear discriminant analysis (LDA) classifier is used for each of the features separately. The data is split into $K = 4$ different subsets. 3 of such subsets were used for the training of the model, and the remaining ones for validation. This process is repeated until all possible combinations of test and training subsets are used. For each case the accuracy of the classification is calculated, and the final value consists in the mean accuracy over all combinations. This process is repeated 50 times to get a more robust estimation of the classifiers performance.

The accuracy of group separation of each of the combinations of transfer function coefficients is shown in Table 4.5. $(B_1/A_1)$ is the most discriminant when it comes to group separation between Grey/White and White/Grey groups. The accuracy is not improved when using features together.

| | Accuracy (%) |
|---|---|
| $(B_1/A_1)$ | $73 \pm 6\%$ |
| $(B_2/A_2)$ | $71 \pm 7\%$ |
| $B_3$ | $68 \pm 6\%$ |

Table 4.5: Accuracies of heterogeneous group separation of combinations of transfer function coefficients using a LDA classifier.

The value of $73 \pm 6\%$ accuracy is very close to the one obtained in the previous study of brain tissue classification using the non-parametric frequency responses of SEEG signals referenced in distant white matter. In that case, an accuracy of $72 \pm 3\%$ was obtained for homogeneous tissue separation using an LDA classifier for the same 19 patients from this study.

Thus, the information obtained from the identification of the proposed model is indeed useful for classification of brain tissues, with an additional insight in the differences in conductivity of grey and white matter.

## 4.4 Discussion on the choice of the model

The proposed model in the form of an electronic circuit represents the physical properties of the brain-electrode interface. It is based in previous literature (see (Sankar et al. 2014), (Lempka, Miocinovic, et al. 2009), and (M. Johnson et al. 2005)), and yields good visual fits to the frequency response obtained from the SPA of the data as well as good quantitative fits in time when comparing the real output to the model output.

One might argue that the gain drop observed in higher frequencies as well as the phase shift in Fig.4.12 are not very significant, as if the system had no dynamics and could be approximated by a simple gain. In this case, the circuit can be simplified to a purely resistive one, as seen in Fig. 4.20.

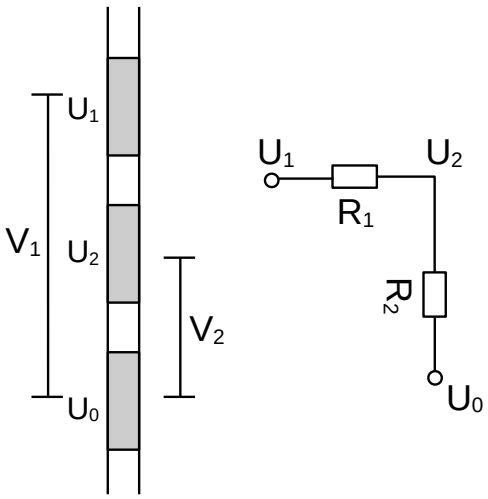


Figure 4.20: Simplified circuit based on the hypothesis of the model being represented by a simple gain.

For which the transfer function is given as:

$$V_2 = \frac{R_2}{R_1 + R_2} V_1 = gV_1 \tag{4.80}$$

One reason why the complex model could be confounded with a purely resistive one is that the numerator and denominator of the transfer function of equation (4.40) are of the same order. Moreover, the coefficients $B_1$ and $A_1$ are very close in magnitude, the same can be said about coefficients $B_2$, and $A_2$ (see Fig. 4.18a), with $A_1 > B_1$, and $A_2 > B_2$. Thus, if the poles and zeros act in the same frequencies with similar intensity, the gain remains almost constant.

In order to test the hypothesis that the model can be described by a simple gain, $g$ is identified for each combination of three contacts, using the mean frequency response obtained using SPA for 10 recording sessions $\hat{G}_{SPA}$. The resulting gain for a trio of consecutive contacts $i$ is given by:

$$g_i = \left| \frac{1}{N_f} \sum_{f \in [0,40]} \hat{G}_{SPA}(f) \right| \tag{4.81}$$

with $N_f$ the number of frequency points on the band 0-40 Hz.

The frequency responses of the simple resistor model are compared to the ones obtained from the SPA and the complete model presented in the previous subsections, and can be found in Fig. 4.21. It can be seen that the purely resistive model fits the frequency responses obtained with SPA well, even if a part of the dynamics is not represented when comparing to the complete model.

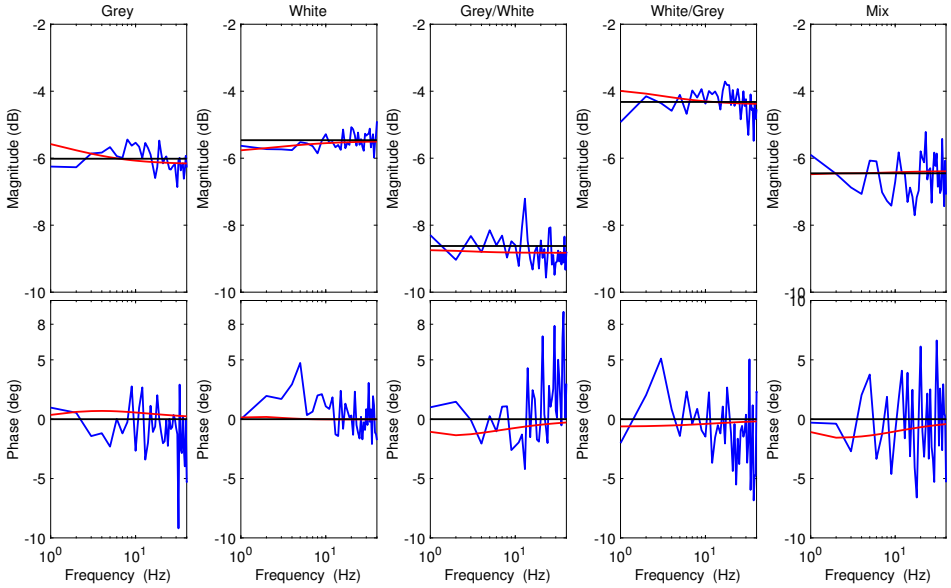


(a) Bode

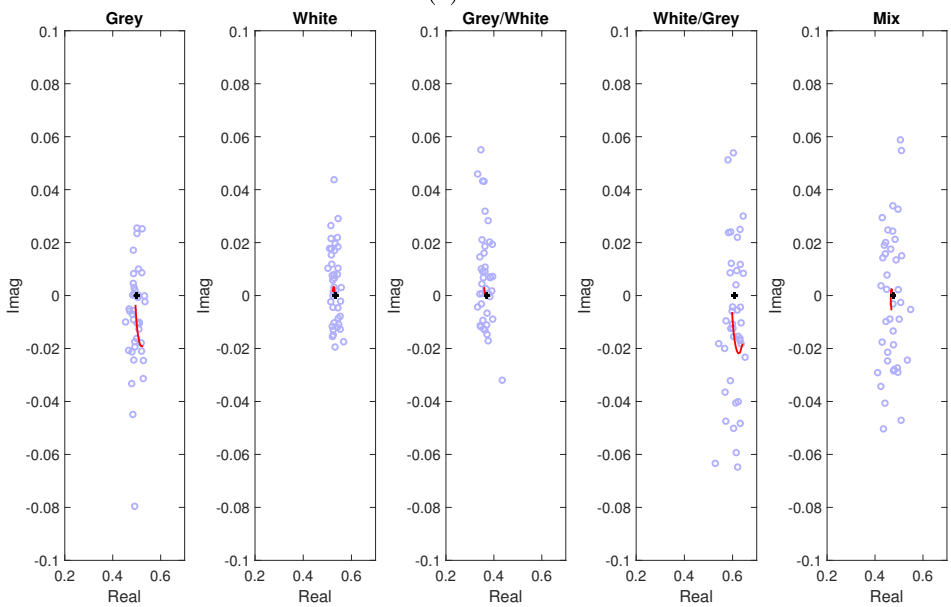


(b) Nyquist

Figure 4.21: Comparison between the identified complete model (in red), the expected response from the data (in blue), and the identified gain for the purely resistive model (in black). In (a) the Bode plots. In (b) the corresponding Nyquist plots for the models in (a).

As mentioned the hypothesis as to why the complex model presented in the previous subsection can be simplified to a purely resistive one lies on the fact that the orders of the numerator and denominator of the transfer function are the same, with zeros and poles operating in similar orders of magnitude.

In order to verify this hypothesis, one can analyse the variation of the real and imaginary

parts of the transfer function of equation (4.40) in relation to the frequency:

$$\mathrm{Re}(H(s)) = \frac{A_1B_1\omega^{4\alpha} + (A_1B_2 + A_2B_1)\omega^{3\alpha}cos(\pi\alpha/2) + (B_1 + A_1B_3)\omega^{2\alpha}cos(\pi\alpha)}{A_1\omega^{4\alpha} + A_1A_2\omega^{3\alpha}2cos(\pi\alpha/2) + \omega^{2\alpha}(A_1cos(\pi\alpha) + A_2^2) + A_2\omega^{\alpha}2cos(\pi\alpha/2) + 1}$$
$$+ \frac{A_2B_2\omega^{2\alpha} + (B_2 + A_2B_3)\omega^{\alpha}cos(\pi\alpha/2) + B_3}{A_1\omega^{4\alpha} + A_1A_2\omega^{3\alpha}2cos(\pi\alpha/2) + \omega^{2\alpha}(A_1cos(\pi\alpha) + A_2^2) + A_2\omega^{\alpha}2cos(\pi\alpha/2) + 1} \quad (4.82)$$

$$\mathrm{Im}(H(s)) = \frac{(A_2B_1 - A_1B_2)\omega^{3\alpha}sin(\pi\alpha/2) + (B_1 - A_1B_3)\omega^{2\alpha}sin(\pi\alpha)}{A_1\omega^{4\alpha} + A_1A_2\omega^{3\alpha}2cos(\pi\alpha/2) + \omega^{2\alpha}(A_1cos(\pi\alpha) + A_2^2) + A_2\omega^{\alpha}2cos(\pi\alpha/2) + 1}$$
$$+ \frac{(B_2 - A_2B_3)\omega^{\alpha}sin(\pi\alpha/2)}{A_1\omega^{4\alpha} + A_1A_2\omega^{3\alpha}2cos(\pi\alpha/2) + \omega^{2\alpha}(A_1cos(\pi\alpha) + A_2^2) + A_2\omega^{\alpha}2cos(\pi\alpha/2) + 1} \quad (4.83)$$

Considering the median values of the identified transfer function coefficients in Fig. 4.18a [$B_1 = 0.35$, $B_2 = 2.6$, $B_3 = 0.53$, $A_1 = 0.7$, $A_2 = 5.8$], and the median value of the non-integer order in Fig. 4.18b $\alpha = 0.8$, the evolution of the real and imaginary parts of the transfer function in frequency can be seen in Fig. 4.22a and the corresponding Nyquist plot can be found in Fig. 4.22b. It can be seen that the real part does not change a lot depending on the frequency, and quickly assumes a final value.

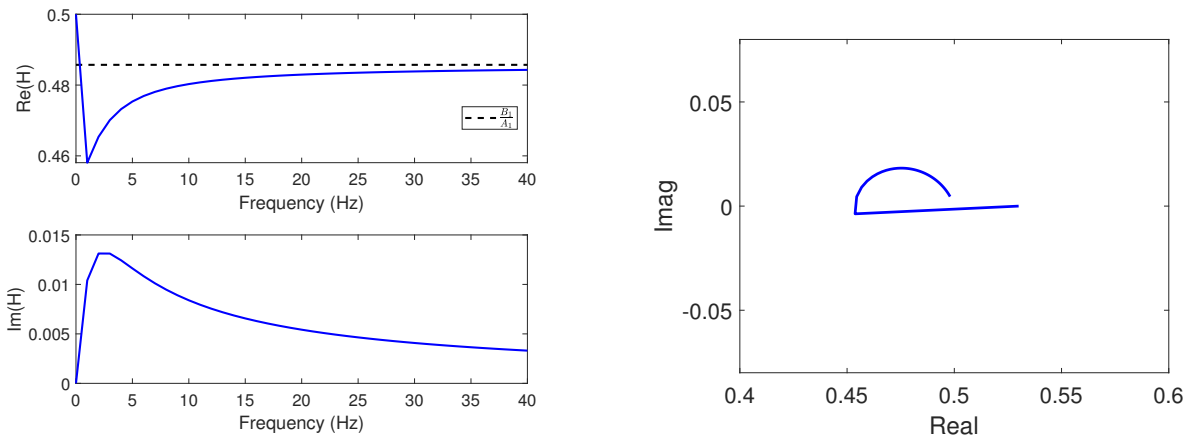


(a) Real and imaginary parts (b) Nyquist

Figure 4.22: Evolution in frequency of the real and imaginary parts of the transfer function considering the medians of the identified values and non-integer order. In (a) the real and imaginary parts are presented separately, and in (b) the resulting Nyquist is presented.

Looking at equation (4.82), when $\omega \to \infty$, the real part assumes a constant value:

$$\mathrm{Re}(H(s \to \infty)) = \frac{A_1B_1\omega^{4\alpha}}{A_1^2\omega^{4\alpha}} = \frac{B_1}{A_1} \quad (4.84)$$

In Fig. 4.22a, the value of $(B_1/A_1)$ is plotted together with the real part of the transfer function, and indeed the value to which the real part converges is $(B_1/A_1)$.

For the imaginary part of the transfer function, it can be seen that it also does not change a lot depending on the frequency, and its values are in general close to zero. This can be justified from the fact that when looking at equation (4.83), considering that the transfer function coefficients are close in magnitude, the subtractions present in the numerator make it close to zero.

In general, the value that dominates the transfer function of the model for most frequencies is $(B_1/A_1)$. Thus, the identified gain values $g$ of the purely resistive model should have similar values to $(B_1/A_1)$ of the complex model. To verify this they are plotted close to one another in Fig. 4.23.

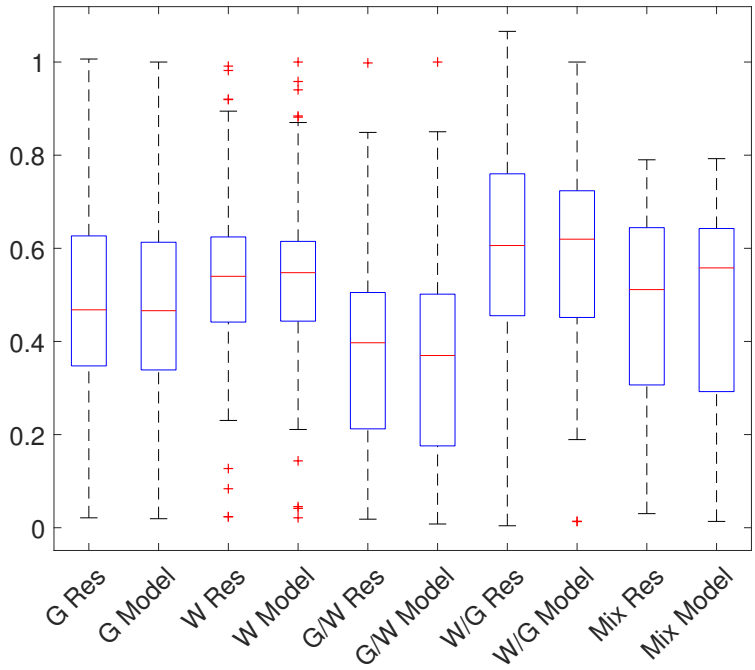


Figure 4.23: Boxplot comparing the distributions of the gain $g$ of the purely resistive model and $(B_1/A_1)$ of the complex model.

As it can be seen, the distribution of $g$ and $(B_1/A_1)$ is very similar for every group of contact trios. Thus, one can make the following approximation: $g = B_1/A_1$, which leads to:

$$R_1 = R_{med1} + 2R_{en} \tag{4.85}$$

$$R_2 = R_{med2} + 2R_{en} \tag{4.86}$$

As for the discrimination power of $g$, using an LDA classifier trained in the same way as described in section 4.3, the obtained accuracy is $73 \pm 6\%$ which is exactly the same accuracy

obtained for $(B_1/A_1)$ of the complex model. For $R_{med1}$ and $R_{med2}$ to have such an impact in the value of $(B_1/A_1)$ and $(1/B_3)$, it means that the orders of magnitude of $R_{cl}$, $R_{ct}$, and $R_{en}$ should either be close to the ones of $R_{med1}$, and $R_{med2}$, or smaller.

The results for tissue classification of heterogeneous triplets of contacts considering the less complicated resistive circuit are the same as for the more complete circuit. Nonetheless, the most complex model accounts for some dynamics that can not be visualised for the resistive circuit. It has been shown that one can go from the complex model of the brain-electrode interface based in previous literature to the simple resistive circuit because of the fact that the transfer function zeros and poles act in similar frequencies in similar intensities, being dominated most of the time by $(B_1/A_1)$.

In terms of identifiability of the system, one can not retrieve the precise electronic components values, only an idea of their order of magnitude, which seems to be close for all resistors. However, the information from the identified coefficients can still be useful for tissue classification. For simplicity reasons and for the sole purpose of tissue classification, one might opt to adopt the simple resistive model.

## 4.5 Conclusions

In this chapter, the modelling of the brain-electrode interface was discussed with the aim of using it for brain tissue classification. The main model proposed and discussed here consists of an electronic circuit of non-integer order, and it is based on previous literature. However, to our knowledge, such model has not yet been identified using typical baseline signals measured during SEEG investigation.

Before the study of the brain-electrode interface strictly speaking, a study was conducted on the modelling of the electrode-electrolyte interface via a *phantom EEG* device. The setup was previously presented in literature, and a model was proposed based on the shape of the frequency response obtained from the data. In the case of this study, however, there is an interest in modelling the *phantom EEG* measurement chain from the physical properties stand point, in which the model is separated in electrode, electrode-electrolyte interface, and propagation medium. The identification methodology of such model was shown in this chapter, and the resulting identified coefficients were used to recover the values of each of the physical components of the measurement chain. These values served as a good starting point for the modelling of the brain-electrode interface, mainly when it comes to the initial values considered for the electrode-electrolyte interface.

After the study on the *phantom EEG* measurement chain, a strategy of model identification of the brain-electrode interface using baseline SEEG signals of three consecutive contacts was proposed. The model was based on the physical properties of the brain-electrode interface discussed in literature. A total of 356 triplets of contacts had validated models with a good fit in the time and frequency domains. Because the relationship between transfer function coefficients and values of electronic components is not bijective, the latter could not be retrieved

separately. Nonetheless, the ratio between transfer function coefficients can be used for tissue classification with up to $73 \pm 6\%$ accuracy in group separation when it comes to heterogeneous tissue among the triplets of contacts. Such results in accuracy are very similar to the ones obtained in the previous chapter for homogeneous group separation when using the frequency response of two consecutive contacts.

Because of the similar order of magnitude of the numerator and denominator transfer function coefficients operating at similar frequencies, the model can be approximated to a simply resistive one. With this simplification, there is a loss in the system dynamics, however the classification results are the same.

The results reveal smaller electrical resistances in white matter compared to grey matter. In literature, there are conflicting values of conductivities of different brain tissues. Results depend largely on fiber orientation in white matter, and measurements circumstances. Nonetheless, the results in this study are consistent with one another when considering different tissue compositions.

As mentioned, the fits in the time and frequency domains of the complex model are good compared to the expected responses from the data. However, when looking at the Nyquist plots specifically, there is a part of the expected response from the data that is not represented by the identified models. It is unclear if this is because of the noise, or because of model or identification algorithm limitations. Thus, as a perspective of the work presented here, further exploration should be done to improve the fit of the Nyquist plot of the model to the expected one from data.

The system identification methodology proposed here could be combined with the results of the previous chapter, to estimate tissue distribution between three consecutive SEEG contacts. This study is presented in the next chapter.

Chapter 5

# Brain tissue classification combining non-parametric and parametric approaches

In the previous chapters, two different approaches for brain tissue classification were proposed. In chapter 3, the best classification results were obtained for pairs of contacts in homogeneous tissues considering their identified non-parametric frequency responses. In chapter 4, classification was performed for trios of contacts in heterogeneous matter with the use of identified models of the brain-electrode interface.

Here, the idea is to propose two ways of combining both methods in order to have a classifier that can be used for contacts both in homogeneous and heterogeneous combinations of tissues. The first way of combining the methods is proposed for the classification of trios of consecutive contacts. The second way of combining the methods is used for single contact classification and elimination of bad cases. The analysis in the following sections are done using data from the same 19 epileptic patients presented in chapter 3.

## 5.1 Classification of contact trios

As mentioned the parametric method can be used for heterogeneous tissue classification of contact trios, and the non-parametric method can be used for homogeneous tissue classification of contact pairs. The idea here is to use the parametric approach for separating heterogeneous from homogeneous groups, then use the parametric approach for heterogeneous tissue classification, and the non-parametric approach for homogeneous tissue classification. This procedure is described in the following subsections for the 356 trios with validated models.

### 5.1.1 First analysis considering the parametric model approach

From the model identification of trios of consecutive contacts proposed in chapter 4, the ratio of transfer function coefficients $(B_1/A_1)$ is used to discriminate between trios of contacts inserted heterogeneous tissues. If $(B_1/A_1) = 0.5$, the matter in which the trio of contacts are inserted in is either homogeneous, or there is the same proportions of grey and white matter

between the first and second contacts, and between the second and third contacts. If there is more grey matter between the first and second contacts than between the second and third contacts, $(B_1/A_1) < 0.5$. On the other hand, if there is more white matter between the first and the second contacts than between the third and second contacts $(B_1/A_1) > 0.5$.

Thus, the model approach can be used at first to divide trios of electrodes into two clusters: One composed of homogeneous groups "Grey" and "White", and the "Mix" group, and the second composed by the heterogeneous groups "Grey/White" and "White/Grey".

The clusters can be defined by simple thresholds that can be chosen to be conservative or not. Here, the choice was made considering the 25th and 75th percentiles of the distributions of homogeneous "Grey" and and "White" groups in Fig. 4.23, and also by looking at the distribution of the "Grey/White", and "White/Grey" groups in Fig. 5.1. The majority of contact trios located in homogeneous tissue have $0.4 \leq (B_1/A_1) \leq 0.6$. Moreover, the biggest intersection between the heterogeneous groups also occur for $0.4 \leq (B_1/A_1) \leq 0.6$, making 0.4 and 0.6 the lower and upper thresholds respectively.

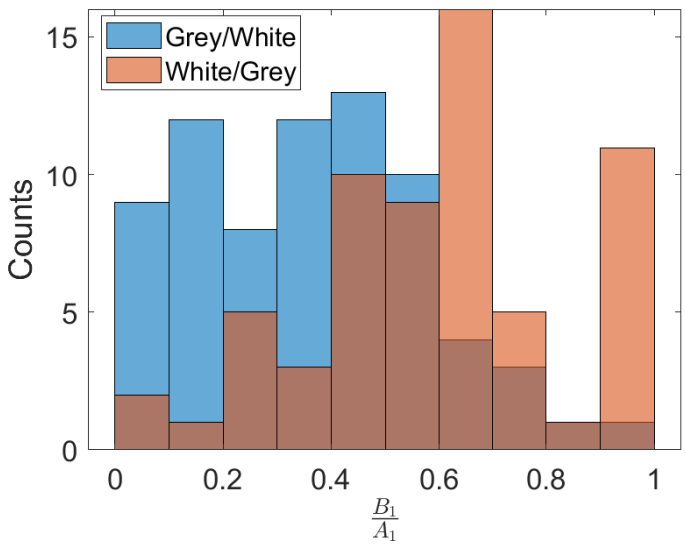


Figure 5.1: Distribution of the values of $(B_1/A_1)$ considering the heterogeneous groups "Grey/White", and "White/Grey".

If $0.4 \leq (B_1/A_1) \leq 0.6$ the tissue between the first and second contacts is assumed to be of the same composition as the one between the second and third contacts, and the trio is considered to be part of the first cluster. The remaining trios of contacts are considered to be part of the second cluster, with heterogeneous tissue distribution between the first two and the second two contacts. For the second cluster, the classification can be done directly from the values of $(B_1/A_1)$. If $(B_1/A_1) < 0.4$, the trio of contacts can be classified as being a part of the "Grey/White" group, and if $(B_1/A_1) > 0.6$ the trio of contacts can be classified as being a part of the "White/Grey" group.

### 5.1.2 Second analysis considering the non-parametric approach

In the previous section, the model based approach was used to separate trios of consecutive contacts into two clusters, one where the tissue distribution between the first and second contacts was the same as the distribution between the second and third contacts, and the other where there is an heterogeneous mixture of tissues between the first and second contacts and between the second and third contacts.

In the case of the second cluster the classification can be directly done using the model approach. However, for the first cluster, the values of $(B_1/A_1)$ are similar, and one cannot use them to classify homogeneous tissue combinations. This is why, for the classification of the first cluster, the non-parametric approach is used, more specifically the non-parametric frequency domain identification method, as it can differentiate between homogeneous tissue groups.

For each of the trios of contacts in the first cluster, the non-parametric frequency response of the first two contacts in monopolar reference is calculated following the procedure described in section 3.3. The LDA classifier presented in section 3.3.3 is used to classify the pairs of contacts using features extracted from the identified frequency responses. However, this classification method can only differentiate between homogeneous "Grey" and "White" groups, and not the "Mix" group.

The solution in this case would be to look at the posterior probabilities (see equation (3.8)) of the pair of electrodes belonging to the "Grey" and "White" groups. If $\hat{P}(G/G|x) > 60\%$ than the pair of contacts, and consequently the trio of contacts can be considered to be inserted in homogeneous grey matter being a part of group "Grey". If $\hat{P}(G/G|x) < 40\%$ than the pair of contacts, and consequently the trio of contacts can be considered to be inserted in homogeneous white matter being a part of group "White". However, if $40\% \leq \hat{P}(G/G|x) \leq 60\%$, the tissue between the first and the second contacts is probably heterogeneous, and therefore the trio of contacts can be considered to be a part of the "Mix" group. With this, all combinations of tissues between a trio of consecutive contacts can be classified.

In the case of the trios of contacts of the second cluster previously classified by the model approach method, the classification via the non-parametric frequency identification of the first two contacts of the trio in monopolar montage could be used to have a better idea of the label of each of the contacts. The heterogeneous group "Grey/White", for example, indicates that there is more grey tissue in between the first and second contacts than in between the second and third contacts. However, this could either mean that the first and second contacts are located in grey matter and the third in white matter, or that the first contact is in grey matter and the second and third contacts are in white matter. Thus, if one wishes to get a better idea of the distributions of each tissue for each contact specifically, taking the first two contacts of a trio in the second cluster, if $\hat{P}(G/G|x)$ is high it means that the tissue between the first and second contacts is likely to be homogeneous, and if $\hat{P}(G/G|x)$ is close to 0.5, it means that the tissue between the first and second contacts is likely to be heterogeneous.

### 5.1.3 Results combining both approaches

From the two analysis described in the previous sections, the overall tissue classification method of trios of consecutive contacts can be summarised by the schematic presented in Fig. 5.2.

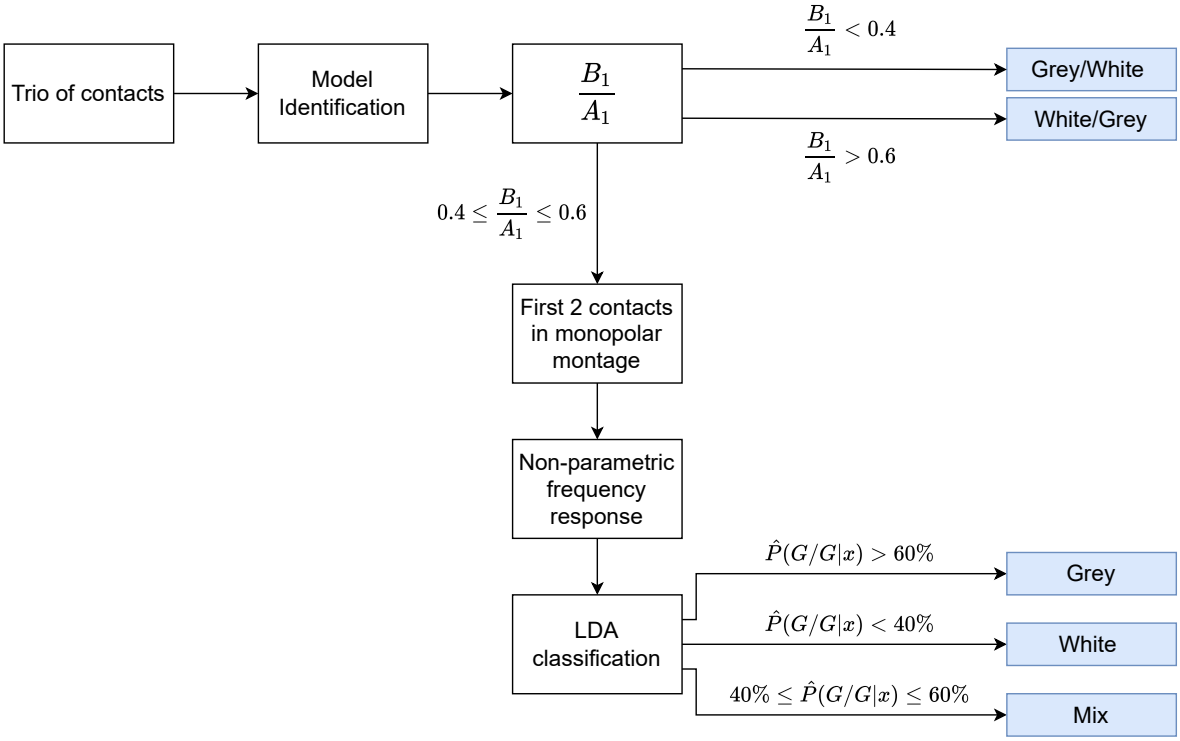


Figure 5.2: Complete tissue classification method, considering both non-parametric and parametric approaches.

The classification method is applied to the trios of consecutive contacts studied in chapter 4. In Fig. 5.3 the previous labels obtained from the co-registration of MRI with the CT-scan of patients are compared to the labels obtained using the classification method proposed here. For each of the previous labels, the distribution of new labels is show in percentage.

From Fig. 5.3 it can be seen that the groups for which there is a higher compatibility between MRI labels and new labels are the heterogeneous "Grey/White" and "White/Grey" groups. 56% of the trios previously classified as "Grey/White" from the MRI were also classified as "Grey/White" with the new method, and 52% of the trios previously classified as "White/Grey" from the MRI were also classified as "White/Grey". For the "Grey/White" group according to MRI classification, there is a larger number of trios classified as being in homogeneous grey matter, than homogeneous white matter. For the "White/Grey" group according to MRI, the number of trios being classified as being a part of homogeneous white matter is larger than the number of trios being in homogeneous grey matter.

For the previously classified homogeneous groups "Grey" and "White", the majority of

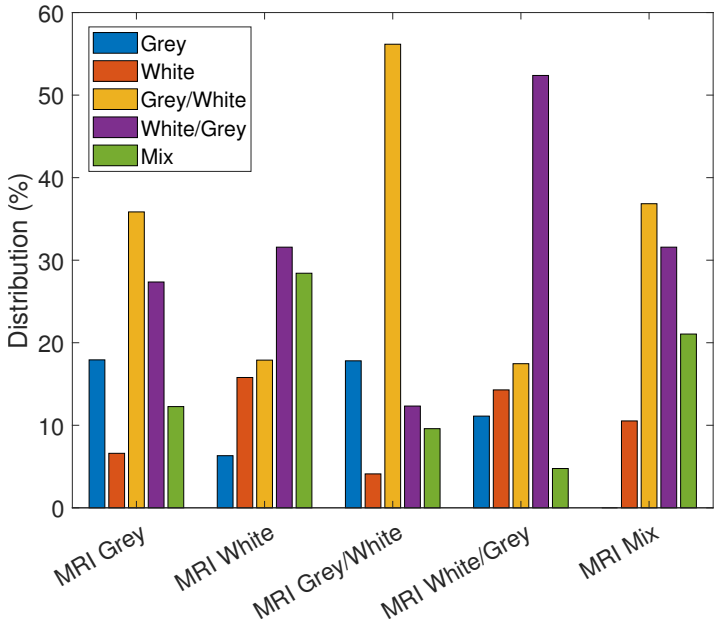


Figure 5.3: Distribution of labels from new classification method with regard to the co-registration of MRI with CT-scan labels.

the new labels were in fact not as expected from previous labelling from the MRI. For the previously classified "Grey" group, the majority of new labels were "Grey/White", and for the previously classified "White" group, the majority of new labels were "White/Grey". This can be explained by the chosen thresholds for values of $(B_1/A_1)$. The vast majority of trios have values of $(B_1/A_1)$ either lower than 0.4, or higher than 0.6. The fact that the majority of $(B_1/A_1)$ is not close to 0.5 even for the previously classified homogeneous cases could be justified from the fact that the brain has a complex pattern when it comes to tissue distribution. Even if contacts are inserted punctually in one tissue, the conductivity between two consecutive contacts depends on the surrounding tissue as well. Therefore, even if both contacts of a pair are in grey matter there might be some white matter in between them that will influence the conductivity see Fig. 5.4a. Nevertheless, for the previously classified "Grey" group, for the remainder of trios for which $0.4 \leq (B_1/A_1) \leq 0.6$, the majority were classified as being a part of the "Grey" group in the new classification. However, for the previously classified "White" group, for the trios of contacts with $0.4 \leq (B_1/A_1) \leq 0.6$, the majority of new labels were equal to "Mix". This means that for the majority of cases $40\% \leq \hat{P}(G/G|x) \leq 60\%$, which is justifiable from the fact that most of the white matter contacts used are close to grey matter, therefore there might be grey matter influences on the conductivity of such cases.

Finally, for the previously classified "Mixed" group, there is a similar phenomenon that can be observed for the previously classified homogeneous groups, in which the majority of the new labels are either "Grey/White", or "White/Grey". Once again, this is justified from the fact that the majority of cases have $(B_1/A_1)$ either lower than 0.4, or higher than 0.6. In the specific case of previously classified "Mix" group, this is easily justified from the fact that the proportion of the "middle tissue" might not be the same between the first and second contacts

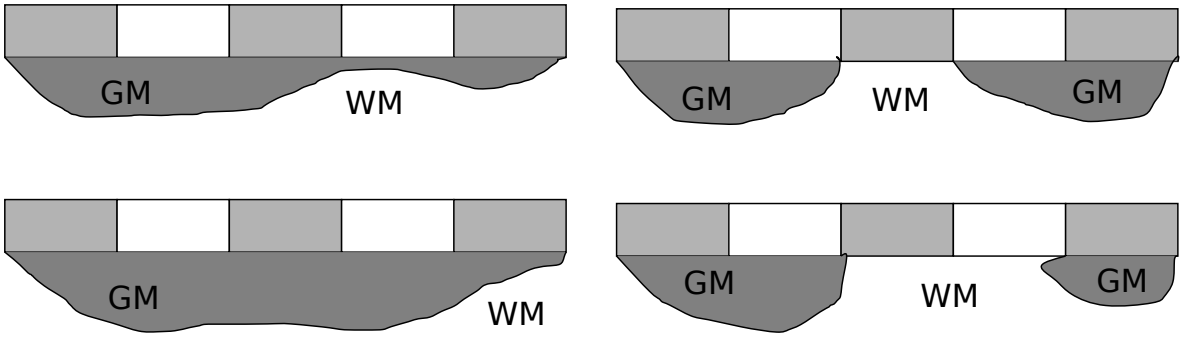


(a) Three contacts in "Grey" group (b) Three contacts in "Mix" group

Figure 5.4: Differences in tissue distribution between three consecutive contacts in (a) grey matter, and in (b) mixed tissues that result in different conductivities between them.

compared to the second and third contacts, this can be seen in Fig. 5.4b. Nevertheless, for the $0.4 \leq (B_1/A_1) \leq 0.6$ cases, the majority of new labels were equal to "Mix".

As mentioned in section 5.1.2, the posterior probabilities obtained from the non-parametric classification approach of the first two contacts of a trio of heterogeneous tissue composition, can be used to get insight into the label of each contact of the trio. For the "Grey/White" trios, the higher $\hat{P}(G/G|x)$ is, the more likely the first second contacts are to be in grey matter. Also, the closest $\hat{P}(G/G|x)$ is to 0.5, the more likely the first and second contacts are to be in heterogeneous matter. For the "White/Grey" trios, the smaller $\hat{P}(G/G|x)$ is, the more likely the first and second contacts are to be in homogeneous white matter. Also, the closest $\hat{P}(G/G|x)$ is to 0.5, the more likely the first and second contacts are to be in heterogeneous matter. This can be observed in Fig. 5.5, in which the posterior probabilities $\hat{P}(G/G|x)$ of heterogeneous groups as classified by the co-registration of MRI with CT-scan are plotted against $(B_1/A_1)$ values, and are separated by group according to the classification of each contact on the trio.

By looking at Fig. 5.5 for the "Grey/White" group, it can be seen that higher values of $\hat{P}(G/G|x)$ are obtained for trios of contacts for which the first and second contacts were labelled as being a part of grey matter, and smaller values of $\hat{P}(G/G|x)$ were obtained when the first contact of the trio was labelled grey matter and the second was labelled white matter. For the "White/Grey" group, the separation is less clear but there is still a tendency of $\hat{P}(G/G|x)$ being smaller when the first and second contacts are labelled as white matter, and $\hat{P}(G/G|x)$ being close to 0.5 when first and second contacts are labelled as white and grey matters respectively.

## 5.2 Classification of single contacts

The aim of this section is to show how to combine the previously proposed methods to create an automatic single contact classification scheme. A total of 356 trios of contacts are used, as

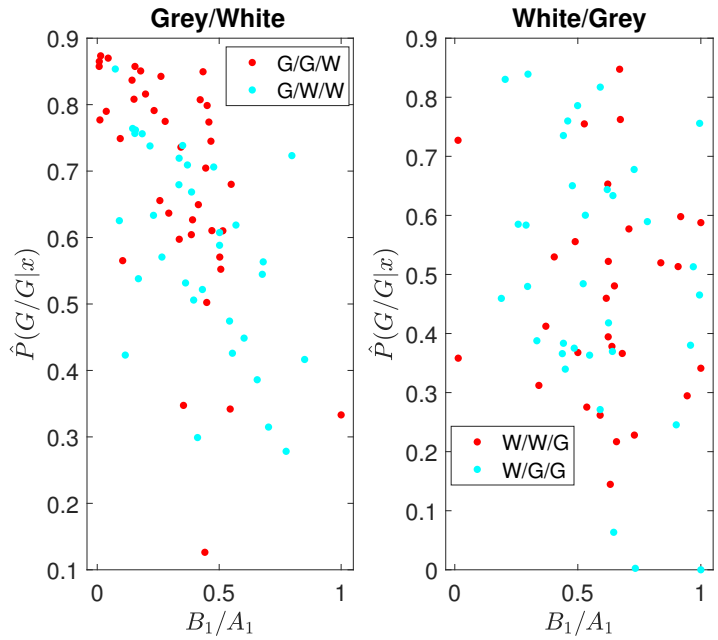


Figure 5.5: Comparison of $\hat{P}(G/G|x)$ obtained for heterogeneous groups "Grey/White" in the left, and "White/Grey" in the right, in regard to classification of each contact according to the co-registration of MRI with CT-scan.

they represent the trios for which the parametric models were validated. For each trio, the non-parametric method is applied for the first two contacts, forming 356 pairs.

### 5.2.1 Single Contact Classification Using Separate Methods

At first, the idea is to test how the existing identification-based classification methods perform for the classification of a single contact with no prior homogeneous and heterogeneous group selection based on MRI. As in the case of the non-parametric method the classification is done considering pairs of contacts, and for the case of the parametric method the classification is done considering trios, the idea is to use the features to classify only the first contact of the pair, which is equivalent to the first contact of the trio. Thus, the labels are simply going to be "Grey", and "White" of the first contact as for the MRI classification.

Two LDA classifiers are trained considering the MRI classification as the ground truth, one considering the non-parametric features and only homogeneous pairs according to the MRI (145 "Grey/Grey", and 124 "White/White"), and the other one considering the parametric feature and only heterogeneous trios according to the MRI (73 "Grey/White", and 63 "White/Grey"). It is important to note that an heterogeneous trio can be related to a homogeneous pair, in the cases where the first two contacts of the trio are in the same tissue and the third one in a different tissue. For the pairs of contacts 76% are in homogeneous tissue, and 24% is in heterogeneous tissue. For the trios of contacts 56% are in homogeneous tissue, 38% in heterogeneous tissue, and 6% are in mixed tissue, in which the second contact

is in a different tissue than the other two (Grey/White/Grey or White/Grey/White).

The classifiers were trained using the MRI labels of the first contact, with 75 % of the data, and validated with the remaining 25 %. Once the two classifiers were trained, they were applied to pairs and trios of contacts in homogeneous and heterogeneous groups separately, and also to all 356 first contacts of the considered pairs and trios. The accuracies of the classifiers for selected groups, as well as the accuracy of the classifiers considering all contacts are shown in Table 5.1.

| LDA Classifier | Accuracy | | |
|---|---|---|---|
| | Only homogeneous | Only heterogeneous | All contacts |
| Non-parametric | 72% (76% of pairs) | 55% (24% of pairs) | 68% |
| Parametric | 60% (56% of trios) | 73% (38% of trios) | 65% |

Table 5.1: Accuracies of identification-based LDA classifiers for 356 single contacts

As expected, the non-parametric classifier performs better for homogeneous groups, and the parametric classifier performs better for heterogeneous groups. The parametric classifier presents higher accuracy for homogeneous group separation than the non-parametric classifier for heterogeneous group separation. However, when it comes to overall accuracy considering all groups, the non-parametric classifier performs better than the parametric one. This is because 76% of contact pairs are in homogeneous tissues.

### 5.2.2 Combination of Both Identification Methods

As it can be seen from the previous section, each identification-based classification method classifies well the label of the first contact for different types of tissue combinations. Here, the idea is to combine information from both classifiers using the posterior probabilities of each first contact belonging to the "Grey" group according to each classifier $c \in$ [non-parametric (np), parametric (p)]. Using Bayes rule with Gaussian distribution density given in equation (3.7) and recalled below:

$$P_c(x|G) = \frac{1}{((2\pi)^d|\Sigma_G|)^{\frac{1}{2}}} exp\left(-\frac{1}{2}(x-\mu_G)\Sigma_G^{-1}(x-\mu_G)^T\right) \tag{5.1}$$

where $x$ represents one contact, $d$ the number of features ($d = 4$ for the non-parametric, and $d = 1$ for the parametric), and $\Sigma_G$ and $\mu_G k$ the covariance and the mean of the features of group "Grey" respectively. Considering $P_G$ as the prior probability of the "Grey" class, and a normalization constant $P(x) = \sum_{k\in[G,W]} P_c(x|k)P_k$, the normalised posterior probability is given by:

$$\hat{P}_c(G|x) = \frac{P_c(x|G)P_G}{P(x)} \tag{5.2}$$

The values of $\hat{P}_c(G|x)$ indicate how likely the contact $x$ is of being a part of the "Grey" group given the feature values of $x$. Each 356 combination of pairs and trios, are assigned two values of normalised posterior probabilities $\hat{P}_{np}(G|x)$, and $\hat{P}_p(G|x)$ corresponding to the non-parametric and parametric classifiers respectively.

#### 5.2.2.1 Bad contacts elimination

As a first step, one can use this information to eliminate contacts with "Bad" classification. This can be done by comparing the label attributed by each classifier. From the 356 trios ans pairs, the contacts that had the same attributed label using both non-parametric and parametric classifier can be considered as correct (72%). However, it does not mean that all of the remaining 28% should be considered to be "badly" classified. In fact, for the cases where either non-parametric or parametric classifiers have probabilities in the middle range ($0.4 < \hat{P}_c(G|x) < 0.6$), it means that the chances for the contact being in grey or white matter are close for the specific classifier, so one should use the other classifier to make a decision. In this cases, there is no error of classification. Thus, the only classifications that can be considered as "Bad" when comparing labels attributed by the two classifiers are the ones for which when one of the normalised posterior probabilities is high the other is low.

With that, only 14% of contacts were considered as "badly" classified, leaving 305 contacts to be analysed in the following section. The graphical representation of the "Bad" contact elimination according to the normalised posterior probabilities can be found in Fig. 5.6, together with the likely trio compositions expected for each combination of probabilities. The reason for the existence of "Bad" classifications using the identification methods is unclear. One justification might be the presence of important noise in the data of these specific contacts that has an influence in the identified models.

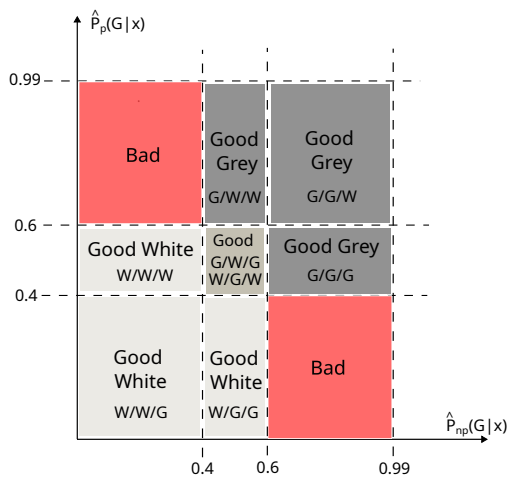


Figure 5.6: Representation of the "Bad" contact elimination process according to the normalised posterior probabilities.

#### 5.2.2.2 Combined classification

Once the contacts of "Bad" classification were eliminated by comparison of the normalised posterior probabilities of the non-parametric and parametric classifiers, what is left to do is to combine the information of each classifier. In order to do so, a unified normalised posterior probability is calculated by taking the mean of the normalised posterior probabilities of each classifier:

$$\hat{P}(G|x) = \frac{\hat{P}_{np}(G|x) + \hat{P}_{p}(G|x)}{2} \tag{5.3}$$

If $\hat{P}(G|x) > 0.5$ the contact is considered to be in "Grey" matter, and if $\hat{P}(G|x) < 0.5$ the contact is considered to be in "White" matter. With the combined classification, and considering only the 305 contacts previously selected, the obtained accuracy in respect to the MRI classification is 72%. In order to compare the combined classification with each classifier separately, the same 305 selected pairs and trios of contacts are used. In Fig. 5.7 the percentage of correctly classified first contacts considering the combined classification is compared to the percentage of correctly classified first contacts of the separate classifiers in regard to the MRI classification of the pairs and trios for the non-parametric and parametric cases respectively. In Table 5.2, the overall accuracies for each classifier considering all 305 contacts are presented.

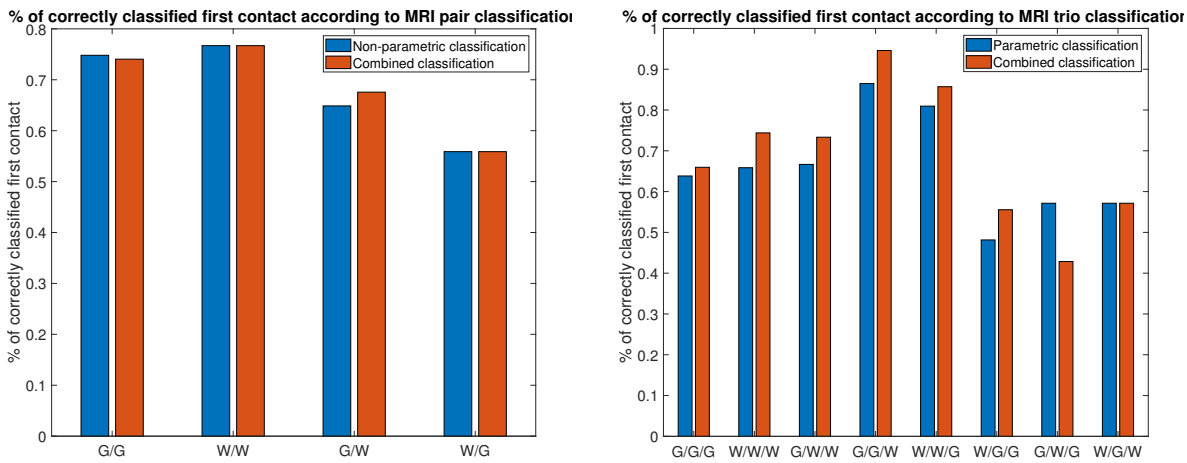


(a) Non-parametric classifier (b) Parametric classifier

Figure 5.7: Comparison of correctly classified first contacts in respect to MRI groups of (a) non-parametric and combined classifiers, and (b) parametric and combined classifiers.

In general, it can be seen that the combined classifier has very similar performance to the non-parametric classifier. The former is slightly less effective for classification of "Grey/Grey" cases, but more effective for classification of "Grey/White" cases. However, the combined classifier has a better performance than the parametric one for most of the cases other than "Grey/White/Grey", and "White/Grey/White" tissue compositions. Indeed, the improve-

| | Accuracy |
|---|---|
| Combined | 72% |
| Non-parametric | 72% |
| Parametric | 66% |

Table 5.2: Accuracies for Single Contact Classification for Each Classifier for 305 Contacts

ment is from 66% alone to 72% with the combined classifier. With the elimination of "Bad" contacts, the performance of individual classifiers was enhanced when compared to Table 5.1.

The results indicate that out of the two previously proposed classifiers, the non-parametric one is the most robust for single tissue classification. This can be explained by the fact that the parametric classification method uses trios of contacts for feature extraction. The more contacts are used, the more the conductivity of the medium is impacted by other surrounding tissues, and the harder binary classification is. Nevertheless, the parametric classifier can still be of help for the non-parametric classification for eliminating uncertain contacts, and giving an idea of the surrounding tissue composition.

## 5.3 Conclusions

In this chapter, both of the methods based on non-parametric and parametric identification proposed in the previous two chapters were combined in order to form two different classification methods. One able to classify trios of consecutive contacts inserted both in homogeneous and heterogeneous tissues, and the other able to classify single contacts.

The first method consists in first using the modelling approach to create two clusters. The first cluster is composed by trios of contacts for which the tissue between the first and second contacts is of the same composition as the tissue between the second and third contacts. The second cluster is composed by trios of contacts for which the distribution of different tissues between the first and second contacts is not the same as in between the second and third contacts. The second cluster can be classified straightforward using the values of $(B_1/A_1)$ into two heterogeneous groups "Grey/White" and "White/Grey". In order to classify the first cluster as being a part of the homogeneous "Grey" and "White" groups or the "Mix" group, the non-parametric approach with non-parametric frequency response method should be used with the LDA classifier for the first and second contacts of the trio in monopolar reference. The labels are determined by looking at posterior probabilities $\hat{P}(G/G|x)$. These probabilities can also be used in the case of the heterogeneous groups in order to have a better insight as to the labels of each of the contacts individually.

By applying the overall classification method to the data from 19 epileptic patients, it can be seen that most of the trios of contacts were classified as being a part of heterogeneous groups "Grey/White" and "White/Grey". The divergence from the classification obtained with the co-registration of MRI with CT-scan can be justified from the fact that both the

non-parametric and model approaches for classification proposed in this study are based on the fact that the conductivities of grey and white matter are different from one another. The conductivity between two contacts is not punctual, and does not depend only on the tissues surrounding the contacts but also in the tissue between them.

The second method consists in training two separate LDA classifiers, one using the non-parametric method and homogeneous groups, the other using the parametric method and heterogeneous groups. However, both methods are used for the classification of only the first contact of a pair or trio. By the combination of the posterior probabilities of the LDA classifiers, contacts with bad classification were eliminated. The accuracy of the combined classifier with the elimination of bad contacts is similar to the non-parametric method, and better than the parametric one. This can be explained by the fact that, as the parametric classification uses trios of contacts, it is more affected by surrounding tissues, thus it is worse for binary classification.

In general, the proposed classification methods combining the non-parametric and parametric modelling approaches are sensitive to all tissue surrounding the trio of contacts and are not necessarily useful for punctual tissue classification, or classification of tissue adjacent to a contact. As was discussed in (Mercier et al. 2017), the signal measured by a single contact is largely impacted by the surrounding tissues, thus a binary classification might not be the most appropriate. As they are, the combined tissue classification methods serve as a complement for MRI tissue classification. Furthermore, once the non-parametric and parametric classifiers are trained, they can be helpful for doctors to decide which contacts are of interest for the stimulation phase of the SEEG investigation. The second method for single contact classification also helps for elimination of bad classifications due to noisy signals recorded by the contacts that affect identified models.

# Conclusion et perspectives

## General conclusion

In the context of pre-surgical evaluation for drug-resistant epileptic patients, brain tissue classification plays an important role in the correct identification of epileptic zones as well as of the eloquent cortex. There is, however, not a lot of variety when it comes to classification methods. The vast majority of them are based on imaging, such as the co-registration of MRI with CT-scan, in which the tissue in which a certain contact is inserted in is labelled according to the intensity of the image voxel. The problematic of tissue classification and EZ identification was reviewed in chapter 1.

The main goal of this study was to propose methods for brain tissue classification using only signals measured during typical SEEG examination. In order to do so, two different approaches were proposed, and tested on data of 19 epileptic patients.

In chapter 3, the signal based approach was presented in which features were either extracted directly from monopolar SEEG signals, or from the non-parametric frequency responses of pairs of consecutive electrodes. Such features were used for supervised classification using mainly LDA classifiers for the frequency response case, and six other classification methods for the monopolar signals case. From this approach, the highest accuracy obtained was $72 \pm 1\%$ compared to the classification from MRI of homogeneous tissue compositions, and was achieved using features extracted from the frequency domain responses of paired contacts and an LDA classifier. Signals in monopolar reference have proven not to be very discriminant between grey and white matter. When comparing to the only other study that conducts tissue classification from SEEG signals, features proposed in this study extracted from the Bode plots of two consecutive electrodes are more discriminant when using the same classification algorithm and data. The classification is robust to contacts located in epileptic networks, and is region independent.

The model based approach for brain tissue identification was presented in chapter 4 based on the methods for system identification presented in chapter 2. At first, the modelling of a *phantom EEG* from a physical stand point was proposed in order to gather information on the different parts of the measurement chain, mainly the electrode-electrolyte interface. With the proposed method, all separate components of the electronic circuit could be identified. After that, the modelling of the brain-electrode interface using triplets of adjacent SEEG contacts was proposed based on the literature and adapted for the problem to solve. An identification method was proposed considering constraints and previous knowledge. Even though the identified coefficients of the models could not be used to recover the electronic circuit component values, the ratios between them could still be used for brain tissue classification. The accuracy in group separation obtained using a simple LDA classifier and one feature extracted from the identified models was $73 \pm 6\%$. This value is close to the one obtained using features from the

non-parametric frequency response of patients.

From the chosen referencing configuration, the resulting transfer function of the brain-electrode interface can be approximated to a purely resistive model. Although such model does not represent all the dynamics of the interface, it can still achieve the same classification accuracy.

The features extracted from both approaches proposed in this study proved to be discriminant for brain tissue separation, when compared to previously proposed ones. The signal approach can be used for homogeneous tissue separation, and the model approach can be used for heterogeneous tissue separation.

In chapter 5 both signal and model approaches were combined in order to propose a general brain tissue classifier for both homogeneous and heterogeneous tissue combinations of trios of consecutive contacts. As both signal and model approaches rely on the difference of conductivity between contacts, the general classification method is sensitive to all tissues surrounding the three contacts, not only the immediate tissue in contact with them. Thus, apart from the highly probable homogeneous tissue cases, and some heterogeneous cases, one can not use the method proposed here for individual contact classification. In other words, the classification shows the distribution of brain tissue between two contacts of the trio and not in a specific spot. Nevertheless, the information on the tissue distribution between three contacts can be also useful during SEEG investigation.

As it is, the classification method proposed in this study can be used as a support for the existing classification methods using the co-registration of MRI with CT-scan, and to help doctors to choose contacts to be recorded during SEEG investigation.

## Perspectives

As the vast majority of tissue classification methods are image based, they are considered to be the ground truth. However, one should consider that such methods are limited by image resolution, and could also present miss-classifications. Yet, there is no way of knowing exactly how accurate MRI based classification is, when there are no other methods to compare it with. Thus, in order to understand the true validity of the proposed methods in this study, more tests need to be performed with different data sets, focusing mainly in contacts located in regions for which the probability of correct MRI classification is high. If there are any other methods to be proposed in the future for tissue classification, they could also provide a greater insight to how accurate the classification methods of this study could be.

The choice of the voltage reference has a high impact on the differentiation of brain tissues. This was previously discussed in literature, and can also be seen when comparing the frequency responses obtained using contacts with monopolar reference, and contacts referenced considering adjacent electrodes for both approaches of this study. As there are endless possibilities for referencing signals, the same model and signal based features could be applied

in re-referenced SEEG signals, in order to see in which configuration the best accuracy can be achieved. For different references, however, the proposed electronic circuit model might need some small modifications.

As mentioned, the proposed method has only been applied in baseline signals collected during wakefulness while the patients were resting. Studies suggest differences in the power spectrum of signals measured during sleep when compared to wakefulness ((De Gennaro et al. 2003), and (Amzica et al. 1998)). These differences can be mainly perceived for smaller frequencies and could be useful for tissue classification. Other types of signals for which the classification methods could also be applied to are signals measured during direct brain stimulation, for which grey and white matter react differently.

In addition, even though the proposed electronic circuit model fits the expected response from the data, and can be used for tissue classification, the fit in the Nyquist plot could still be improved. For that, adjustments to the model and identification algorithm could be considered.

Finally both classification methods use consecutive SEEG contacts in a specific order. As all combinations are considered, one contact can be considered as the input in one case, and as the output in the other. This overlapping information could also be used to classify the tissues in which each contact is inserted in individually.

# Bibliography


Machado, M., A. Voda, G. Besançon, G. Becq, and O. David (2021). "Frequency-domain identification of stereoelectroencephalographic transfer functions for brain tissue classification". In: *IFAC-PapersOnLine* 54.7, pp. 565–570 (cit. on pp. 2, 40).

Machado, M., A. Voda, G. Besançon, G. Becq, P. Kahane, et al. (2022). "Brain tissue classification from stereoelectroencephalographic recordings". In: *Journal of Neuroscience Methods* 365, p. 109375 (cit. on pp. 2, 40).

Lopes, P. et al. (2021). "Machine Learning and Stereoelectroencephalographic Feature Extraction for Brain Tissue Classification". In: *IFAC-PapersOnLine* 54.15, pp. 340–345 (cit. on pp. 2, 58–62).

Machado, M., A. Voda, G. Besançon, G. Becq, and O. David (2020). "New modeling results for an EEG measurement system with exciting and reading electrodes". In: *IFAC-PapersOnLine* 53.2, pp. 15922–15927 (cit. on pp. 2, 66).

Machado, Mariana Mulinari Pinheiro et al. (2023). "Electrode–brain interface fractional order modelling for brain tissue classification in SEEG". In: *Biomedical Signal Processing and Control* 79, p. 104050 (cit. on p. 2).

Pinheiro Machado, Mariana Mulinari et al. (2022a). "Dynamic Modelling of the Brain-electrode Interface for Stereoelectroencephalography". In: *2022 26th International Conference on System Theory, Control and Computing (ICSTCC)*, pp. 576–581 (cit. on p. 2).

— (2022b). "System-Identification-Based Automatic Brain Tissue Classification for Stereoelectroencephalography". In: *2022 26th International Conference on System Theory, Control and Computing (ICSTCC)*, pp. 440–445 (cit. on p. 2).

Fisher, R. et al. (2005). "Epileptic seizures and epilepsy: definitions proposed by the International League Against Epilepsy (ILAE) and the International Bureau for Epilepsy (IBE)". In: *Epilepsia* 46.4, pp. 470–472 (cit. on p. 5).

David, O., J. Bastin, et al. (2010). "Studying network mechanisms using intracranial stimulation in epileptic patients". In: *Frontiers in Systems Neuroscience* 4, p. 148 (cit. on pp. 5, 8).

Carvallo, A. et al. (2018). "Biophysical modeling for brain tissue conductivity estimation using SEEG electrodes". In: *IEEE Transactions on Biomedical Engineering* 66.6, pp. 1695–1704 (cit. on pp. 5, 11–13, 46, 65, 80, 88, 96).

Greene, P. et al. (2021). "Classification of stereo-EEG contacts in white matter vs. gray matter using recorded activity". In: *Frontiers in neurology*, p. 1806 (cit. on pp. 5, 9, 10, 39, 40, 46, 53, 54, 63).

Brodie, M. et al. (1997). "Commission on European Affairs: appropriate standards of epilepsy care across Europe". In: *Epilepsia* 38.11, pp. 1245–1250 (cit. on p. 5).

Acharya, U. et al. (2019). "Characterization of focal EEG signals: a review". In: *Future Generation Computer Systems* 91, pp. 290–299 (cit. on p. 5).

Trebaul, L., P. Deman, et al. (2018). "Probabilistic functional tractography of the human cortex revisited". In: *NeuroImage* 181, pp. 414–429 (cit. on pp. 5, 9).

Katti, G., S. Ara, and A. Shireen (2011). "Magnetic resonance imaging (MRI)–A review". In: *International journal of dental clinics* 3.1, pp. 65–70 (cit. on p. 6).

Duncan, J. (1997). "Imaging and epilepsy." In: *Brain: a journal of neurology* 120.2, pp. 339–377 (cit. on p. 6).

Bien, C. et al. (2009). "Characteristics and surgical outcomes of patients with refractory magnetic resonance imaging–negative epilepsies". In: *Archives of neurology* 66.12, pp. 1491–1499 (cit. on p. 6).

Nunez, P., R. Srinivasan, et al. (2006). *Electric fields of the brain: the neurophysics of EEG.* Oxford University Press, USA (cit. on p. 7).

Noachtar, S. and J. Rémi (2009). "The role of EEG in epilepsy: a critical review". In: *Epilepsy & Behavior* 15.1, pp. 22–33 (cit. on p. 7).

Talairach, J. and J. Bancaud (1973). "Stereotaxic approach to epilepsy". In: *Progress in neurological surgery.* Vol. 5. Karger Publishers, pp. 297–354 (cit. on p. 7).

Bartolomei, F., S. Lagarde, et al. (2017). "Defining epileptogenic networks: contribution of SEEG and signal analysis". In: *Epilepsia* 58.7, pp. 1131–1147 (cit. on pp. 7, 8).

Mercier, M. et al. (2017). "Evaluation of cortical local field potential diffusion in stereotactic electro-encephalography recordings: a glimpse on white matter signal". In: *Neuroimage* 147, pp. 219–232 (cit. on pp. 7, 10, 39, 49, 116).

Kahane, P. and F. Dubeau (2014). "Intracerebral depth electrodes electroencephalography (stereoencephalography)". In: *Current Practice of Clinical Encephalography. Philadelphia, Wolters Kluwer Health*, pp. 398–437 (cit. on p. 8).

Bartolomei, F., P. Chauvel, and F. Wendling (2008). "Epileptogenicity of brain structures in human temporal lobe epilepsy: a quantified study from intracerebral EEG". In: *Brain* 131.7, pp. 1818–1830 (cit. on p. 8).

David, O., T. Blauwblomme, et al. (2011). "Imaging the seizure onset zone with stereo-electroencephalography". In: *Brain* 134.10, pp. 2898–2911 (cit. on p. 8).

David, O., A. Job, et al. (2013). "Probabilistic functional tractography of the human cortex". In: *Neuroimage* 80, pp. 307–317 (cit. on pp. 8, 41).

David, O., A. Woźniak, et al. (2008). "Preictal short-term plasticity induced by intracerebral 1 Hz stimulation". In: *Neuroimage* 39.4, pp. 1633–1646 (cit. on p. 9).

Dora, L. et al. (2017). "State-of-the-art methods for brain tissue segmentation: A review". In: *IEEE reviews in biomedical engineering* 10, pp. 235–249 (cit. on p. 10).

Deman, P. et al. (2018). "IntrAnat electrodes: a free database and visualization software for intracranial electroencephalographic data processed for case and group studies". In: *Frontiers in neuroinformatics* 12, p. 40 (cit. on pp. 10, 41).

Tohka, J. (2014). "Partial volume effect modeling for segmentation and tissue classification of brain magnetic resonance images: A review". In: *World journal of radiology* 6.11, p. 855 (cit. on p. 10).

Cho, J. et al. (2015). "Influence of the head model on EEG and MEG source connectivity analyses". In: *Neuroimage* 110, pp. 60–77 (cit. on p. 11).

Holdefer, R., R. Sadleir, and M. Russell (2006). "Predicted current densities in the brain during transcranial electrical stimulation". In: *Clinical neurophysiology* 117.6, pp. 1388–1397 (cit. on p. 11).

McCann, H., G. Pisano, and L. Beltrachini (2019). "Variation in reported human head tissue electrical conductivity values". In: *Brain topography* 32.5, pp. 825–858 (cit. on pp. 11, 12, 46, 56, 96).

Ammari, H. et al. (2017). "Determining anisotropic conductivity using diffusion tensor imaging data in magneto-acoustic tomography with magnetic induction". In: *Inverse Problems* 33.12, p. 125006 (cit. on p. 11).

Basser, P., J. Mattiello, and D. LeBihan (1994). "MR diffusion tensor spectroscopy and imaging". In: *Biophysical journal* 66.1, pp. 259–267 (cit. on p. 12).

Logothetis, N., C. Kayser, and A. Oeltermann (2007). "In vivo measurement of cortical impedance spectrum in monkeys: implications for signal propagation". In: *Neuron* 55.5, pp. 809–823 (cit. on pp. 12, 46, 96).

Güllmar, D., J. Haueisen, and J. Reichenbach (2010). "Influence of anisotropic electrical conductivity in white matter tissue on the EEG/MEG forward and inverse solution. A high-resolution whole head simulation study". In: *Neuroimage* 51.1, pp. 145–163 (cit. on p. 12).

Opitz, A. et al. (2017). "Limitations of ex vivo measurements for in vivo neuroscience". In: *Proceedings of the National Academy of Sciences* 114.20, pp. 5243–5246 (cit. on p. 12).

Geddes, L. and L. Baker (1967). "The specific resistance of biological material—a compendium of data for the biomedical engineer and physiologist". In: *Medical and biological engineering* 5.3, pp. 271–293 (cit. on pp. 12, 46, 96).

Satzer, D. et al. (2015). "Anatomic correlates of deep brain stimulation electrode impedance". In: *Journal of Neurology, Neurosurgery & Psychiatry* 86.4, pp. 398–403 (cit. on pp. 13, 96).

Lempka, S., S. Miocinovic, et al. (2009). "In vivo impedance spectroscopy of deep brain stimulation electrodes". In: *Journal of neural engineering* 6.4, p. 046001 (cit. on pp. 13, 15–17, 65, 80, 81, 88, 97).

Lempka, S., M. Johnson, et al. (2011). "Theoretical analysis of intracortical microelectrode recordings". In: *Journal of neural engineering* 8.4, p. 045006 (cit. on p. 13).

Sankar, V. et al. (2014). "Electrode impedance analysis of chronic tungsten microwire neural implants: understanding abiotic vs. biotic contributions". In: *Frontiers in neuroengineering* 7, p. 13 (cit. on pp. 13, 16, 65, 80, 97).

Otto, K., M. Johnson, and D. Kipke (2006). "Voltage pulses change neural interface properties and improve unit recordings with chronically implanted microelectrodes". In: *IEEE transactions on biomedical engineering* 53.2, pp. 333–340 (cit. on p. 13).

Johnson, M., K. Otto, and D. Kipke (2005). "Repeated voltage biasing improves unit recordings by reducing resistive tissue impedances". In: *IEEE Transactions on neural systems and rehabilitation engineering* 13.2, pp. 160–165 (cit. on pp. 13, 16, 17, 65, 80, 97).

Koessler, L. et al. (2017). "In-vivo measurements of human brain tissue conductivity using focal electrical current injection through intracerebral multicontact electrodes". In: *Human brain mapping* 38.2, pp. 974–986 (cit. on p. 13).

Trebaul, L., D. Rudrauf, et al. (2016). "Stimulation artifact correction method for estimation of early cortico-cortical evoked potentials". In: *Journal of neuroscience methods* 264, pp. 94–102 (cit. on pp. 13, 65).

Besançon, G., G. Becq, and A. Voda (2019). "Fractional-order modeling and identification for a phantom EEG system". In: *IEEE Transactions on Control Systems Technology* 28.1, pp. 130–138 (cit. on pp. 14–17, 66–68, 83, 88).

Robinson, D. (1968). "The electrical properties of metal microelectrodes". In: *Proceedings of the IEEE* 56.6, pp. 1065–1071 (cit. on pp. 14, 68–70, 72, 88).

De Levie, R. (1965). "The influence of surface roughness of solid electrodes on electrochemical measurements". In: *Electrochimica Acta* 10.2, pp. 113–130 (cit. on p. 14).

Liang, S., R. Wu, and L. Chen (2015). "Laplace transform of fractional order differential equations". In: *Electron. J. Differ. Equ* 139, p. 2015 (cit. on pp. 14, 82).

McAdams, E., A. Lackermeier, et al. (1995). "The linear and non-linear electrical properties of the electrode-electrolyte interface". In: *Biosensors and bioelectronics* 10.1-2, pp. 67–74 (cit. on pp. 14–16, 69, 70).

Grill, W. and J. Thomas Mortimer (1994). "Electrical properties of implant encapsulation tissue". In: *Annals of biomedical engineering* 22.1, pp. 23–33 (cit. on p. 15).

Yousif, N. and X. Liu (2009). "Investigating the depth electrode–brain interface in deep brain stimulation using finite element models with graded complexity in structure and solution". In: *Journal of neuroscience methods* 184.1, pp. 142–151 (cit. on p. 15).

Ljung, L. (1998). *System Identification: Theory for the User*. Pearson Education (cit. on pp. 19, 22, 47, 85).

Landau, I. and G. Zito (2006). *Digital control systems: design, identification and implementation*. Vol. 130. Springer (cit. on pp. 19, 34, 72, 74).

Stoica, P. and R. Moses (1997). *Introduction to spectral analysis*. Pearson Education (cit. on p. 19).

Young, Peter C (1970). "An instrumental variable method for real-time identification of a noisy process". In: *Automatica* 6.2, pp. 271–287 (cit. on p. 29).

Waltz, R. et al. (2006). "An interior algorithm for nonlinear optimization that combines line search and trust region steps". In: *Mathematical programming* 107.3, pp. 391–408 (cit. on p. 30).

Wächter, A. and L. Biegler (2006). "On the implementation of an interior-point filter line-search algorithm for large-scale nonlinear programming". In: *Mathematical programming* 106.1, pp. 25–57 (cit. on p. 30).

Oustaloup, A. (1995a). "La dérivation non entière: Théorie". In: *Synthèse et Applications* (cit. on p. 35).

Podlubny, I. (1998). *Fractional differential equations: an introduction to fractional derivatives, fractional differential equations, to methods of their solution and some of their applications*. Elsevier (cit. on p. 35).

Malti, R. et al. (2006). "Tutorial on system identification using fractional differentiation models". In: *IFAC Proceedings Volumes* 39.1, pp. 606–611 (cit. on pp. 35, 36).

Trigeassou, J. et al. (1999). "Modeling and identification of a non integer order system". In: *1999 European Control Conference (ECC)*. IEEE, pp. 2453–2458 (cit. on p. 35).

Magin, R. and M. Ovadia (2008). "Modeling the cardiac tissue electrode interface using fractional calculus". In: *Journal of Vibration and Control* 14.9-10, pp. 1431–1442 (cit. on pp. 35, 69).

Sommacal, L. et al. (2008). "Fractional multi-models of the frog gastrocnemius muscle". In: *Journal of Vibration and Control* 14.9-10, pp. 1415–1430 (cit. on p. 35).

Zou, C. et al. (2017). "Nonlinear fractional-order estimator with guaranteed robustness and stability for lithium-ion batteries". In: *IEEE Transactions on Industrial Electronics* 65.7, pp. 5951–5961 (cit. on p. 35).

Bohannan, G. (2008). "Analog fractional order controller in temperature and motor control applications". In: *Journal of Vibration and Control* 14.9-10, pp. 1487–1498 (cit. on p. 35).

Samko, S., A. Kilbas, O. Marichev, et al. (1993). *Fractional integrals and derivatives.* Vol. 1. Gordon and breach science publishers, Yverdon Yverdon-les-Bains, Switzerland (cit. on p. 35).

Oldham, K. and J. Spanier (1974). *The fractional calculus theory and applications of differentiation and integration to arbitrary order.* Elsevier (cit. on p. 35).

Grunwald, A. (1867). "Uber" begrente" Derivationen und deren Anwedung". In: *Zangew Math und Phys* 12, pp. 441–480 (cit. on pp. 36, 83).

Letnikov, A. (1868). ": Theory of differentiation with an arbitrary index. Math. Sb. 3, 1-66". In: (cit. on pp. 36, 83).

Jonathan (2022). *Fractional Derivative.* URL: `https://www.mathworks.com/matlabcentral/fileexchange/45982-fractional-derivative` (visited on 03/09/2022) (cit. on pp. 36, 84).

Carlson, G. and C. Halijak (1964). "Approximation of fractional capacitors (1/s)ˆ(1/n) by a regular Newton process". In: *IEEE Transactions on Circuit Theory* 11.2, pp. 210–213 (cit. on p. 36).

Matsuda, K. and H. Fujii (1993). "H (infinity) optimized wave-absorbing control-Analytical and experimental results". In: *Journal of Guidance, Control, and Dynamics* 16.6, pp. 1146–1153 (cit. on p. 36).

Oustaloup, A. (1995b). *Digital control systems: design, identification and implementation.* Hermes Science Publications (cit. on p. 36).

Petrás, I. (2011). *Fractional derivatives, fractional integrals, and fractional differential equations in Matlab.* IntechOpen (cit. on pp. 36, 72).

Petráš, I. (2003). *Digital fractional order differentiator/integrator-IIR type.* URL: `http://www.%20mathworks.%20com/matlabcentral/fileexchange/3672` (visited on 03/09/2022) (cit. on pp. 36, 72).

Al-Alaoui, M. (1993). "Novel digital integrator and differentiator". In: *Electronics letters* 29.4, pp. 376–378 (cit. on p. 36).

Vinagre, B., Y. Chen, and I. Petráš (2003). "Two direct Tustin discretization methods for fractional-order differentiator/integrator". In: *Journal of the franklin institute* 340.5, pp. 349–362 (cit. on p. 37).

Tuyisenge, V. et al. (2018). "Automatic bad channel detection in intracranial electroencephalographic recordings using ensemble machine learning". In: *Clinical Neurophysiology* 129.3, pp. 548–554 (cit. on p. 41).

Lee, C., J. Lee, A. Lee, et al. (2000). *Statistics for business and financial economics.* Vol. 1. Springer (cit. on p. 43).

Becq, G., S. Bonnet, et al. (2011). "Classification of epileptic motor manifestations using inertial and magnetic sensors". In: *Computers in biology and medicine* 41.1, pp. 46–55 (cit. on p. 44).

Becq, G., P. Kahane, et al. (2013). "Classification of epileptic motor manifestations and detection of tonic–clonic seizures with acceleration norm entropy". In: *IEEE Transactions on Biomedical Engineering* 60.8, pp. 2080–2088 (cit. on p. 44).

Frauscher, B. et al. (2018). "Atlas of the normal intracranial electroencephalogram: neurophysiological awake activity in different cortical areas". In: *Brain* 141.4, pp. 1130–1144 (cit. on pp. 44, 60).

Hastie, T., R. Tibshirani, and J. Friedman (2001). *The Elements of Machine Learning* (cit. on p. 44).

Akhtari, M. et al. (2006). "Electrical conductivities of the freshly excised cerebral cortex in epilepsy surgery patients; correlation with pathology, seizure duration, and diffusion tensor imaging". In: *Brain Topography* 18.4, pp. 281–290 (cit. on p. 56).

Roehri, N., F. Bartolomei, and C. Bénar (2019). "Delphos: Detector of ElectroPHysiological Oscillations and Spikes". In: *10th European SEEG Course* (cit. on p. 56).

Auzias, G., O. Coulon, and A. Brovelli (2016). "MarsAtlas: A cortical parcellation atlas for functional mapping". In: *Human brain mapping* 37.4, pp. 1573–1592 (cit. on p. 57).

Boonyakitanont, P. et al. (2020). "A review of feature extraction and performance evaluation in epileptic seizure detection using EEG". In: *Biomedical Signal Processing and Control* 57, p. 101702 (cit. on pp. 58, 63).

Sharmila, A. and P. Geethanjali (2018). "Effect of filtering with time domain features for the detection of epileptic seizure from EEG signals". In: *Journal of medical engineering & technology* 42.3, pp. 217–227 (cit. on pp. 58, 63).

Flandrin, P. (1992). "Wavelet analysis and synthesis of fractional Brownian motion". In: *IEEE Transactions on information theory* 38.2, pp. 910–917 (cit. on p. 60).

Hastie, T., R. Tibshirani, J. Friedman, and J. Friedman (2009). *The elements of statistical learning: data mining, inference, and prediction.* Vol. 2. Springer (cit. on p. 60).

McAdams, E. and J. Jossinet (1995). "Tissue impedance: a historical overview". In: *Physiological measurement* 16.3A, A1 (cit. on p. 65).

Becq, G., A. Voda, et al. (2017). "Experiments and Analysis for Fractional Order Modelling of an EEG Recording Process." In: *ICINCO (1)*, pp. 559–566 (cit. on pp. 66–68).

Besancon, G. et al. (2018). "Order and parameter identification for a non-integer-order model of an EEG system". In: *IFAC-PapersOnLine* 51.15, pp. 772–777 (cit. on pp. 66–68).

Walter, E. and L. Pronzato (1997). *Identification of parametric models: from experimental data.* Springer Verlag (cit. on p. 71).

Johnson, A. et al. (2004). "Design and testing of an impedance-based sensor for monitoring drug delivery". In: *Journal of the Electrochemical Society* 152.1, H6 (cit. on pp. 71, 72).

Cantrell, D. et al. (2007). "Incorporation of the electrode–electrolyte interface into finite-element models of metal microelectrodes". In: *Journal of neural engineering* 5.1, p. 54 (cit. on p. 77).

Scherer, Rudolf et al. (2011). "The Grünwald–Letnikov method for fractional differential equations". In: *Computers & Mathematics with Applications* 62.3, pp. 902–917 (cit. on p. 94).

De Gennaro, L. and M. Ferrara (2003). "Sleep spindles: an overview". In: *Sleep medicine reviews* 7.5, pp. 423–440 (cit. on p. 119).

Amzica, F. and M. Steriade (1998). "Electrophysiological correlates of sleep delta waves". In: *Electroencephalography and clinical neurophysiology* 107.2, pp. 69–83 (cit. on p. 119).

**Résumé** — L'épilepsie est un trouble neurologique qui touche plus de 15 millions de personnes dans le monde. Dans les cas où les patients souffrent d'épilepsie focale résistante aux médicaments, une chirurgie résective peut être envisagée. Pour qu'une telle chirurgie soit réussie, il est impératif d'identifier correctement la zone épileptique (ZE) à enlever, ainsi que le cortex éloquent à éviter. L'un des examens préchirurgicaux qui peut être réalisé est la stéréoélectroencéphalographie (SEEG), dans laquelle des électrodes sont placées directement dans le cerveau du patient. Lors de cet examen, la classification correcte des contacts est cruciale pour l'identification correcte des ZE. Non seulement cela aide à choisir les contacts à enregistrer, mais aussi, en cas de stimulation cérébrale directe, il est important de savoir quel type de tissu est stimulé car ils ont des dynamiques différentes.

Jusqu'à présent, la grande majorité de la classification des tissus cérébraux se fait par imagerie, le plus souvent avec le co-enregistrement de l'imagerie par résonance magnétique (IRM) et de la tomographie par ordinateur (CT). Ce processus d'étiquetage n'est pas toujours disponible. De plus, ces méthodes sont limitées par les résolutions d'imagerie, ce qui peut parfois induire des erreurs de classification. Il est donc intéressant d'explorer d'autres types de classification des tissus qui ne reposent pas sur l'imagerie.

Dans ce contexte, l'objectif de cette thèse est de proposer différentes méthodes de classification des tissus cérébraux en utilisant uniquement les signaux typiques mesurés lors des examens SEEG avec le patient au repos. Dans cette étude, deux approches principales ont été proposées pour y parvenir : Une approche basée sur le signal, et une approche basée sur un modèle. Dans le premier cas, les signaux SEEG bruts ont été considérés, et les caractéristiques ont été extraites directement soit des domaines temporel et fréquentiel, soit de la réponse fréquentielle non-paramétrique des contacts consécutifs appariés. Pour l'approche basée sur un modèle, un circuit électronique est proposé prenant en compte des trios de contacts consécutifs, sur la base des propriétés physiques de l'interface cerveau-électrode discutées dans la littérature. Un algorithme d'identification a été proposé pour identifier un tel modèle basé sur des techniques de modélisation dynamique, avec la spécificité de traiter la dynamique d'ordre fractionnaire.

Les deux approches ont été testées avec des données enregistrées chez 19 patients épileptiques. L'étiquetage préalable provenant du co-enregistrement de l'IRM et du CT scanner des patients est utilisé pour la classification supervisée. Dans l'approche par le signal, les caractéristiques obtenues à partir de la réponse en fréquence non paramétrique se sont avérées être les plus discriminantes, avec une précision allant jusqu'à $72 \pm 1\%$ en considérant les paires de contacts dans un tissu homogène avec une analyse discriminante linéaire (LDA). Pour la seconde approche, la précision obtenue était de $73 \pm 6\%$ avec un classificateur LDA en considérant des trios de contacts dans des tissus hétérogènes. Les caractéristiques proposées dans ce travail se sont avérées plus discriminantes que celles proposées dans le seul autre travail qui utilise les signaux SEEG pour la classification des tissus cérébraux. Enfin, les deux approches, celle du signal et celle du modèle, ont été combinées pour créer un classificateur général des

tissus cérébraux capable de classer les combinaisons de tissus homogènes et hétérogènes entre des trios de contacts consécutifs.

En l'état, les méthodes de classification proposées peuvent être utilisées comme support aux méthodes existantes basées sur l'imagerie, et peuvent aider les médecins à prendre des décisions pendant l'examen SEEG.

**Mots clés :** Classification des tissus cérébraux, identification d'ordre non entier, modélisation de l'interface cerveau-électrode, stéréoélectroencéphalographie, estimation de la fonction de transfert empirique, SEEG, EEG, interface électrode-électrolyte, élément à phase constante, système d'ordre fractionnaire, identification, modélisation, diagnostic.

---

**Abstract** — Epilepsy is a neurological disorder that affects over 15 million people worldwide. In cases where the patients suffer from drug-resistant focal epilepsy, a resective surgery might be considered. In order for such a surgery to be successful, it is imperative to correctly identify the epileptic zone (EZ) to be removed, as well as the eloquent cortex to be avoided. One of the pre-surgical examinations that can be conducted is the stereoelectroencephalography (SEEG), in which electrodes are placed directly into the brain of the patient. In this examination, the correct classification of contacts is crucial for the correct identification of EZs. Not only it helps with choosing contacts to be recorded, but also, in cases of direct brain stimulation, it is important to know what type of tissue is being stimulated as they have different dynamics.

So far, the vast majority of brain tissue classification is done via imaging, most commonly with the co-registration of magnetic resonance imaging (MRI) and computer tomography (CT) scan. This labelling process is not always available. Moreover, such methods are limited by imaging resolutions, which can sometimes induce classification errors. Thus, it is of interest to explore other types of tissue classification that do not rely on imaging.

In this context, the aim of this thesis is to propose different brain tissue classification methods using solely typical signals measured during SEEG examinations with the patient at rest. In this study, two main approaches were proposed to do so: A signal based approach, and a model based approach. For the first case, raw SEEG signals where considered, and features were extracted directly either from the temporal and frequency domains, or from the non-parametric frequency response of paired consecutive contacts. For the model based approach, an electronic model considering trios of consecutive contacts was proposed, based on the physical properties of the brain-electrode interface discussed in literature. An identification algorithm was proposed to identify such model based on dynamical modelling techniques, with the specificity of

dealing with fractional order dynamics.

The two approaches were tested with data recorded in 19 epileptic patients. Previous labelling from the co-registration of MRI with CT scan of the patients is used for supervised classification. From the signal approach, the features obtained from the non-parametric frequency response were proven to be the most discriminant ones, with up to $72 \pm 1\%$ accuracy considering contact pairs in homogeneous tissue with a linear discriminant analysis (LDA). For the second approach, the achieved accuracy was of $73 \pm 6\%$ with a LDA classifier considering trios of contacts in heterogeneous tissues. The proposed features in this work proved to be more discriminant than the ones proposed in the only other work that uses SEEG signals for brain tissue classification. Finally, both signal and model approaches were combined to create a general brain tissue classifier that can classify both homogeneous and heterogeneous tissue combinations between trios of consecutive contacts.

As they are, the proposed classification methods can be used as a support to the existing ones based on imaging, and can help doctors to make decisions during SEEG examination.

**Keywords:** Brain tissue classification, non-integer order identification, brain-electrode interface modelling, stereoelectroencephalography, empirical transfer function estimate, SEEG, EEG, electrode-electrolyte interface, constant phase element, fractional order system, identification, modelling, diagnosis.

---

Gipsa-lab, Domaine Universitaire - BP46
38402 Saint Martin d'Hères